

**Measurement of Top Quark Properties  
from Pair Production and Decay  
with the CMS Detector**

Dissertation  
zur Erlangung des Doktorgrades  
des Department Physik  
der Universität Hamburg

vorgelegt von  
Diplom-Physiker Christoph Rosemann  
aus Mönchengladbach

Hamburg  
November 2008

Gutachter der Dissertation: Prof. Dr. Joachim Mnich  
Prof. Dr. Peter Schleper

Gutachter der Disputation: Prof. Dr. Joachim Mnich  
Jun.-Prof. Dr. Johannes Haller

Datum der Disputation: 17. Dezember 2008

Vorsitzender des Prüfungsausschusses: Dr. Georg Steinbrück  
Vorsitzender des Promotionsausschusses: Prof. Dr. Joachim Bartels

Leiter des Departments Physik: Prof. Dr. Robert Klanner  
Dekan der MIN-Fakultät: Prof. Dr. Arno Frühwald

## Abstract

Semileptonic top quark pair decays are analysed using full simulation of the CMS detector at the proton–proton collider LHC. A complete analysis of event selection and reconstruction is performed with the goal of the determination of differential cross sections. Special emphasis is put on object reconstruction and an efficient and unbiased event selection procedure.

The reconstruction of semileptonic  $t\bar{t}$  decays uses the full combination of all reconstruction objects. These objects are specifically defined and analysed in their reconstruction performance. For this several methods are developed and implemented. A highly efficient electron identification and a clear procedure of lepton isolation are defined.

Two selections are compared, a cut-based and a neural network-based selection with a common efficiency of 10%. For the event selection and reconstruction a kinematic fit is implemented. As final step the  $t\bar{t}$  spectra of rapidity, invariant mass and transverse momentum are analysed.



## Zusammenfassung

Unter Verwendung der detaillierten Simulation des CMS Detektors am Large Hadron Collider werden Top Quark Paare im semileptonischen Zerfallskanal untersucht. Die vollständige Analyse ist auf das Ziel der Bestimmung differentieller Wirkungsquerschnitte ausgerichtet. Besondere Bedeutung wird dabei sowohl auf die Definition der initialen Rekonstruktionsobjekte gelegt, als auch auf die Formulierung einer unverfälschten und effizienten Ereignisselektion.

Der semileptonische Zerfall von  $t\bar{t}$  ist in mehrfacher Hinsicht ausgezeichnet geeignet für eine solche Betrachtung. In Erwartung der hohen Produktionsrate am LHC handelt es sich bei der Beschäftigung mit dem schwersten bekannten Teilchen physikalisch um ein höchst interessantes Experimentierfeld. Auf der Seite der Rekonstruktion werden nahezu alle Objekte benötigt, die überhaupt rekonstruiert werden. Die exakte Definition von rekonstruierten Objekten wie Leptonen oder Jets wird deshalb ausführlich behandelt. Unter anderem werden eine hocheffiziente Methode zur Elektronidentifikation, sowie eine Prozedur zur Isolation von Leptonen beschrieben.

Es werden zwei verschiedene Verfahren zur Ereignisselektion entworfen und bei einer Selektionseffizienz von 10 % verglichen; eine schnittbasierte Methode sowie ein neuronales Netz. Für die Selektion und die finale Ereignisrekonstruktion wird ein kinematischer Fit entwickelt. Als Test der kompletten Kette werden die differentiellen Verteilungen in Rapidität, invarianter Masse und transversalem Impuls des  $t\bar{t}$  Systems analysiert.



# Contents

<b>1</b>	<b>Introduction</b>	<b>1</b>
<b>2</b>	<b>The Top Quark and the Standard Model</b>	<b>3</b>
2.1	The Standard Model of Particle Physics . . . . .	3
2.1.1	Electroweak interaction . . . . .	5
2.1.2	Strong interaction . . . . .	12
2.2	The Top Quark . . . . .	16
2.2.1	Basic Properties . . . . .	16
2.2.2	Cross section . . . . .	19
<b>3</b>	<b>The Experimental Setup</b>	<b>23</b>
3.1	The Large Hadron Collider . . . . .	23
3.2	The Compact Muon Solenoid . . . . .	26
3.2.1	CMS coordinate system . . . . .	27
3.2.2	Solenoid . . . . .	28
3.2.3	Tracking System . . . . .	28
3.2.4	Calorimeters . . . . .	35
3.2.5	Luminosity Monitoring . . . . .	38
3.2.6	Trigger and Data Acquisition . . . . .	40
<b>4</b>	<b>Event Generation, Simulation and Object Reconstruction</b>	<b>43</b>
4.1	Event Generation and Detector Simulation . . . . .	43

4.2	Object Reconstruction . . . . .	44
4.2.1	Muon Identification and Reconstruction . . . . .	44
4.2.2	Electron Reconstruction . . . . .	49
4.2.3	Electron Identification . . . . .	52
4.2.4	Jet Reconstruction . . . . .	62
4.2.5	B-Jet Identification . . . . .	66
4.2.6	Missing Transverse Energy Reconstruction . . . . .	68
<b>5</b>	<b>Event Selection and Interpretation</b>	<b>71</b>
5.1	Preselection step . . . . .	73
5.1.1	Lepton Selection . . . . .	73
5.1.2	Jet Selection . . . . .	74
5.1.3	Preselection Summary . . . . .	76
5.2	Selection . . . . .	78
5.2.1	Cut-based Selection . . . . .	85
5.2.2	Neural Network Selection . . . . .	89
5.2.3	Selection Summary . . . . .	93
5.3	Event Interpretation . . . . .	94
<b>6</b>	<b>Differential Distributions of <math>t\bar{t}</math> pairs</b>	<b>99</b>
6.1	Summary . . . . .	110
<b>7</b>	<b>Conclusion and Outlook</b>	<b>111</b>
7.1	Conclusion . . . . .	111
7.2	Outlook . . . . .	112
	<b>Appendix</b>	<b>115</b>
<b>A</b>	<b>Electron Likelihood technique</b>	<b>115</b>
<b>B</b>	<b>Electron Probability Density Functions</b>	<b>116</b>

C Least Square fitting with external constraints	121
D Artificial Neural Networks	123
E Identification of $\tau$ -jets	127
Bibliography	133



# Chapter 1

## Introduction

In this thesis semileptonic top quark pair decays are analysed, using full simulation of the CMS detector at the Large Hadron Collider. The main motivation is the thorough preparation for the analysis of detector data after the start of collisions in 2009.

The topic of the determination of differential cross section in the semileptonic  $t\bar{t}$  decay is suited most outstandingly. A complete analysis is given for the feature extraction and error estimation based on the simulation. It is a manifold test of the reliability of the simulation and reconstruction chain. Some of the major challenges are identified, which provides a guideline for dealing with detector data.

The specific topic combines the theoretical and experimental aspects most beneficially. The top quark is the heaviest known particle, and discovered only in 1995. Many of its features are not yet fully known, or at least not very accurately. Especially the analysis of differential properties is suited to prove if the underlying model is correct, or if it needs to be modified. The high mass relates it also directly to the solution of the problem of mass generation. The production mechanism is dominated by quantum chromodynamics at the LHC, whereas its decay properties are completely determined by the electroweak interaction. It is the only quark that decays before it hadronises, passing its spin information directly on to its daughter particles.

In the experimental detection mechanism and the subsequent reconstruction basically all parts are involved. The reconstruction of an electron or a muon as lepton, the jets as hadronic objects and additional tagging information needs input of all parts of the detector. Whereas detector data is not available yet, the simulation and the reconstruction software is checked thoroughly.

The LHC imposes large challenges for the event reconstruction and selection. The semileptonic  $t\bar{t}$  decay is the most promising of all  $t\bar{t}$  decays. About 30% of all top quark pairs

decay into a muon or an electron plus additional jets, where the lepton is both well identifiable and reconstructable. The statistically more important full hadronic decay mode is very hard to identify and very complicated in its reconstruction. The fully leptonic decay mode is less likely to occur, but much easier to select. But these decays are kinematically less constrained due to a second escaping neutrino, making full event reconstruction highly speculative.

The determination of production cross sections is complementary to mass measurements. Furthermore differential cross sections are the extension of the measurement of the total cross section.

Only with the large statistics that are expected at the LHC this will become possible for  $t\bar{t}$  decays. Still the analysis of semileptonic  $t\bar{t}$  decays will remain a complex task. The determination of differential cross sections builds heavily upon the exact and bias-free reconstruction of the physics objects. Also a selection method is needed, that is highly efficient and at the same time unbiased. The event reconstruction itself is also challenging, due to number of possibilities to combine the measured jets to the final system.

After a short description of the Standard Model and Top Quark physics in chapter 2 the Large Hadron Collider and the CMS detector are described in chapter 3. Then the full analysis is given in the logical sequence of execution. The first of the two central parts is the definition of all physics objects that are used in the analysis, given in chapter 4. In this a complete electron identification based on a likelihood method is presented in detail, as well a procedure for the definition of lepton isolation. Also a jet energy correction method is developed. The second central part consists of the detailed description of the selection in chapter 5, where also the event reconstruction method is presented. Two selection methods are compared, a cut-based and a neural network-based approach. The differential cross sections of the  $t\bar{t}$  system in rapidity, invariant mass and transverse momentum are analysed as test of the whole procedure in chapter 6.

As usual in elementary particle physics natural units are used with

$$\hbar = c = 1.$$

If not explicitly commented the conjugate particle is usually implied whenever pairs of particles and decays are given.

# Chapter 2

## The Top Quark and the Standard Model

The top quark plays a prominent role in the theoretical foundation of elementary particle physics, the Standard Model. Production and decay properties of top quark pairs link fundamental parts of this theory together. In the first part of this chapter the underlying physical framework is described. The second part focuses on the experimental and theoretical aspects of top quark physics.

### 2.1 The Standard Model of Particle Physics

The Standard Model of Particle Physics is the theoretical description of all known interactions of elementary particles. Here a brief overview is presented, more extensive literature exists for example in [1]. Emphasis is put on the aspects and relations most relevant to the top quark.

The theory can be divided into a description of the particles involved and the forces acting upon them. Interactions are described by the exchange of particles, where all particles are described by fields in a quantum field theory. The Standard Model is built on three main pillars:

- Fermion fields are the building blocks of matter.
- One basic symmetry principle, the local gauge invariance of the free fermion fields, which introduces two interactions by exchange of vector gauge bosons.
- The breaking of electroweak symmetry, which introduces mass and the hypothetical Higgs boson.

The Higgs boson is the only particle within the Standard Model that has not yet been discovered in an experiment. Due to its fundamental structural importance to the Standard Model a more detailed description of the Higgs mechanism is given.

Gravity is excluded from the current model of interactions due to its relative weakness and currently unsolvable complications. Unifications that include gravity exist, for example in String theory, but have no computable applications to particle physics yet.

## Fermions

Fermions are particles that carry half-integer spin. All known matter is made of fermions with spin  $\frac{1}{2}$ . Two basic families of fermions exist, quarks and leptons. Leptons take only part in the electroweak interaction. Quarks additionally participate in the strong interaction. All fundamental fermions are point-like objects, which is experimentally confirmed to the order of  $10^{-18}$  m. The current experimental knowledge about the mass and electric charge of the fermions is shown in table 2.1. The experimental error on the values is omitted for simplicity. In case of the top quark charge the value is not experimentally confirmed, but only assumed [2].

## Quantum field theory

Modern elementary particle physics is described by a quantised relativistic field theory. In analogy to classical mechanics the Lagrangian formalism is used. The starting point in the description is the Lagrangian density  $\mathcal{L}$  as a function of the fields  $\phi_i$  and their derivatives in  $(\vec{x}, t)$ .

Leptons			Quarks		
	mass[ MeV]	charge [e]		mass[ MeV]	charge [e]
$\nu_e$	$< 5 \cdot 10^{-6}$	0	up	1.5-3	+2/3
electron	0.511	-1	down	3-7	-1/3
$\nu_\mu$	$< 0.27$	0	charm	95	+2/3
muon	105.7	-1	strange	1250	-1/3
$\nu_\tau$	$< 31$	0	top	171200	+2/3(?)
tauon	1777	-1	bottom	4200	-1/3

**Table 2.1:** Mass and electric charge of the fundamental fermions. For the quarks they are given as *current-quark masses* in the  $\overline{\text{MS}}$ -scheme [3].

## Local Gauge Invariance

All interactions within the Standard Model can be derived by the fundamental principle of local gauge invariance. More precisely, the free Dirac Lagrangian density is demanded to be locally gauge invariant.

The two basic symmetry groups in the Standard Model are:

- $SU(2)_L \otimes U(1)_Y$ , which is the basis for the electroweak interaction, the unification of weak and electromagnetic interactions. The bosons are the photon and the heavy gauge bosons  $W^\pm$  and  $Z$ .
- $SU(3)_C$ , which describes the strong interaction by exchange of gluons in quantum chromodynamics (QCD).

Fundamental to a consistent and successful theoretical description of experimental observation is the renormalisability of the theory. This means that any calculable observable is finite in any order of perturbation calculation. It has been proven that local gauge invariance ensures the renormalisability [4].

### 2.1.1 Electroweak interaction

The Standard Model of electroweak interaction is the unified description of the electromagnetic and weak interaction. It describes these interactions by the exchange of Spin-1 particles, namely the photon and the heavy gauge bosons  $W^\pm$  and  $Z$ . The unification of electromagnetism and the weak interaction was formulated by Glashow, Salam and Weinberg (GSW) [5].

The fermions can be assigned the quantum numbers of the weak isospin  $\vec{T}$  and the weak hypercharge  $Y$ . The electric charge of the fermions is related to quantum numbers by the Gell-Mann–Nishijima-Relation, where  $T_3$  corresponds to the third component of the weak isospin:

$$Q = T_3 + \frac{Y}{2}.$$

Under gauge transformations the left-handed components of fermion fields form isospin doublets, while the right-handed components form singlets. The resulting structure of electroweak quantum numbers to the fundamental fermions is given in table 2.2.

The symmetry group  $SU(2)_L \otimes U(1)_Y$  is generated by four fields (three plus one). The weak isospin  $\vec{T}$  is generated by the three non-abelian fields  $W_\mu^i$ . The generator of the weak hypercharge  $Y$  is usually denoted as  $B_\mu$ .

Including the propagation of the boson fields, the resulting Lagrangian density is:

$$\mathcal{L}_{EW} = -\frac{1}{4}B_{\mu\nu}B^{\mu\nu} - \frac{1}{4}W_{\mu\nu}^j W_j^{\mu\nu} + \{\text{interaction terms}\}.$$

The non-abelian structure leads to a self-coupling of the gauge bosons. Resolving the tensor products yields Feynman diagrams as shown in figure 2.1.

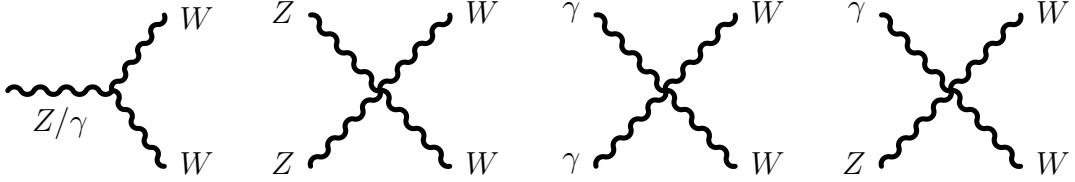


**Figure 2.1:** The Feynman graphs of the self-coupling of the electroweak gauge bosons.

The mass eigenstates and therefore the physically observable fields are rotations of the  $\vec{W}_\mu$  and  $B_\mu$  fields:

$$\begin{aligned} \begin{pmatrix} W_\mu^+ \\ W_\mu^- \end{pmatrix} &= \frac{1}{\sqrt{2}} \begin{pmatrix} 1 & -1 \\ 1 & 1 \end{pmatrix} \begin{pmatrix} W_\mu^1 \\ W_\mu^2 \end{pmatrix}, \\ \begin{pmatrix} Z_\mu \\ A_\mu \end{pmatrix} &= \begin{pmatrix} \cos \vartheta_W & -\sin \vartheta_W \\ \sin \vartheta_W & \cos \vartheta_W \end{pmatrix} \begin{pmatrix} W_\mu^3 \\ B_\mu \end{pmatrix}. \end{aligned} \quad (2.1)$$

Equation (2.1) introduces a parameter of the Standard Model of electroweak interactions, the weak mixing angle  $\sin \vartheta_W$ . The two coupling constants  $g$  and  $g'$  are connected to the electric charge  $e$  (or the electromagnetic coupling constant  $\alpha = e^2/4\pi$ ):

$$e = g \sin \vartheta_W = g' \cos \vartheta_W.$$

	$T$	$T_3$	$Y$	$Q$		
$\begin{pmatrix} \nu_e \\ e \end{pmatrix}_L$	$\begin{pmatrix} \nu_\mu \\ \mu \end{pmatrix}_L$	$\begin{pmatrix} \nu_\tau \\ \tau \end{pmatrix}_L$	1/2	+1/2	-1	0
$\begin{pmatrix} u \\ d' \end{pmatrix}_L$	$\begin{pmatrix} c \\ s' \end{pmatrix}_L$	$\begin{pmatrix} t \\ b' \end{pmatrix}_L$	1/2	-1/2	-1	-1
$\begin{pmatrix} u \\ d' \end{pmatrix}_L$	$\begin{pmatrix} c \\ s' \end{pmatrix}_L$	$\begin{pmatrix} t \\ b' \end{pmatrix}_L$	1/2	+1/2	+1/3	+2/3
$\begin{pmatrix} u \\ d' \end{pmatrix}_L$	$\begin{pmatrix} c \\ s' \end{pmatrix}_L$	$\begin{pmatrix} t \\ b' \end{pmatrix}_L$	1/2	-1/2	+1/3	-1/3
$e_R$	$\mu_R$	$\tau_R$	0	0	-2	-1
$\nu_{e,R}$	$\nu_{\mu,R}$	$\nu_{\tau,R}$	0	0	0	0
$u_R$	$c_R$	$t_R$	0	0	+4/3	+2/3
$d'_R$	$s'_R$	$b'_R$	0	0	-2/3	-1/3

**Table 2.2:** The electroweak quantum numbers  $Y$  and  $T_3$  of the fundamental fermions as assigned by the theory.

As an additional complication the weak eigenstates of the quarks are not identical to the mass eigenstates. This can be expressed by rotating their weak eigenstates by a unitary transformation. By convention the left-handed quarks with  $T_3 = -1/2$  ( $d'$ ,  $s'$  and  $b'$ ) are assigned as the weak eigenstates of the  $d$ ,  $s$  and  $b$  quarks. The observed rotation is thus parametrised by the Cabibbo-Kobayashi-Maskawa (CKM) mixing matrix:

$$\begin{pmatrix} d' \\ s' \\ b' \end{pmatrix} = V_{CKM} \cdot \begin{pmatrix} d \\ s \\ b \end{pmatrix} = \begin{pmatrix} V_{ud} & V_{us} & V_{ub} \\ V_{cd} & V_{cs} & V_{cb} \\ V_{td} & V_{ts} & V_{tb} \end{pmatrix} \begin{pmatrix} d \\ s \\ b \end{pmatrix}.$$

The CKM matrix elements are therefore related to the probabilities of flavor-changing decays. The matrix element  $V_{tb}$  is very close to unity, although this is not experimentally confirmed, but inferred from assuming unitarity of the CKM matrix.

Recent experiments show that also neutrino mixing occurs [6]. Since the effect is rather small in high energy experiments, the mixing is usually omitted. Nevertheless it shows that neutrinos have a mass and that their mass eigenstates are not the weak eigenstates, similar to the quark sector. This implies a similar mixing matrix called the Maki-Nakagawa-Sakata (MNS) matrix. In contrast to the relatively small mixing in the quark sector, mixing seems to be much stronger for neutrinos.

One of the fundamental problems of the GSW model is that naive mass terms in the Lagrangian density break local gauge invariance. But experimental observation clearly finds both vector bosons (like the  $Z$ ) and fermions (like the top quark) to be massive. The solution within the Standard Model is the Higgs mechanism. It explains how particles acquire mass dynamically through the interaction with a scalar field in a way that leaves the local gauge invariance intact.

## The Higgs mechanism

The Higgs field is a scalar field with a potential  $V(\phi)$ . In the minimal Standard Model the choice is a complex, scalar isospin doublet field

$$\phi = \frac{1}{\sqrt{2}} \begin{pmatrix} \phi_1 + i\phi_2 \\ \phi_3 + i\phi_4 \end{pmatrix} = \begin{pmatrix} \phi^+ \\ \phi^0 \end{pmatrix}.$$

with the symmetric potential

$$V(\phi) = \mu^2 \phi^\dagger \phi + \lambda (\phi^\dagger \phi)^2.$$

This is the most simple non-trivial choice of a potential that generates masses in the Lagrangian densities. To ensure the physical behaviour of  $V \rightarrow \infty$  for  $\phi \rightarrow \pm\infty$  the real

parameter  $\lambda$  must be positive. In case of  $\mu^2 < 0$  the minimum of  $V(\phi)$  is no longer at  $\phi = 0$ , but at the non-vanishing vacuum expectation value

$$\phi_{\min} = \pm \sqrt{\frac{-\mu^2}{\lambda}} = \pm v.$$

The initial symmetry can now be broken spontaneously by choosing a vacuum ground state. In agreement with experimental observation this is chosen in a way that the photon remains massless, which is achieved by setting only  $\phi_3 \neq 0$ . This leaves three degrees of freedom, which are absorbed in the additional longitudinal polarization states of the three heavy gauge bosons.

The expansion around the ground state and the introduction of another scalar field  $h(x)$  along  $\phi_3$  leads to

$$\phi = \frac{1}{\sqrt{2}} \begin{pmatrix} 0 \\ v + h(x) \end{pmatrix}.$$

By the choice of this potential another particle is introduced, the Higgs boson. It can be described using the Klein-Gordon Lagrangian density for a scalar spin-0 field  $\phi$ , characterising a spin-0 particle of mass  $m$

$$\mathcal{L}_{\text{Klein-Gordon}} = \frac{1}{2} (\partial_\mu \phi) (\partial^\mu \phi) - \frac{1}{2} m^2 \phi^2.$$

The resulting structure of the full Higgs Lagrangian density is then

$$\begin{aligned} \mathcal{L}_{\text{Higgs}} = & \frac{1}{2} (\partial_\mu h) (\partial^\mu h) + \{\text{mass terms}\} + \{\text{const. term}\} \\ & + \{\text{trilinear couplings}\} + \{\text{quadrilinear couplings}\}. \end{aligned}$$

The terms are

$$\begin{aligned} \text{mass terms} &= -\lambda v^2 h^2 + \frac{1}{4} g^2 v^2 W_\mu^+ W^{-\mu} + \frac{1}{8} (g^2 + g'^2) v^2 Z_\mu Z^\mu, \\ \text{trilinear couplings} &= -\lambda v^2 h^3 + \frac{1}{2} g^2 v h W_\mu^+ W^{-\mu} + \frac{1}{4} (g^2 + g'^2) v h Z_\mu Z^\mu, \\ \text{quadrilinear couplings} &= -\frac{1}{4} \lambda v^2 h^4 + \frac{1}{2} g^2 h^2 W_\mu^+ W^{-\mu} + \frac{1}{8} (g^2 + g'^2) h^2 Z_\mu Z^\mu. \end{aligned}$$

The coupling terms describe the coupling to the massive bosons and the self-coupling of the Higgs field. The corresponding Feynman diagrams are shown in figure 2.2. This choice of the Higgs field determines the masses of the gauge bosons to be

$$m_W = \frac{1}{2} g v = \frac{e v}{2 \sin \vartheta_W}, \quad (2.2)$$

$$m_Z = \frac{1}{2} v \sqrt{g^2 + g'^2} = \frac{e v}{2 \sin \vartheta_W \cos \vartheta_W}, \quad (2.3)$$

$$m_\gamma = 0.$$

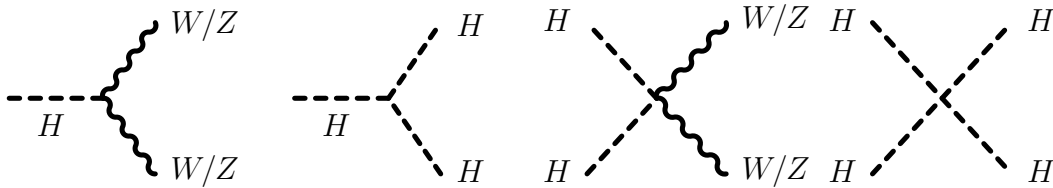


**Figure 2.2:** The trilinear and quadrilinear Higgs couplings to the gauge bosons and the Higgs itself in terms of the respective Feynman diagrams.

While no compelling reason exists that the fermions acquire mass by coupling to the same Higgs field, usually this is chosen as the most simple realisation. The choice of only one doublet field is called the minimal Standard Model. Indicator of the coupling strength is the Yukawa coupling  $\lambda_f$ , in combination with the vacuum expectation value  $v$ :

$$m_f = \lambda_f \frac{v}{\sqrt{2}}.$$

These masses are not determined by the theory but must be determined experimentally. The vacuum expectation value  $v$  can be calculated by using the already measured quantities  $m_Z$ ,  $m_W$  and  $\cos\vartheta$  to be

$$v \cong 246 \text{ GeV}.$$

Within this description the top quark has the largest coupling constant  $\lambda_t \approx 1$ , rendering it the heaviest known fermion. A direct measurement of the coupling of the top quark to the Higgs boson would help to clarify if one doublet Higgs field gives mass both to the gauge bosons and the fermions. An example would be the measurement of associated production in  $t\bar{t}H$ .

The equations (2.2) and (2.3) yield an important relationship valid for the Higgs mechanism. The Veltman parameter  $\rho$  is defined as

$$\rho = \frac{m_W^2}{m_Z^2 \cos^2 \vartheta_W}. \quad (2.4)$$

A prominent feature of all models that contain only Higgs doublets (including the minimal Standard Model) is that  $\rho = 1$  holds in all orders of perturbation theory in the on-shell scheme. Then equation (2.4) can serve as a definition of the weak mixing angle

$$\cos \vartheta = \frac{m_W}{m_Z}.$$

Up to now the Higgs boson has not been observed. Its mass is an independent parameter which has to be measured. Direct searches from the Large Electron Positron Collider (LEP) have set a lower limit on the Higgs mass of 114.4 GeV [7].

Structurally the Higgs mechanism is vitally important for the Standard Model. The dynamic generation of particle masses makes the connection to the top quark as the heaviest known particle especially prominent.

Two relationships give an estimate of the possible mass of the Higgs boson within the Standard Model. The first sets an upper limit to the Higgs mass. The contributions of the two first diagrams for the scattering of longitudinally polarised  $W^\pm$  and  $Z$  bosons in figure 2.3 are divergent. More precisely, they exceed the unitary limit. This means that the probability rises above unity, since its cross section has the proportionality

$$\sigma \propto \frac{s}{m_W^2}.$$

A solution is the inclusion of the contribution of the Higgs boson in the third Feynman diagram in figure 2.3. This means something like a Higgs boson is required for the inner consistency of the theory. It additionally sets an upper limit to the Higgs mass for achieving this

$$m_H < 1 \text{ TeV}.$$

This is not simply a theoretical implication, since results from LEP have shown that longitudinally polarised bosons exist [8].

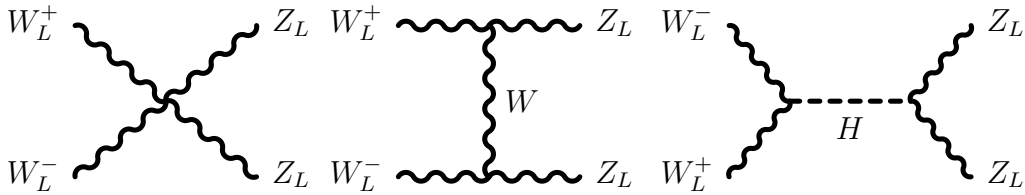


**Figure 2.3:** The three feynman graphs contributing to the scattering of longitudinally polarised  $W^\pm$  and  $Z$  bosons.

The second relationship for a mass estimate of the Higgs boson is more complicated. It relates the masses of the  $W$  boson, the top quark and the Higgs boson. In high  $Q^2$  collision the relation between the Fermi constant  $G_F$ , the weak mixing angle and the boson masses is modified by radiative corrections  $\Delta r$ .

$$\frac{G_F}{\sqrt{2}} = \frac{\pi\alpha}{2m_W \sin^2 \vartheta_W} \frac{1}{1 - \Delta r} \quad (2.5)$$

These corrections have been calculated initially by Veltman, Marciano, Sirlin and others [9]. The corrections include the running of the fine-structure constant  $\alpha$  and modifications to the  $\rho$ -parameter of equation (2.4)

$$\Delta r = \Delta\alpha + \cot^2 \vartheta_W \Delta\rho + \dots \quad (2.6)$$

The leading contribution is the influence of the top quark mass  $m_t$  to the W boson propagator as shown in figure 2.4a). This is the so-called W boson self energy, which arises from the large difference between the top and bottom quark mass

$$\Delta\rho_t = \frac{3G_F}{8\pi^2\sqrt{2}} \left( m_t^2 + m_b^2 - 2\frac{m_t^2 m_b^2}{m_t^2 - m_b^2} \ln \frac{m_t^2}{m_b^2} \right) \approx \frac{3G_F}{8\pi^2\sqrt{2}} m_t^2, \quad \text{for } m_b^2 \ll m_t^2.$$

The Feynman diagram for self energy of the Higgs boson is shown in figure 2.4b). The associated radiative correction depends only logarithmically on the masses of the vector bosons:

$$\Delta\rho_H = -\frac{3G_F}{8\pi^2\sqrt{2}} (m_Z^2 + m_W^2) \left( \ln \frac{m_H^2}{m_W^2} - \frac{5}{6} \right)$$

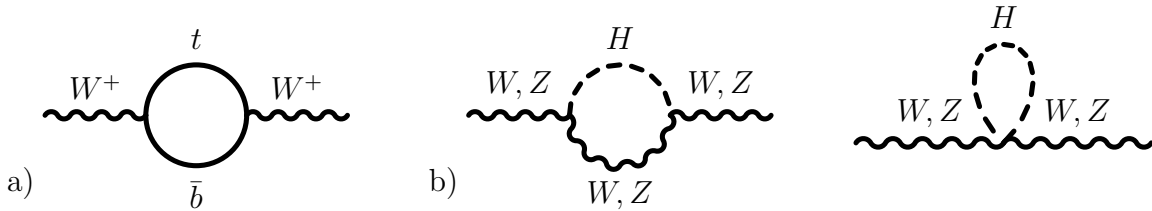


**Figure 2.4:** a) The leading contribution to the modification of the W boson self energy. The main source is the large mass difference of the top and the b quark. b) The two leading contributions to the Higgs self energy.

Using equation (2.5) it is possible to deduce the value of the unknown Higgs mass from careful measurement of electroweak observables. The two corrections  $\Delta\rho_t$  and  $\Delta\rho_H$  correlate the masses of the W boson  $m_W$ , the top quark  $m_t$  and the Higgs boson  $m_H$ . The relations can be expressed graphically. Figure 2.5a) shows the  $1\sigma$  fit contours of LEP, SLD and Tevatron data to  $m_W$  and  $m_t$ . Below the fit contours different Higgs mass hypotheses are shown. Assuming that the true values are approximately within the contour, a Higgs mass of at most a few hundred GeV is suggested. Another way to predict the Higgs mass is to simultaneously fit all measured parameters of the electroweak Standard Model to extract the unknown Higgs mass. Figure 2.5b) shows the  $\Delta\chi^2$  versus different Higgs mass hypotheses, indicating the most likely Higgs mass. This is the difference between the best  $\chi^2$  value and the computed  $\chi^2$  value at a given mass. The different lines show different input data and different extraction methods for the input parameters. The yellow area shows the excluded region from direct searches at LEP. One of the main influences on the graph is the top quark mass. The central value of the top quark mass determines mostly the position of the minimum of the fit parabola. The relatively large error on the top quark mass has a large influence on the width of the fit parabola.

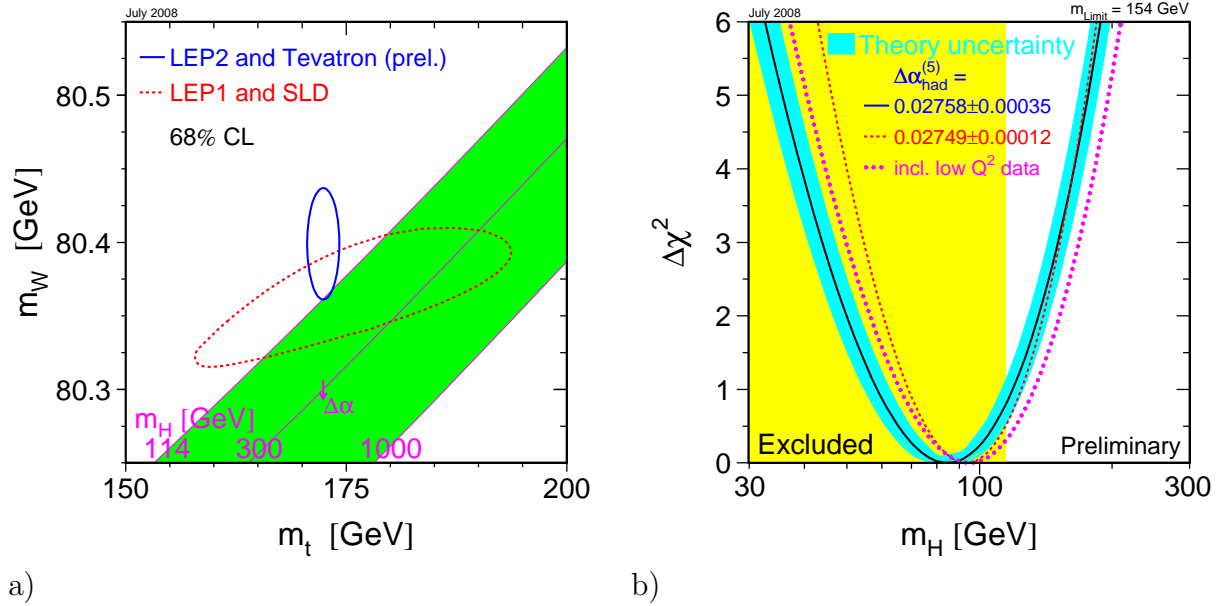


**Figure 2.5:** a) The  $1\sigma$  contours of simultaneous fitting of  $m_W$  and  $m_t$  to LEP, SLD and Tevatron data. Additionally the Higgs mass regions are shown below the contours. The direction of change of  $\Delta\alpha$  of equation (2.6) is also given for reference. b)  $\Delta\chi^2 = \chi^2_{min} - \chi^2(m_H)$  versus  $m_H$  from a global fit to electroweak data. Different line colours correspond to different data input. The yellow region is excluded by direct searches from LEP[10].

### 2.1.2 Strong interaction

The quantum field description of the strong interaction is called Quantum Chromodynamics (QCD). It describes the interactions between gluons and quarks and the resulting confinement of quarks into hadrons. Gluons are the Spin-1 gauge bosons of the strong force.

The basic structure of QCD is defined by the theory of the non-abelian gauge group of  $SU(3)_C$ . Each quark has exactly one of three possible colour eigenstates, usually called red, green and blue. Leptons remain colourless (they are colour singlets), and therefore remain unaffected by colour transformations. The Lagrangian density of QCD is given by

$$\mathcal{L}_{QCD} = \bar{\chi} (i\gamma^\mu \partial_\mu - m) \chi - g_s \bar{\chi} \gamma^\mu T_a \chi G_\mu^a - \frac{1}{4} G_{\mu\nu}^a G_a^{\mu\nu}.$$

The strong coupling constant  $\alpha_s$  is connected to the gluon field coupling  $g_s$  by:

$$\alpha_s = \frac{g_s^2}{4\pi}.$$

The value of  $\alpha_s$  depends on the momentum transfer  $Q^2$ . This so-called running of the coupling constant is similar to the electromagnetic coupling, but exhibits a fundamentally different dependence. At low values of  $Q^2$ ,  $\alpha_s$  is very large, and it approaches zero for very high  $Q^2$ , leading to the asymptotic freedom of quarks at high  $Q^2$ .

Direct experimental analysis of free quarks is therefore impossible, quarks are confined to bound states in hadrons. Hadrons can be divided into baryons, bound states of three quarks, and mesons, bound states of a quark and an anti-quark. This is usually expressed as postulation that only colourless particles can exist freely (anti-quarks carry anti-colour).

The non-abelian structure of the gauge group leads to a self-coupling of the gluon fields. The resulting Feynman graphs are shown in figure 1.6.



**Figure 2.6:** The Feynman diagrams of the gluon self-coupling in the Lagrangian density.

Gluons are assumed to be massless. There is no possibility to include a massive term in the Lagrangian that leaves it locally gauge invariant. Each of the gluons carries colour and anti-colour. The nine possible combinations of the colour generators decompose into an octet of colour–anti-colour combinations, and one singlet that is invariant under colour transformations. It can be deduced from experimental observation that the colour singlet of gluons is not realised in nature [1].

## The proton

The proton is the most important bound state of quarks. Some basic information is given here, because protons are the initial particles for the analysed process.

In the most simple view the proton is a bound state of two up quarks and one down quark (uud). But actually a proton has a very complicated structure due to the fact that it is a bound state of particles that interact both via strong and electroweak interaction. In a slightly better approximation the proton is made up of partons, namely quarks and

gluons. The experimental key to the proton structure is the deep inelastic scattering of point-like particles like electrons with protons (and neutrons). The basic process is shown in figure 2.7.

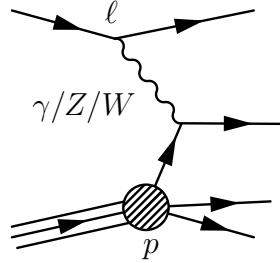


**Figure 2.7:** The basic process of deep inelastic scattering (DIS): an incoming lepton exchanges a boson ( $\gamma$ ,  $W$  or  $Z$ ) with a quark.

Two main variables  $x$  and  $Q^2$  are used in the description of the proton as a composition of partons. The parton momentum  $x$  is expressed as the fraction of the total proton momentum, ranging between zero and one.  $Q^2$  is the momentum transfer from the lepton to the interacting parton. The proton is usually described with two structure functions  $F_1(x, Q^2)$  and  $F_2(x, Q^2)$ . They are parametrisations of the proton as seen by the lepton. Experiments to measure the structure functions were for example performed at the Hadron-Elektron-Ring-Anlage (HERA) located at DESY (Deutsches Elektronen-Synchrotron) in Hamburg.

These and other experiments have shown that the proton does not consist of three static valence quarks (uud). In addition there are sea quarks and gluons present. The sea quarks are quark–anti-quark pairs into which the gluons may split. The summed momenta of all quarks is only little more than half of the total momentum of the proton. The rest of the proton momentum is carried by the gluons. The structure functions are composed of parton density functions (PDFs) which describe the probability to find a parton with a certain  $x$  in the proton at a given scale  $\mu$ . The PDF extraction from experimental data is a complicated fit, where the gluon part is determined indirectly. Their contribution is calculated under the assumption of certain models.

The gluons have a special role in these evolution models of parton densities. The reaction kinematics do not only depend on the momentum fraction  $x$  of the quark, but also on the momentum transfer  $Q^2$ . This dependence is only logarithmic, being proportional to

$$\alpha_s \ln Q^2.$$

This scaling violation can be used in combination with an evolution scheme to extract the parton density distributions. The schematic form of the evolution in the scale of the

momentum transfer  $\mu^2$  is in leading order (LO)

$$\frac{\partial f_a}{\partial \ln \mu^2} \sim \frac{\alpha_S(\mu^2)}{2\pi} \sum_b (P_{ab} \otimes f_b).$$

It describes the evolution of the parton distribution  $f_a$  using the splitting functions  $P_{ab}$  that describe the transition of a parton  $a$ . The leading order splitting functions are the transitions quark-quark  $P_{qq}$ , quark-gluon  $P_{qg}$ , gluon-quark  $P_{gq}$  and gluon-gluon  $P_{gg}$ .

Usually the parton distribution functions are given in sets, that follow certain extraction rules and use certain fixed sets of parameters. In figure 2.8 an example of a certain pdf set is shown.

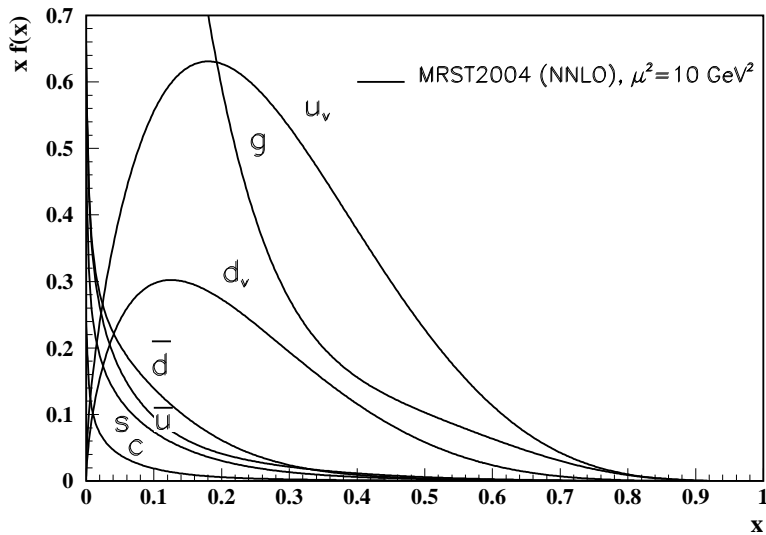


**Figure 2.8:** Parton distribution functions of the valence quarks  $u_v, d_v$ , the gluons  $g$  and the sea quarks  $\bar{u}, \bar{d}, s, c$ . The NNLO MRST 2004 parametrisation is used at scale  $\mu^2 = 10 \text{ GeV}^2$  [11].

## 2.2 The Top Quark

Within the Standard Model the top quark is the weak isospin doublet partner of the bottom quark. It has the electric charge of  $q = 2/3$ , the weak hypercharge  $Y = 1/3$  and is the member of a colour triplet. The existence of a third quark generation (including the top) had been assumed before even the second generation of particles was completely discovered. High precision measurements at LEP indicated a very heavy doublet partner quark for the bottom quark [12]. It eluded direct detection until the Tevatron, a  $p\bar{p}$  collider, was the first to provide the necessary energy and luminosity to produce top quark pairs. In 1995 the two experiments CDF and D0 at the collider at Fermilab finally announced the discovery [13]. The most accurately known property of the top quark is its mass. The current world average value is  $m_t = (171.2 \pm 2.1)$  GeV [3].

In addition to the mass also the total pair production cross section in  $p\bar{p}$  collisions at the Tevatron is measured [14, 15]. Recent measurements at the Tevatron give indication of single top production [16]. Ultimately measurements at the Tevatron are statistically limited, due to the relative small production cross section.

The Large Hadron Collider will provide much higher statistics, due to its higher luminosity and a larger production cross section. The total production cross section is more than two orders of magnitude higher than at the Tevatron due to the centre-of-mass energy of 14 TeV, shown in figure 2.9. Production cross sections decrease with  $1/s$  for a given centre-of-mass energy  $s$  above the production threshold. But this reduction is overcompensated for the top pair production by the much higher abundance of partons above the production threshold of required momentum. In the following subsections mostly the properties of top quark pair production and decays are presented.

### 2.2.1 Basic Properties

Under the assumption of the Standard Model the CKM matrix elements yield the possible decay channels and their relative fractions. Cross-generation decays into a s-quark or a d-quark almost never occur. The branching ratio for the decay  $t \rightarrow Wb$  is at least 99.8% (from current measurements [3]). For the purposes of this thesis this ratio can safely be assumed to be one. The value of  $|V_{tb}|$  is not yet measured directly, its value is inferred from measurement of the related CKM values and assuming the matrix to be unitary. Measurement of single top decays can provide a direct measurement, which will likely be performed at the LHC.

An intermediate state of top quark pair decays is

$$t\bar{t} \rightarrow b\bar{b}W^+W^-.$$

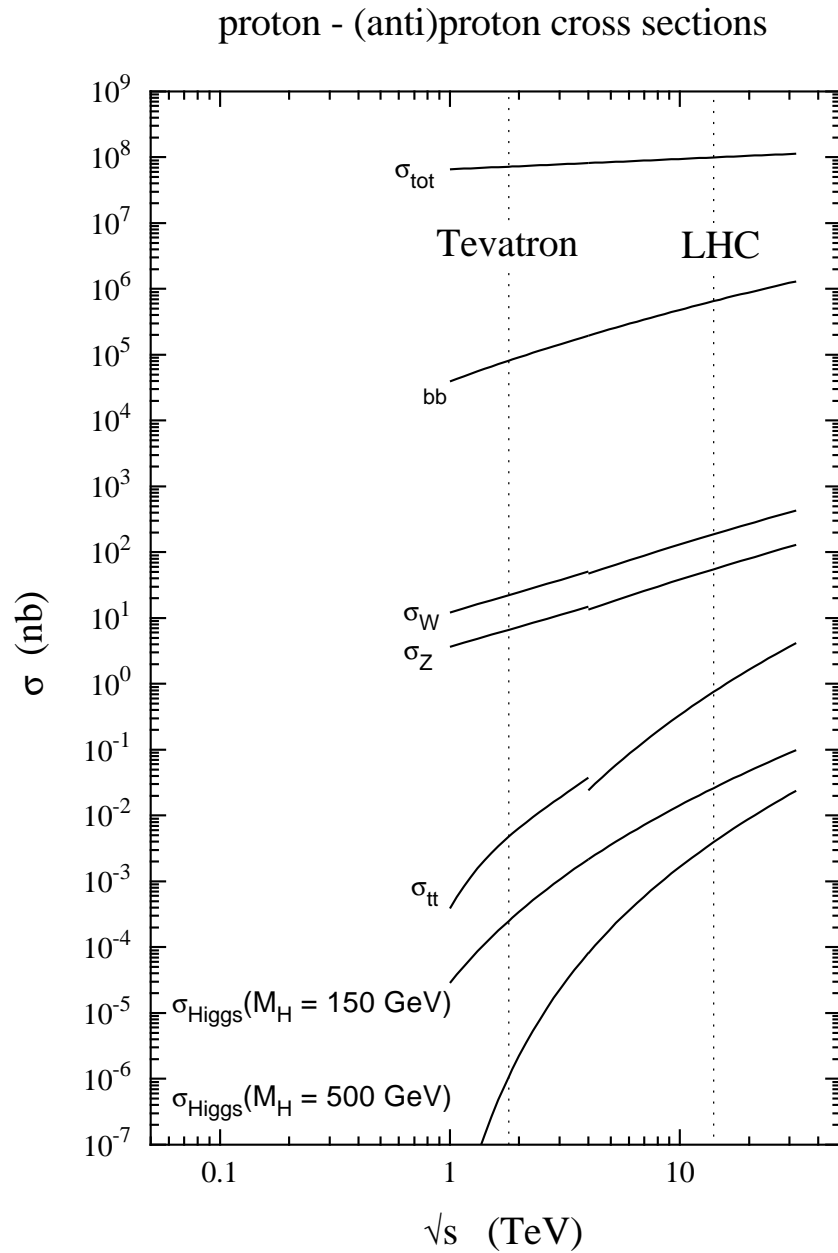


**Figure 2.9:** Cross sections as a function of the centre-of-mass energy in the hadron-hadron system for proton-(anti)proton collisions. At the LHC protons will be collided with protons at 14 TeV. For comparison the Tevatron values for proton-anti-proton collisions at 1.96 TeV are shown [17].

Event classification is therefore analogue to  $W^+W^-$  decay event classification. Table 2.3 shows the relative branching ratios of top pair decays and the used naming convention of the final states.

### Fully hadronic final states

In the largest fraction of top pair decays both W bosons decay hadronically. The decay can be written as

$$t\bar{t} \rightarrow b\bar{b}W^+W^- \rightarrow b\bar{b}q\bar{q}'q''\bar{q}'''.$$

This channel has the combined advantage of being the most probable decay mode with (at least in principle) completely measurable particles in the final state. The solely hadronic activity imposes large challenges, especially at a hadron collider. Effective selection will be a challenging task due to the large hadronic backgrounds. Reconstruction is complicated due to the large number of combinatorics in assigning the reconstructed quarks to the right decay, even if the selection and the jet reconstruction was successful. It remains to be seen if this channel allows a clean and efficient selection that will permit a cross section measurement. A proposal for the selection and a mass measurement in this decay channel at the LHC with the CMS detector exists [18].

### Semileptonic final states

The second largest fraction of final states originates from a combination of one hadronic and one leptonic W boson decay. These decays can be written as

$$t\bar{t} \rightarrow b\bar{b}W^+W^- \rightarrow b\bar{b}q\bar{q}'\ell\nu_\ell,$$

Name	Process	Branching Fraction
Fully hadronic	$t\bar{t} \rightarrow b\bar{b}W^+W^- \rightarrow b\bar{b}q\bar{q}'q''\bar{q}'''$	46.2%
Semileptonic	$t\bar{t} \rightarrow b\bar{b}W^+W^- \rightarrow b\bar{b}q\bar{q}'\ell\nu_\ell$	43.5%
Dileptonic	$t\bar{t} \rightarrow b\bar{b}W^+W^- \rightarrow b\bar{b}\ell\nu\ell'\nu'$	10.3%
Semileptonic'	$t\bar{t} \rightarrow b\bar{b}W^+W^- \rightarrow b\bar{b}q\bar{q}'\ell\nu_\ell (\ell \neq \tau)$	28.8%
Dileptonic'	$t\bar{t} \rightarrow b\bar{b}W^+W^- \rightarrow b\bar{b}\ell\nu\ell'\nu' (\ell \neq \tau)$	5.1%

**Table 2.3:** The nomenclature and the branching fraction of the different decay modes used in this thesis. Other names are also in use. For example semileptonic decays are also often called *lepton plus jets*.

where  $\ell$  denotes either an electron, muon or tau, and  $\nu_\ell$  the respective neutrino partner. The neutrino escapes undetected. The event is therefore not fully determined by detectable particles. Only by application of kinematic constraints full event reconstruction is possible. At hadron colliders tau final states are usually excluded from the analyses, because in the tau decay chain are always two neutrinos present. This makes full and accurate reconstruction more complicated than in the electron or muon semileptonic case. In the most probable case of hadronic tau decays no lepton is available, which makes event classification more complicated. The almost equal statistical importance with respect to the fully hadronic decays is reduced by one third due to this exclusion of final states. A single charged lepton makes event selection much easier than in fully hadronic decays. One of the two top quarks is still fully determined by detectable particles. In this analysis semileptonic  $t\bar{t}$  decays with either an electron or a muon in the final state are considered.

### Dileptonic final states

The remaining decay mode occurs when both W bosons decay leptonically, producing a pair of a oppositely charged leptons and two neutrinos. This can be written as

$$t\bar{t} \rightarrow b\bar{b}W^+W^- \rightarrow b\bar{b}\ell\nu\ell'\nu'.$$

Dileptonic decays are intrinsically underdetermined, due to the undetectable two neutrinos. The problem is more pronounced if one or both charged leptons are a tau, as described for the semileptonic decay mode. Good measurement of the leptons therefore demands again the rejection of taus in the final state. The branching ratio of events without taus amounts to approximately 5%. The major advantage of dileptonic final states is the easiest selection of  $t\bar{t}$  events, due to the clear signature of two oppositely charged leptons. Full event reconstruction is only possible based on assumptions about the event kinematics. The selection of these decays is both very pure and efficient in comparison to the other final states.

### 2.2.2 Cross section

At a hadron collider four different processes contribute to top quark pair production in leading order (LO). Figure 2.10 shows the three gluon fusion contributions, figure 2.11 shows the quark annihilation process.

The leading order hadronic cross section for top pair production can be written as

$$d\sigma_{\text{hadronic}} = \sum_{i,j} \int dx_1 dx_2 \text{pdf}_{i,H_1}(x_1, \mu_F) \text{pdf}_{j,H_2}(x_2, \mu_F) \cdot d\hat{\sigma}(i(x_1 P_1)j(x_2 P_2) \rightarrow t\bar{t}). \quad (2.7)$$

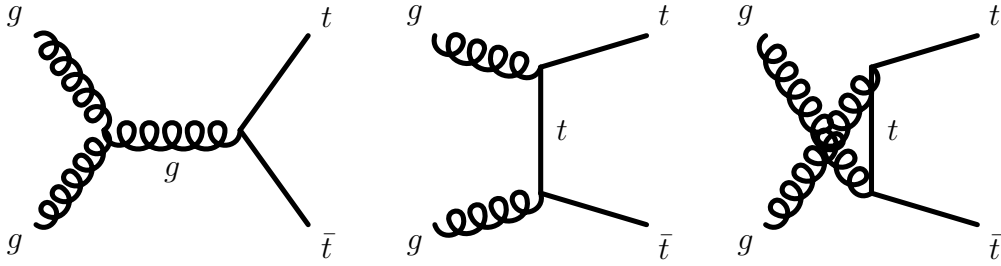


**Figure 2.10:** The three gluon fusion Feynman diagrams for top quark pair production in leading order.

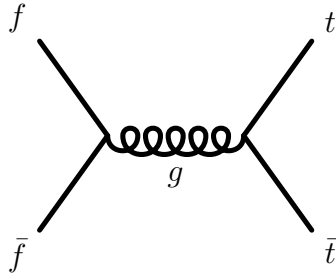


**Figure 2.11:** The quark annihilation Feynman diagram for top quark pair production in leading order.

Protons are the colliding particles, which are described by the parton distribution functions  $\text{pdf}_{i,H}(x, \mu_F)$ . They describe the probability to find a parton  $i$  (quark or gluon) in the hadron  $H$  with the momentum fraction  $x_i$  of the hadron momentum  $P_i$ . For calculation the partonic cross section can be divided into two contributions, gluon fusion and quark–anti-quark annihilation. The ingoing particles in the partonic process have momenta  $p_{1,2}$ , while the outgoing partons have  $p_{3,4}$

$$\begin{aligned} g(p_1) + g(p_2) &\rightarrow t(p_3) + \bar{t}(p_4) \\ q(p_1) + \bar{q}(p_2) &\rightarrow t(p_3) + \bar{t}(p_4) \end{aligned}$$

The cross section calculation follows the usual way of separating the kinematics and the matrix element calculation

$$d\hat{\sigma}_{ij} = \frac{1}{\hat{s}} \frac{d^3p_3}{(2\pi^2)^3 2E_3} \frac{d^3p_4}{(2\pi^2)^3 2E_4} (2\pi)^4 \delta^4(p_1 + p_2 - p_3 - p_4) \overline{\sum} |\mathcal{M}_{ij}|^2,$$

where the first part is the flux factor with the actual centre-of-mass energy  $\hat{s} = (p_1 + p_2)^2$ . The derivation of the matrix element is given in [19]. For the gluon fusion the colour and spin averaged result is

$$\overline{\sum} |\mathcal{M}_{gg}|^2 = (4\pi\alpha_2)^2 \left( \frac{1}{6\tau_1\tau_2} - \frac{3}{8} \right) \left( \tau_1^2 + \tau_2^2 + \rho + \frac{\rho^2}{4\tau_1\tau_2} \right)$$

And for the quark annihilation the averaged result is

$$\overline{\sum} |\mathcal{M}_{q\bar{q}}|^2 = (4\pi\alpha_2)^2 \frac{4}{9} \left( \tau_1^2 + \tau_2^2 + \frac{\rho}{2} \right)$$

Some kinematical shorthands for the ratios of scalar products are used to simplify the notation

$$\tau_1 = \frac{2(p_1 \cdot p_3)}{\hat{s}}, \quad \tau_2 = \frac{2(p_2 \cdot p_3)}{\hat{s}}, \quad \rho = \frac{4m^2}{\hat{s}}.$$

The total hadronic cross sections in equation (2.7) can be evaluated in terms of the ratio of the two production mechanisms. At the LHC with the collision of  $pp$  at 14 TeV the production is dominated by about 90% gluon fusion, leading to a total LO cross section of about 490 pb. For the Tevatron, colliding  $p\bar{p}$  at 1.96 TeV the production is dominated to about 85% by  $q\bar{q}$  annihilation resulting in a total leading order cross section of roughly 7 pb [3]. The predominance of gluon fusion can be explained by the domination of the gluon density at low  $x$  in the proton (see the example for a pdf in figure 2.8). Assuming symmetric momenta for the colliding partons the minimal needed energy for each parton is the top quark mass. With the given beam energy of the Large Hadron Collider of 7 TeV this amounts to

$$x_{min} = 2m_t/\sqrt{s} \approx 0.025.$$

It is evident from QCD that the leading order calculation is only the starting point. The further expansion in orders of  $\alpha_s \approx 0.1$  is needed, including interference effects. Especially the large phase space at the LHC for additional hard gluon radiation in  $t\bar{t}$  production makes it mandatory to incorporate higher orders. The current prediction for the total  $t\bar{t}$  production cross section (for a top mass of 171 GeV and a centre-of-mass energy  $\sqrt{s} = 14$  TeV) is [20]

$$\sigma_{t\bar{t}}^{\text{NLO+NLL}} = 908_{-85}^{+82}(\text{scales})_{-29}^{+30}(\text{PDFs})\text{pb}.$$

Higher-order calculations exist for the total cross section, single-inclusive  $p_T$  and  $y$  spectra and double differential spectra [21].



# Chapter 3

## The Experimental Setup

The Large Hadron Collider (LHC) is a proton–proton collider with a centre-of-mass energy of 14 TeV. The Compact Muon Solenoid (CMS) is one of the four experiments at the LHC, built to detect final state particles that are produced in the collisions. The other experiments at the LHC are ALICE (A Large Ion Collider Experiment), a dedicated heavy ion detector, ATLAS (A Toroidal LHC Apparatus), another general purpose detector besides CMS, and LHCb (Large Hadron Collider beauty), which is a specialised detector for the measurement of B-hadrons.

This chapter begins with a short description of the LHC. Then the CMS detector is presented. Emphasis is put on the parts necessary for the reconstruction of top quark decay products.

### 3.1 The Large Hadron Collider

The LHC is operated by the European Organization for Nuclear Research CERN (formerly Conseil Européen Pour La Recherche Nucléaire), situated in Geneva. The collider is a ring accelerator with a circumference of almost 27 km, located in a tunnel between 70 m and 140 m underground of Switzerland and France. The main operation mode of proton–proton collisions starts in 2009 and will later be expanded by an additional running period with heavy ions. Here only the proton configuration is described. In figure 3.1 the layout of the collider with the position of the experiments is sketched.

The nominal centre-of-mass energy in the proton–proton system is  $\sqrt{s} = 14$  TeV with symmetric beam energies. Before entering the LHC the protons are pre-accelerated in different systems. The final injection is done by the Super Proton Synchrotron at an energy of 450 GeV. Superconductive radio frequency cavities provide the electrical field

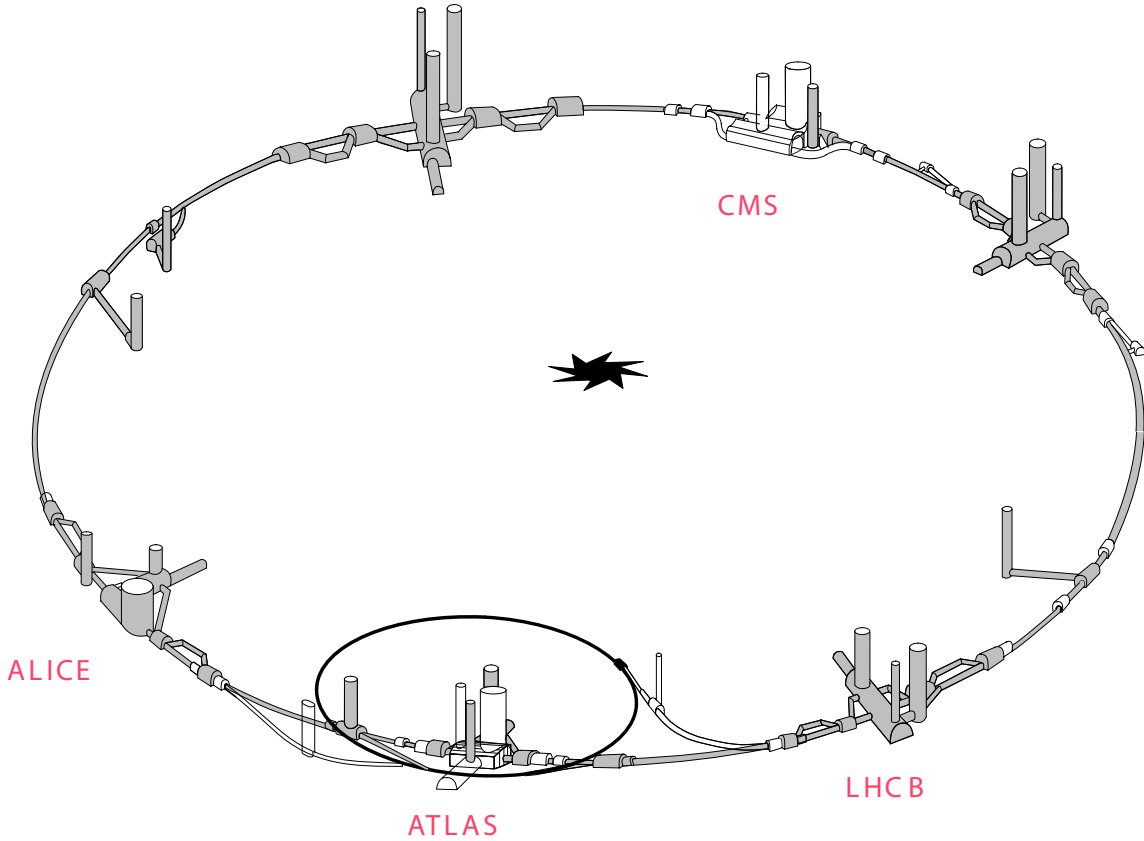


**Figure 3.1:** An overview sketch of the LHC and the position of the four experiments. The tunnel is located between 70 m and 140 m underground [22].

needed for the acceleration. The protons are kept on track by magnetic fields. Because of the same charge of the protons two separate beam lines are needed. A main component of the collider are 1232 superconductive dipole magnets with two beam pipes in the middle. The dipole field is configured in a way that the charged particles are kept on the curved track in both directions. By equating the Lorentz force and centripetal force the needed magnetic field strength  $B$  can be computed:

$$B = \frac{p}{q \cdot r_{LHC}}.$$

For a proton with charge  $q = +1$ , a momentum of 7 TeV and the exact radius of the LHC  $r_{LHC} = 2804\text{ m}$  this results in a field strength of  $B = 8.33\text{ T}$ . Several thousand additional magnets are needed for focusing and correcting the beams.

The integrated luminosity  $L$  of a collider relates the total cross section  $\sigma$  of a certain process and the number  $N$  of occurring events:

$$N = L \cdot \sigma. \quad (3.1)$$

The luminosity  $L$  in equation (3.1) is the integrated luminosity over time

$$L = \int dt \mathcal{L}.$$

The instantaneous luminosity  $\mathcal{L}$  can be expressed by the beam configuration of the collider

$$\mathcal{L} = f \frac{kn_1n_2}{4\pi\sigma_x\sigma_y}, \quad (3.2)$$

where  $n_i$  is the number of particles in each of the  $k$  bunches,  $\sigma_x$  and  $\sigma_y$  are the extension of the colliding bunch perpendicular to the beam direction and  $f$  is the revolution frequency. There are up to  $1.15 \cdot 10^{11}$  protons in each bunch, with a total of up to 2808 bunches in the collider. By the given size of the ring the revolution frequency is fixed to  $f = c/r_{LHC} = 11.25$  kHz. The actual bunch crossing rate is 40 MHz as a result of a complex bunch train structure.

Several luminosity phases are foreseen, which determine the actual beam parameters. In the initial phase the emphasis is put on the commissioning of the machine. The first main operation will be the *low luminosity phase* in the first years with an instantaneous luminosity of  $\mathcal{L} = 10^{33} \text{ cm}^{-2}\text{s}^{-1}$ . It is intended to collect an integrated luminosity of several  $10 \text{ fb}^{-1}$  in this phase. The *high luminosity phase* corresponds to a nominal design luminosity of  $\mathcal{L} = 10^{34} \text{ cm}^{-2}\text{s}^{-1}$ . This phase is intended to last more than five years, collecting several  $100 \text{ fb}^{-1}$ . Plans for further luminosity and energy upgrades are currently under review.

The LHC is unique in its combination of both the highest energy and the highest luminosity. The very high collision rate presents a great challenge for the experiments. One of the most prominent analysis challenges will be the occurrence of so-called Pile-Up events. Due to the total inelastic proton–proton cross section of about 120 mb at  $\sqrt{s} = 14$  TeV the average number of events per bunch crossing will be about 2.4 at the low luminosity, rising to 24 at high luminosity. The detector hardware design and the subsequent reconstruction are specifically designed to cope with the resulting challenges. The beams are brought to collision at a small horizontal crossing angle of  $284 \mu\text{rad}$  (at the CMS interaction point). This reduces the length of the interaction region along the beam-pipe in the  $z$  coordinate.

## 3.2 The Compact Muon Solenoid

CMS is designed as a multi-purpose detector to cover a broad range of physics expected at the LHC. It is built to measure and identify muons, electrons, photons and hadronic particles produced in the beam collisions with high accuracy. Figure 3.2 shows an overview of the detector.

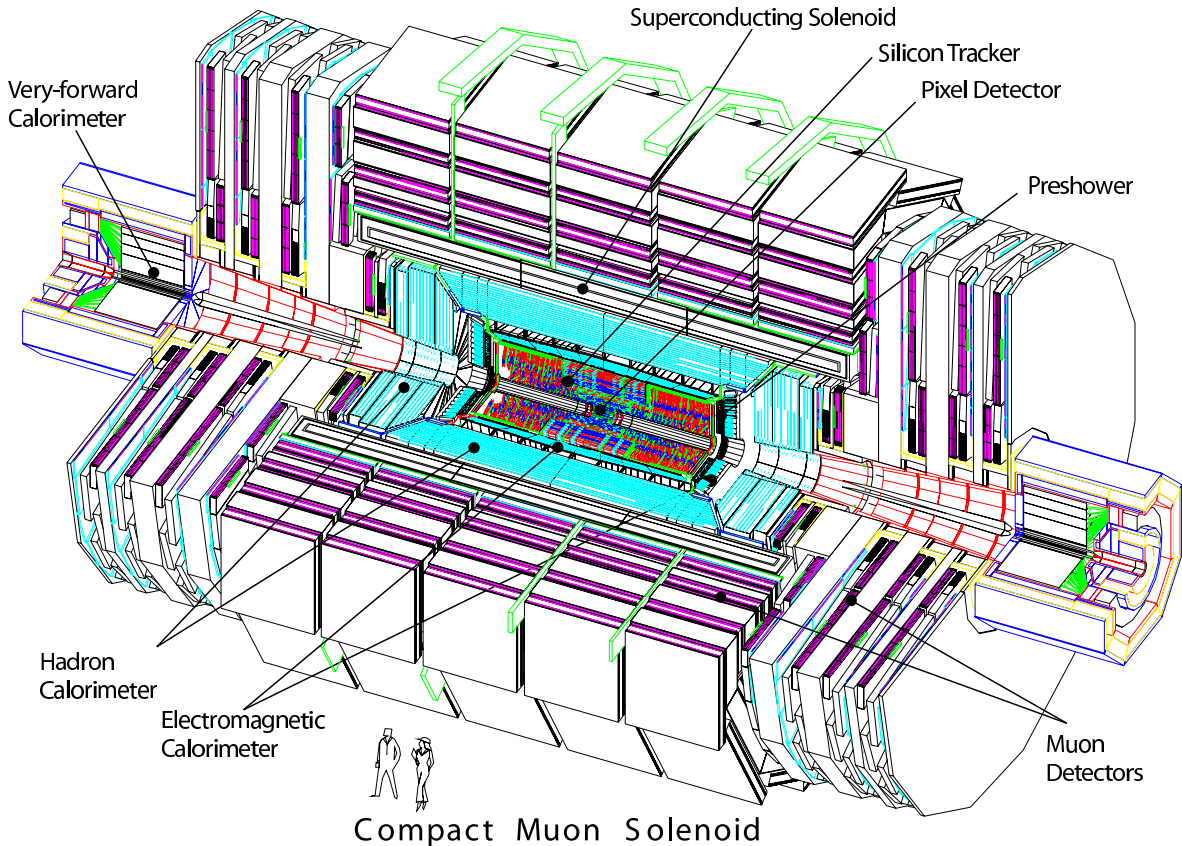


**Figure 3.2:** A perspective sketch of the CMS detector. The different subdetectors are denoted. The total length of the detector is 21.6 m, its central diameter is 14.6 m. The total weight is 12500 tons [23].

The detector has a cylindric shape and is built around the beam pipe with the nominal interaction point at the centre. The subdetectors are arranged in layers from inside out. Every subdetector is divided into a barrel and an endcap part.

Mechanically the detector is divided into eleven segments along the beam-pipe. The central segment contains a support tube that hosts the magnet and most parts of the inner detectors. Two wheels on each side of the central element cover the length of the

support tube and two endcap segments (in three parts) close the detector to the sides. This design allowed the pre-assembly in sections at ground level with subsequent lowering of each segment into the underground cavern. Further maintenance of the detector in the underground cavern is possible, since the detector can be opened by sliding the segments apart during shutdown phases.

The inner tracking system directly surrounds the beam-pipe and consists of the vertex detector and the tracker. Next the electromagnetic and the hadronic calorimeters are installed. The muon system is placed outermost within the iron return yoke of the magnet. A big steel tube mounted on the centre ring acts as support structure for the superconducting solenoid magnet. The tracking system and the calorimeters are embedded within the magnet. Extending its inner parts, two additional hadronic calorimeter endcaps are mounted outside the iron structure, increasing the angular acceptance.

The decay products of semileptonic top pair decays leave signatures in all sub-detector components. Any measurement of these kinds of decays therefore requires the input from all sub-detectors, making use of the whole detector.

### 3.2.1 CMS coordinate system

The origin of the CMS coordinate system is the nominal interaction point, located in the centre of the detector. The horizontal  $x$  axis is pointing south to the accelerator ring centre. The vertical  $y$  axis is pointing upward. To create a right-handed coordinate system, the horizontal  $z$  axis is pointing west, which also defines the two beam direction as positive and negative. The polar angle  $\vartheta$  is measured with respect to the  $z$  axis,  $\vartheta = 0$  is  $+z$  axis and  $\vartheta = \pi$  is  $-z$  axis. The azimuthal angle  $\phi$  is measured in the  $x/y$  plane,  $\phi = 0$  is  $+x$  axis and  $\phi = \pi/2$  is  $+y$  axis. By definition  $\phi$  varies between  $-\pi$  and  $+\pi$ .

The intrinsic ignorance of an unknown boost along the  $z$  axis at a hadron collider is reflected in some additional commonly used variables. A useful kinematic variable for hadron colliders is the pseudorapidity  $\eta$ . For massless particles it is the same as the rapidity  $y$ , which is Lorentz invariant under boosts along the beam axis. The pseudorapidity is related to the polar angle  $\vartheta$ :

$$\eta = -\ln \left( \tan \frac{\vartheta}{2} \right).$$

The sign of  $\eta$  is equal to the sign of  $z$ . An angular distance  $\Delta R$  can be defined as a combination of distances in  $\phi$  and  $\eta$

$$\Delta R = \sqrt{(\Delta\phi)^2 + (\Delta\eta)^2}.$$

The transverse energy  $E_T$  (or likewise momentum  $p_T$ ) is also boost invariant

$$E_T = E \cdot \sin \vartheta = \frac{E}{\cosh \eta}.$$

### 3.2.2 Solenoid

The solenoid provides the magnetic field needed for the bending of tracks, which allows the determination of particle momenta in the tracker. The chosen configuration by CMS is a large superconducting solenoid with a field of approximately 4 T. All calorimeters and inner tracker parts are located inside the magnet and provided with the nominal magnetic field. Embedded in the iron return yoke is the muon chamber system, which is thus provided with a magnetic field of 2 T of reversed polarity with respect to the field inside the solenoid [24].

### 3.2.3 Tracking System

The tracking system is the core part of the detector. Its purpose is to measure the momentum of charged final state particles as precisely as possible. A particle can be identified by its momentum, charge and energy. Momentum and the sign of the charge are measured within the tracker that is embedded in the solenoidal magnetic field. The tracks are bent in the  $r\phi$ -plane by the Lorentz force

$$\vec{F}_L = \frac{q}{m} \vec{p} \times \vec{B}.$$

Because the solenoidal field is parallel to the beam direction only the transverse momentum part is measured. The tracker provides the hits for measuring the track curvature. The relative accuracy of the transverse momentum measurement can be approximated by

$$\frac{\delta p_T}{p_T} = \frac{1}{qBl^2} p_T \frac{\sqrt{720}}{\sqrt{N+4}} \sigma_x,$$

where  $q$  is the charge of the particle,  $B$  is the magnetic field,  $l$  is the length of the measured track segment,  $N$  is the number of hits and  $\sigma_x$  the single hit resolution [25].

To optimise the resolution one therefore has to choose a high magnetic field, try to get a long lever arm on the track (a large  $l$ ), minimise the single hit resolution and try to get as many hits as possible.

For the analysis of semileptonic  $t\bar{t}$  pair decays tracks play a very important role. Good identification and reconstruction of leptons is crucial for the selection and reconstruction

of the leptonically decaying  $W$  boson in the semileptonic decay mode. The measurement of the charged fraction of the hadrons can enhance the reconstruction of jets. If the ratio of charged and neutral particles in a jet can be determined, the much better momentum resolution of the tracker can enhance the overall jet energy measurement. Furthermore the inner tracker is used in the identification of special hadron flavors like B-hadrons, which helps to suppress background processes in the selection of  $t\bar{t}$  events.

The tracking system consists of three parts. For the two innermost parts silicon has been chosen as the sensitive material. The innermost detector is built of silicon pixel detectors and is extended outwards by a silicon strip tracker. Silicon detectors combine the advantage of high spatial hit resolution in combination with a very fast readout, which is needed due to the high bunch crossing rate of 40 MHz. The third and outermost part outside the magnet coil is the muon system, which is built of three different types of gaseous detectors.

### The Vertex Detector

The vertex detector (figure 3.3) provides exact measurement of the starting point of any charged track. This is needed for an exact reconstruction of vertices and tracks. The key resulting ability is to distinguish the primary vertex from secondary or higher-order vertices. The main purpose is particle identification of heavy decays from charm or bottom quarks, but it is also important for the suppression of Pile-Up events. These Pile-Up events do not originate from the hard proton–proton collision and therefore have often a different  $z$  value of their vertex.

The measurement of vertex properties is the main ingredient for the identification of heavy quark decays, with special emphasis on bottom quarks. The big importance especially for  $t\bar{t}$  decays is the large branching ratio of top quarks into bottom quarks, which is very close to unity ( $\approx 0.998$ ). Due to hadronisation b-quarks immediately (in about  $10^{-24}$ s) form b-hadrons, which may live long enough to travel macroscopic distances in the order of millimeters from their production vertex. Thus their final decays have a different vertex position. In addition the track multiplicity is higher than in non b-hadron decays. Both properties can be measured with a highly granular vertex detector with high spatial resolution. The possibility to identify jets originating from b-quarks can be used as an important part in selection of top quark decays.

In the pixel detector silicon pixels of the size  $100\ \mu\text{m} \times 150\ \mu\text{m}$  in  $r\phi \times z$  are used as active material. The thickness of the sensitive silicon is about  $300\ \mu\text{m}$ , directly interfacing a readout chip. The silicon pixels are put into an array of different geometries according to the barrel and endcap design. The complete sensor modules are grouped together and put on a carbon fibre support structure to form the geometry of the barrel and endcap.

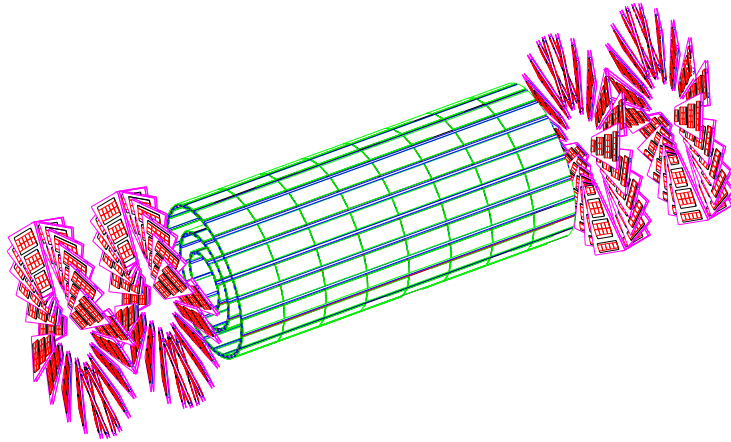


**Figure 3.3:** Schematic perspective sketch of the pixel detector. The beam pipe is almost directly embraced by the inner layer of the barrel. The inner diameter of the first barrel layer is about 8.2 cm, the outer diameter of the last barrel layer is about 21 cm. The length of the barrel is about 53 cm. At  $z = \pm 35.5$  cm and  $z = \pm 46.5$  cm the endcap disks are located [23].

The barrel part consists of three layers of modules (so called *ladders*). The endcaps are constructed of two layers (planned with an upgrade to three layers later) of turbine shaped disks. Each pair of endcap disks has 9 million readout channels. The barrel layers have 9.6, 16 and 22.4 million readout channels respectively. In total there are 66 million readout channels.

The resulting angular coverage in rapidity is  $|\eta| \leq 2.4$  for a track originating from the centre of the detector. The spatial precision is around  $10 \mu\text{m}$  in  $r\phi$  and  $15 \mu\text{m}$  in  $z$  for at least two hits in different layers. It is achieved through charge spread across more than one pixel [26].

### The Silicon Strip Tracker

The maximum number of hits for the vertex detector is limited to three. To increase this number with longer leverage the tracking system is extended by a larger structure. The expected density of hits will be much lower due to the larger distance to the interaction point, so a less granular detector technique than in the vertex detector is feasible. Silicon strip sensors in a highly modular construction are chosen. The inner tracker layout is shown in figure 3.4.

In its structure the tracker is divided into an inner part with the Tracker Inner Barrel (TIB) and Tracker Inner Disks (TID) as endcaps. This inner part is enclosed by the

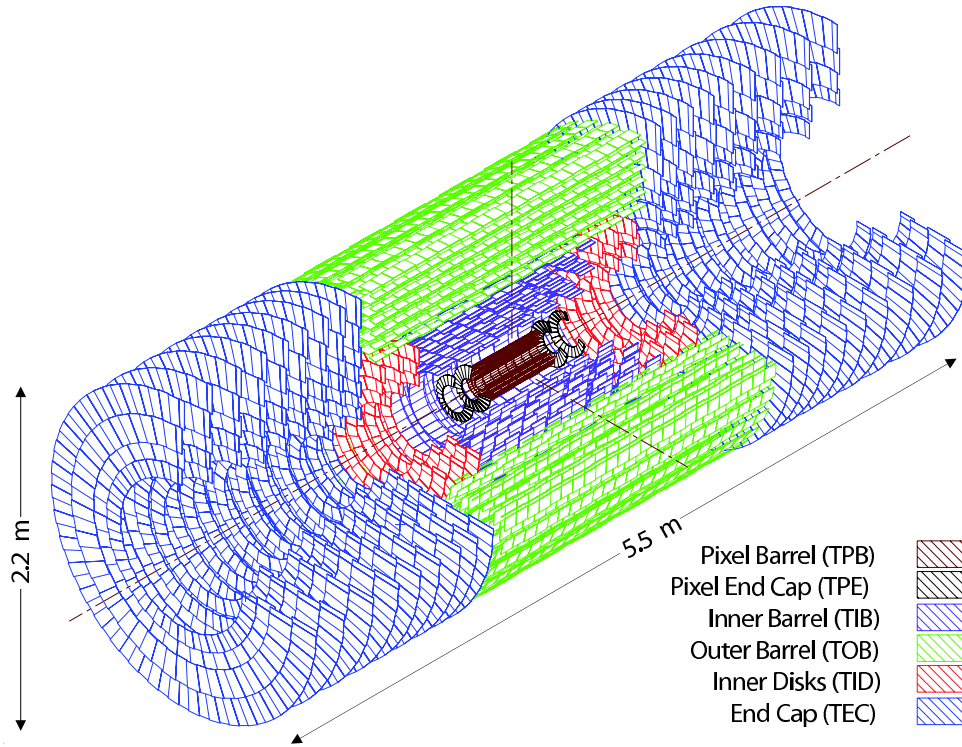


**Figure 3.4:** A perspective sketch of the silicon strip tracker and its components. The overall length is almost 5.6 m, the outer diameter is roughly 2.2 m. In the centre the vertex detector is visible [27].

Tracker Outer Barrel (TOB). The TOB is then closed to the sides with the Tracker Endcaps (TEC). The silicon strip modules in rectangular or trapezoidal shape are mounted onto the support structure so that the area of each layer is completely covered by sensitive material. Each sensor has about  $10 \text{ cm} \times 10 \text{ cm}$  size with separated readout strips of  $80 \mu\text{m}$  to  $210 \mu\text{m}$  width. In the barrel there are ten layers in total, four layers in the TIB and six in the TOB. The endcaps are made of 12 layers, the TID consists of three disks and the TEC of nine disks on either side. The inner diameter of the endcaps increases from the central disks to the outer ones in order to minimise the excess material. Charged particle rapidities up to about  $|\eta| \approx 2.5$  can therefore be registered by a sufficient number of active layers. The spatial single point resolution of  $100 \mu\text{m}$  is similar to the width of the strips [26, 28].

Combining the vertex and the strip detector information the resulting transverse momentum resolution for single high  $p_T$  tracks can be parametrised as [26]

$$\frac{\sigma p_T}{p_T} \simeq (15 \cdot p_T [\text{TeV}] \oplus 0.5)\% \quad (|\eta| \leq 1.6).$$

## The Muon System

Muons are a substantial part of semileptonically decaying  $t\bar{t}$  pairs. The muon system enables a very good identification and reconstruction of these muons in the signal process.

Figure 3.5 shows a cross section in the  $yz$ -plane of a detector quadrant.

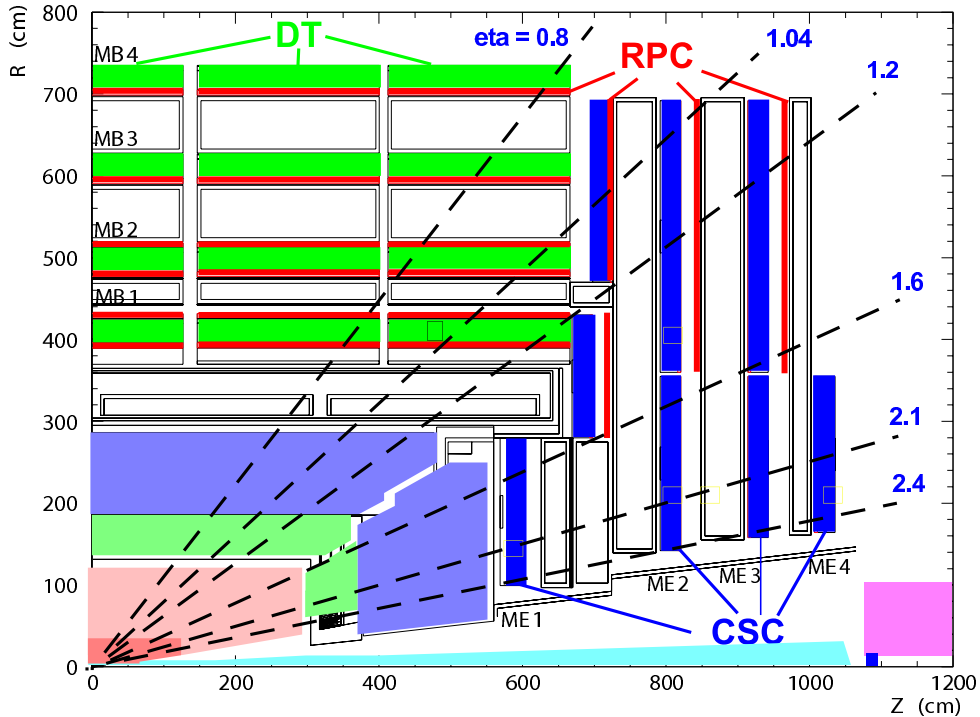


**Figure 3.5:** Cross section view in the  $yz$ -plane of a quadrant of the muon system. Shown is the position of the three different chamber designs: drift tubes (DT), cathode strip chambers (CSC) and resistive plate chambers (RPC) [23].

The muon system is the outermost part of the tracking system, intended to measure only muons. Because muons are minimal ionising particles, they can pass relatively undisturbed through the detector. Therefore the system is placed outside the calorimeters and the magnet coil.

The muon system employs three different gaseous detector technologies. Drift tubes (DT) are used in the barrel part, cathode strip chambers (CSC) in the endcap region and resistive plate chambers (RPC) in both regions. The magnetic field for bending of the tracks is provided by the installation into the iron support structure that acts as return yoke to the magnet. The measurement principle varies with the different detector types.

A cross section view of a drift cell used in the drift tubes is shown in figure 3.6. An anode wire is held inside a long rectangular chamber filled with gas, the walls acting as cathode. If a particle crosses the active volume of the gas electron and ion pairs are created. These pairs drift and finally create a charge avalanche in the strong electric field close to the wire surface. This amplified signal is registered by the readout system. The time between the traversing of the particle and the signal creation due to the charge-collection on the electrodes is approximately proportional to the perpendicular distance between the particle path and the wire. This results in a good measurement of one coordinate, the perpendicular distance to the wire. The other two coordinates are determined more coarsely by the length of the chamber and its lateral position in the detector. The drift tube chamber is usually made of three Super Layers of four staggered layers of rectangular drift cells. The wires in the first and the third layer of the Super Layers are parallel to the beam line, thus measuring in the track bending plane. The layer in between is perpendicular to that. In total there are 250 drift tube chambers in four layers.

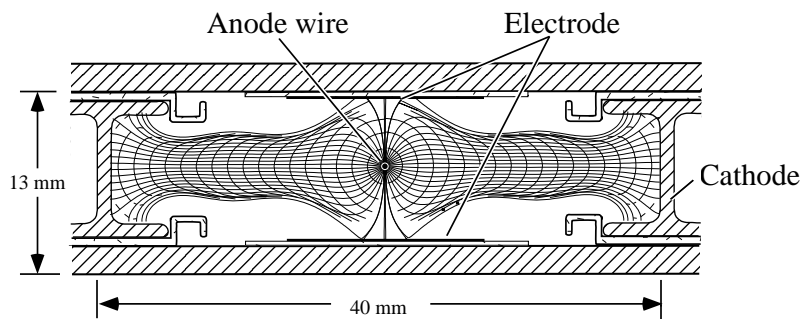


**Figure 3.6:** The drift tube cell design with the central anode wire. Denoted are the electrical field lines including the lines of constant drift times [29].

The cathode strip chambers are designed as multi wire proportional chambers in which one of the cathode plates is segmented in strips perpendicular to the wires. As a result of the segmentation the charge collection on the cathode is distributed over several strips. Spatial resolution is enhanced, since the position is interpolated with respect to the charge distribution. The close spacing of 3.12 mm between the anode wires makes the readout very fast, since the drift times are small. A sketch of the measurement principle is shown in figure 3.7. The combination of wire and cathode signals results in a precise measurement of two coordinates. Each chamber consists of six layers of gas volume, anode wires and cathode strips. The CSCs are only used in the endcaps, therefore a chamber is trapezoidal in shape, covering a complete segment of a circle. The chambers are arranged in four layers in each endcap, with two chambers overlapping in  $\phi$  to avoid gaps. In total 468 cathode strip chambers are installed.

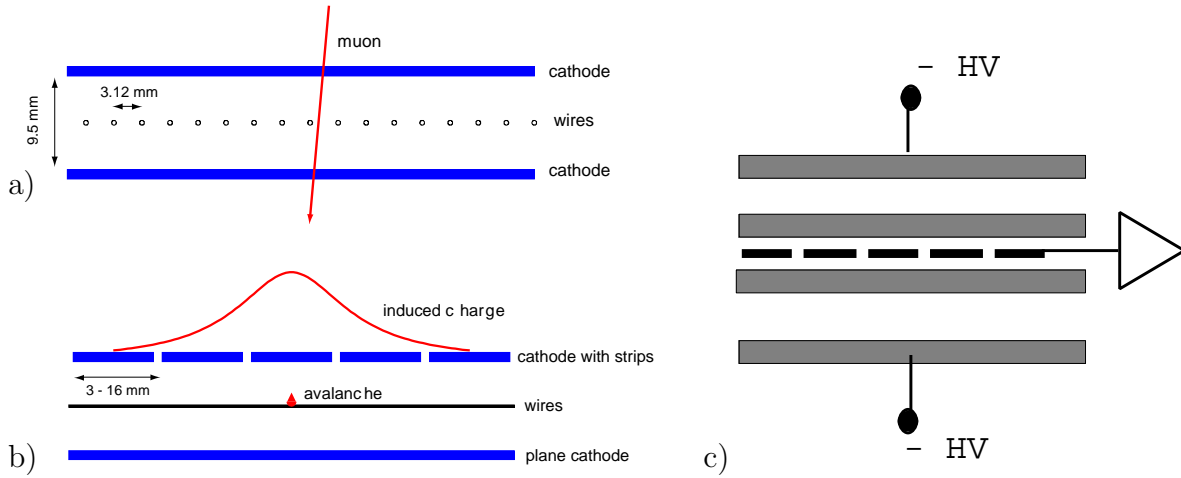


**Figure 3.7:** The cathode strip chamber design. a) A traversing muon is registered by the wire readout. b) Spatial reconstruction accuracy in the perpendicular plane is provided by the strip readout below. c) The resistive plate chamber design of the double gap type (with a single readout). The electric field is induced by applying the high voltage (HV) on the electrodes [29].

The third type of muon detectors is the resistive plate chamber. In principle a RPC is a gas volume between two resistors inside a large electric field. The schematic layout is shown in figure 3.6c). A muon passing through the gas volume will create a charge avalanche that can be recorded. This type of chamber is primarily used for triggering. It creates a very fast signal, but has rather low granularity. The actual design of a RPC is the double-gap type, which means that two sensitive volumes are staggered. Bakelite as resistive material is separated with spacers by 2 mm. Graphite coating on the outer side is used as electrode for the high voltage. The readout is done with capacitive coupled strips between the two volumes of a chamber. The two innermost Super Layers of drift tube chambers are equipped with RPCs (with the strips running parallel to the beam). RPCs are also installed in the endcaps, though in the low luminosity phase only in the outer ring parts covering  $|\eta| < 1.6$  [29].

The angular coverage of the muon system is  $|\eta| < 2.4$ , with the barrel part covering  $|\eta| < 1.2$ . The resulting momentum resolution for muons with the combination of all tracker elements can be parametrised as [23]

$$\frac{\sigma_{p_T}}{p_T} = 0.045 \cdot \sqrt{p_T [\text{TeV}]}.$$

### 3.2.4 Calorimeters

Calorimeters are designed to measure particle energy by full absorption. Neutral particles are not measured by the tracking system. Hence the calorimeters are the only place to measure them. The combination of tracking and calorimetry gives the possibility to measure all particles (with the exception of neutrinos). A granular design of the calorimeters additionally gives a spatial resolution of the deposited energy. This allows geometrical matching with the tracking system.

CMS is equipped with two kinds of calorimeters. The electromagnetic and the hadronic calorimeter are both crucial for identification and reconstruction of decay products of semileptonic  $t\bar{t}$  decays. The electromagnetic calorimeter provides information that is crucial for the identification of electrons. Moreover the measurement of the final products of hadronisation is done by the combination of the hadronic and the electromagnetic calorimeter. This provides necessary input to the reconstruction of quarks (in the form of jets) originating from the  $t\bar{t}$  decays.

#### The Electromagnetic Calorimeter

The main purpose of the Electromagnetic Calorimeter (Ecal) is the measurement of photons and electrons over a broad energy range. It is composed of lead tungstate crystals ( $\text{PbWO}_4$ ) that precisely measure the energy by fully stopping electrons and/or photons. The high granularity additionally yields good spatial resolution. The separation into a barrel (EB) and an endcap (EE) part is also given here. The structure is modular. Several crystals are grouped together as submodules which themselves are mounted together as modules. These either form supermodules in the barrel or the endcaps. An additional element in front of the endcap is the preshower device (ES). Figure 3.8 shows a perspective sketch of the Ecal that hermetically encloses the tracking system.

High energetic electrons and photons create electromagnetic showers in material. These showers are the constant emission of Bremsstrahlung-photons and the successive conversion of photons into  $e^+e^-$ -pairs. Lead tungstate has a very short radiation length of  $X_0 = 0.89$  cm and a small Moliere radius of  $M_R = 2.19$  cm. Another major advantage of the material is the very fast response as scintillator. The length of the crystals varies between 230 mm in the barrel and 220 mm in the endcap, corresponding to radiation lengths of  $25.8 X_0$  and  $24.7 X_0$ . The crystals are shaped like pyramid stumps, varying in size of the smaller end from  $2.2$  cm  $\times$   $2.2$  cm in the barrel to  $2.86$  cm  $\times$   $2.86$  cm in the endcap. Avalanche Photodiodes are mounted on the outer end to collect the scintillation light and make up the first element in the readout chain. The crystal cross section corresponds to a division in  $\Delta\eta \times \Delta\Phi = 0.0175 \times 0.0175$  for the barrel. In the endcaps the granularity

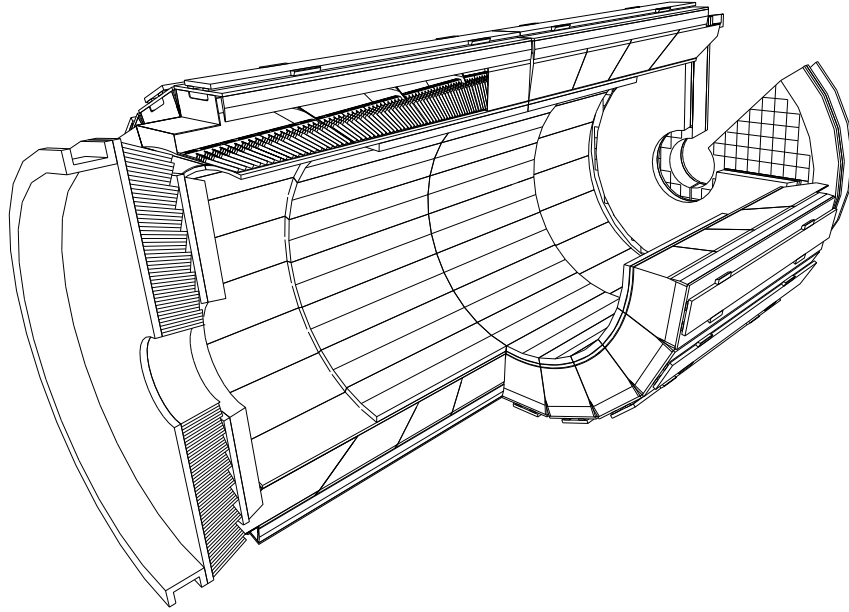


**Figure 3.8:** A schematic sketch of the Ecal. The tracking system is fully enclosed by the Ecal. The inner diameter is 124 cm, the outer diameter is 175 cm. The endcaps extend from  $z = \pm 317$  cm to  $z = \pm 390$  cm. The positioning of individual crystals can be seen at the cut edge of the front endcap and the upper part of the barrel [30].

progressively increases to  $\Delta\eta \times \Delta\Phi = 0.05 \times 0.05$  similar to the hadronic calorimeter. The crystals are mounted on the support structure a little off-pointing to the geometrical centre of the detector with a tilt of  $3^\circ$ . This enhances the directional resolution by a slight spread of showers into adjacent crystals. In total there are 61200 crystals in the barrel and 7324 in each of the endcaps. The barrel covers the pseudorapidity range of  $|\eta| \leq 1.479$ , the endcap directly extends the angular reach to about  $|\eta| = 2.5$ .

Most of the surface in front of the endcaps between Ecal and Tracker is covered by a preshower device. It consists of two planes of silicon strip detectors behind disks of lead absorbers with a radiation length of  $2X_0$  and  $3X_0$ . It helps to distinguish electrons and photons from objects that can fake a similar signature by forcing the showering process. The occurrence of the fake electrons and photons is more likely to happen in the forward (and backward) direction, so only this angular region is covered.

The lateral shape of the electromagnetic shower profile alone provides a possibility to identify electromagnetic objects. Its full potential of identification is utilised when the information is combined with the tracker and the hadron calorimeter.

The energy resolution of the Ecal can be parametrised as a function of the electron/photon energy, determined from test beam results and simulation [23]

$$\frac{\sigma E}{E} = \frac{(2.8 \pm 0.3)\%}{\sqrt{E[\text{GeV}]}} \oplus \frac{0.124 \text{ GeV}}{E} \oplus 0.3\%.$$

### The Hadronic Calorimeter

The Hadronic Calorimeter (Hcal) is a sampling calorimeter with copper alloy as the absorber material and plastic scintillator tiles as sensitive material. The usual structure of barrel (HB) and endcap (HE) that both rest within the magnet is extended with the Hadron Forward Calorimeter (HF). The HF rests outside the main detector endcaps. In the barrel outside the magnet a layer of scintillator fibres employs the magnet as absorber, making up the Outer Hadron Calorimeter (HO). Figure 3.9 shows a quadrant of the detector in cross section view in the  $yz$ -plane.

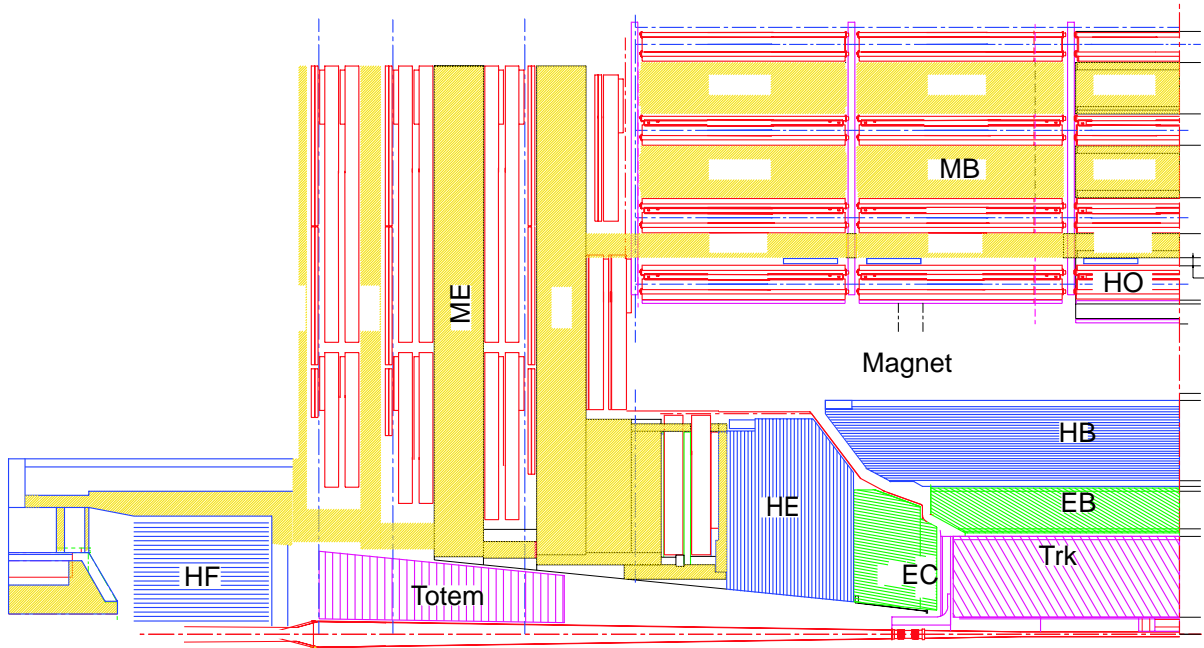


**Figure 3.9:** A cross section of the first quadrant of the detector in the  $rz$  plane. The HO is directly installed on the support tube outside the magnet. The inner diameter of the barrel (HB) is 1.81 m, the outer one 2.95 m. The endcap (HE) extends from  $z = \pm 317$  cm to  $z = \pm 390$  cm. The front of the forward part (HF) is at  $z = \pm 1120$  cm and extends to  $z = \pm 1285$  cm [23].

Alternating layers of copper alloy and plastic scintillator tiles are ordered in projective towers to the nominal interaction point. The Hcal is segmented in  $\eta$ ,  $\phi$  and in depth, which varies in dependence of  $\eta$ . The thickness in interaction lengths varies between  $7\lambda_I$  and  $11\lambda_I$ . The barrel is divided in two half barrels, one for each half space in  $z$ . Each half barrel is segmented into 18 wedges in  $\phi$ . Each wedge consists of four towers in  $\phi$  and 16 in  $\eta$ . The resulting front face division for the barrel are 2304 towers of  $\Delta\eta \times \Delta\phi = 0.087 \times 0.087$ . The angular coverage of the barrel is therefore  $\eta < |1.4|$ . Lateral segmentation varies between 17 and 19 layers of absorber/scintillator tiles. The principle of division in the endcaps is similar, but the actual values vary over the  $\eta$  position. The  $\eta$  towers up to  $|\eta| = 1.74$  are again  $\Delta\eta \times \Delta\phi = 0.087 \times 0.087$ . Up to the end of the endcap at  $|\eta| = 3.0$  this rises to  $\Delta\eta \times \Delta\phi = 0.35 \times 0.175$ . The lateral segmentation is usually 18 layers. The readout is done with wavelength shifting fibres that collect the scintillation light and transmit it to the readout with Hybrid Photodiodes. To cover even higher pseudorapidities up to  $|\eta| = 5.0$ , the Hadron Forward Calorimeter is installed, starting from  $|\eta| = 2.9$  (and thus creating a little overlap with the HE). Since no tracker coverage exists for this high  $\eta$  values a different technology is used. Emphasis is put on the measurement of the neutral part of hadron showers, which leads to a more compact design. The sensitive material are quartz fibres that emit Cerenkov light when struck by high energetic particles. The fibres are also used in signal readout, they transmit the yielded light to photomultipliers. Structurally the HF is roughly segmented in  $\Delta\eta \times \Delta\phi = 0.175 \times 0.35$  with two layers in depth [31].

The energy resolution of the Hcal as a whole depends on  $\eta$  as well as the energy itself due to the different structures and detector types. For the central part and an energy range between 30 GeV and 1 TeV it can be parametrised as

$$\frac{\sigma E}{E} = \frac{100\%}{\sqrt{E[\text{GeV}]}} \oplus 4.5\%.$$

### 3.2.5 Luminosity Monitoring

The master formula for luminosity relates the rate  $R$  of a given process with its cross section  $\sigma$ :

$$\mathcal{L} = \frac{R}{\sigma}.$$

The measurement of luminosity has two different purposes. It provides a real time monitoring accurate enough for online purposes (running the detector) and ultimately the important normalisation for physics analysis. The measurement of the collider related quantities in equation (3.2) does not yield sufficient accuracy. Since the actual value is

of high importance, an additional measurement is performed by the experiment, thus automatically including all down times.

Different ideas will be applied for real time monitoring and offline normalisation (used for physics analysis). The basic idea for both is to take an inclusive or exclusive process with a very precisely known total cross section  $\sigma$  and count the number of occurrences. Candidates for these processes are the total inelastic  $pp$  cross section and the production rates of  $W$  and  $Z$  bosons.

### Online Luminosity Monitoring

The mean number  $\mu$  of total interactions (inelastic proton–proton collisions) per bunch can be calculated for a bunch crossing rate  $f_{BX}$  by

$$\mu = \frac{\sigma \mathcal{L}}{f_{BX}}. \quad (3.3)$$

For the low luminosity at  $\mathcal{L} = 10^{33} \text{ cm}^{-2}\text{s}^{-1}$  this results in a mean of 2.4 interactions per bunch crossing. Based on information from the hadron forward calorimeter HF there are techniques foreseen for a real-time extraction of the luminosity. *Zero counting* is applicable for the low luminosity phase. It is based on Poissonian statistics that govern the number of interactions per bunch. For a mean value  $\mu$  the probability for a number of interactions  $n$  is

$$p(n; \mu) = \mu^n \frac{e^{-\mu}}{n!}. \quad (3.4)$$

The probability to have a given number of interactions in one bunch crossing depends only on the mean value. Even though the actual number is hard to determine, it is possible to distinguish between zero and one or more interactions. This is because any interaction is likely to deposit energy into the HF above the energy threshold. Inverting equation (3.4) yields the means to relate the number of bunch crossings with no interaction to the mean value

$$\mu = -\ln p(0).$$

With a large enough number of bunch crossings a good approximation of the probability is possible. The technique fails to work at high luminosity, for which equation (3.3) yields a mean of 24 interactions. This reduces the probability for bunch crossing with no interactions to a too low level. In addition the energy thresholds have to be raised, further tainting the significance. Other techniques are described in [23].

## Offline Luminosity Monitoring

The offline determination of the luminosity can be done in several ways. One measurement is provided by the TOTEM experiment [32].

A complementary determination is possible by using the production rates of  $W$  and  $Z$  as standard candles. Currently the theoretical uncertainty is larger than the needed accuracy, dominated by the uncertainty on the parton density functions. After its startup the data from LHC will provide the necessary input to obtain the needed accuracy [23].

### 3.2.6 Trigger and Data Acquisition

One of the fundamental challenges of an experiment at the LHC is the extremely high rate of hard interactions. The bunch crossing rate of up to 40 MHz in combination with up to 24 interactions per bunch crossing at high luminosity (see equation 3.3) leads to a rate of more than  $10^8$  events per second. This is opposed to the maximal rate of about 100 Hz with which events can be written to permanent storage. This results in the need of a rejection factor of the order of  $10^6$ . But also the actual rate of interesting events is much lower than the total rate. In the low luminosity phase about one  $t\bar{t}$  pair is produced per second, resulting in about one semileptonic  $t\bar{t}$  decay in three seconds. As a consequence a system must exist that selects events of interest with both high efficiency and high speed. The triggering system is designed to accommodate different and changing requirements for a wide range of physics including top quark pair decays. The trigger and the data acquisition (DAQ) system are closely related, due to the strict requirements on processing time and the massive amount of data.

The actual rate and data reduction takes place in two subsequent steps. The first step is done by the Level-1 trigger, built from very fast custom electronics. The final reduction is performed by the High-Level Trigger (HLT), implemented as software running on a large filter farm of hundreds of computers. Upon a positive total trigger decision the event is committed to permanent storage. In the following a more detailed description of the components is given.

#### The Level-1 Trigger

The Level-1 Trigger is built upon coarsely segmented data that need a minimum of processing for the fastest possible decision. In order to achieve this the Level-1 Trigger logic is built of programmable electronics located physically close to the detector. Segments of the trigger data are first built independently within the calorimetry system and the

muon system and then combined. To facilitate the decision the computed information is ranked in momentum or energy. As further information a level of confidence is incorporated in these measurements, both for the further chain of decision and quality control. Ultimately a Global Level-1 Trigger decision is made. To guarantee minimal dead time the full raw data of the subdetectors is buffered in pipelined memories for up to  $3.2\ \mu\text{s}$ . As resulting constraint the Level-1 Trigger decision must be made within  $1\ \mu\text{s}$ , due to the time it takes for the signals to be fully processed before and after decision-making. The maximal design Level-1 Trigger output rate is 100 kHz, limited by the average time to transfer the full detector information through the further readout system. The actual rate is limited to about 30 kHz to include a safety factor because of the uncertainties of beam and detector conditions [33].

### The High-Level Trigger

To achieve the final acceptable data rate of 100 Hz a further reduction in the order of  $10^3$  is needed. Ultimately this is achieved by the High-Level Trigger (HLT), which is embedded in the Event Filter system. A positive Level-1 Trigger decision sets the first step of data acquisition in action. The full raw detector information is read out and the huge amount of precision data is reduced by signal processing like zero-suppression and data compression. By this the event gets reduced to its final size of about 1.5 MB. Under control of the Event Manager the data is placed temporarily into memory units accessible to the Event Builder network. The bits of information from each subdetector for one event are not coherent at this stage, but distributed in different memory units. For online reconstruction the event must be reassembled. This is done by the Event Builder, which combines the event fragments in two steps. As a by-product the signals are transferred from underground to surface level. A schematic layout of the complex system architecture is shown in figure 3.10.

Regarding the further data flow the most important instance is the Event Filter complex with a number of different tasks. Besides collecting the data from the Event Builder network and performing basic consistency checks one of its main purposes is to run the HLT. The operation of the HLT is done in a very flexible way by running it as software on a processor farm. Each farm node runs the same code and the needed rate reduction can be achieved by scaling the number of nodes according to the time needed to make the HLT decision. Current expectation is that in the order of  $10^3$  processors will be needed. A central design idea is to reject an event as fast as possible and reconstruct only the needed parts in successive steps. This introduces the concept of *virtual trigger levels* consisting of the partial online reconstruction of an event. The final accept is given on the fully online-reconstructed event with specific information about the trigger decision. Upon a positive

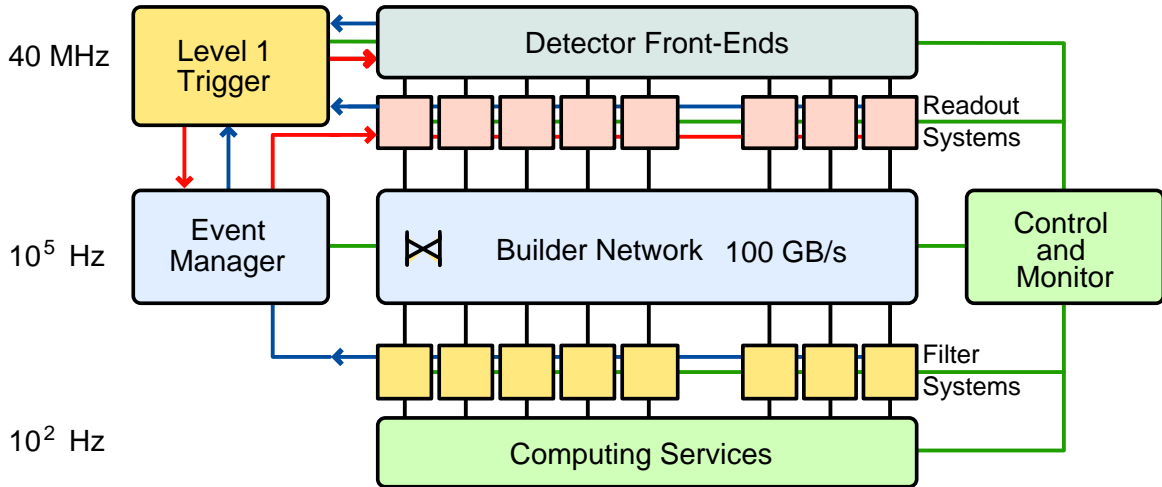


**Figure 3.10:** A sketch of the architecture of the trigger and data acquisition system. On the left hand side the approximate event rate is indicated. The logical data flow is from top to bottom. The Level-1 Trigger decision is based on raw data and triggers the Event Manager. The Event Manager controls the readout of the raw data and initiates first signal processing and data transfer into the Builder Network. Within the Builder Network an event gets reassembled and upon completion presented to the Event Filter system. The whole system is controlled and monitored on different levels.

HLT decision the Event Filter commits all data (including the trigger information) to permanent storage. Furthermore the Event Filter collects data and creates data streams for online Data Quality Monitoring. The accepted events are also routed into online streams for further relay within the CMS computing framework [34].

The triggers will reconstruct physics objects that closely resemble offline analysis objects. Examples are particle candidates like muons, electrons, photons, jets (see chapter 4) and inclusive quantities like the scalar sum of transverse energy. It is not expected that a specific top trigger will exist, but rather a logic combination of triggers will resemble such a trigger. Especially for the semileptonic decay channel the single lepton triggers for muons and electrons are important.

# Chapter 4

## Event Generation, Simulation and Object Reconstruction

In this chapter the techniques for event simulation and object reconstruction are described. Emphasis is put on reconstruction techniques and methods for objects in semileptonic  $t\bar{t}$  decays.

### 4.1 Event Generation and Detector Simulation

Event simulation and reconstruction can be divided in distinctive steps. The first step is the simulation of proton–proton collisions using event generators. These generators provide a full chain from the initial particles to the calculation of four-momenta of final state particles after hadronisation. As second step the interactions between stable particles and the detector material are simulated. The so called digitisation is the third step, where particle interactions with sensitive readout materials are processed. This is done in a way that the actual detector output including electronic signal shape is approximated (as determined for example from test beam data). Simulation, digitisation and the final reconstruction step are specific to the experiment, since they rely on the specific detector geometry and design. In CMS one common software framework is used for these tasks: CMSSW (CMS SoftWare) [35]. Geant4 [36] is used for simulation.

The main tool used for event generation in both signal and background processes for this analysis is ALPGEN [37]. It is a leading order matrix element generator, implementing higher order corrections via parton showers. It calculates the matrix element for the chosen process plus additional radiation neglecting interference effects and virtual corrections. The final hadronisation after parton shower matching is performed by Pythia [38].

Comparison with data from the Tevatron has shown that ALPGEN yields an improved estimation of event kinematics with higher jet multiplicities. This is needed for the good description of kinematics in a multi-jet environment of the main background processes which are vector boson production with additional jets, as well as the signal process itself. A detailed description of the event production with ALPGEN is given in the manual [37]. The generator settings for the data samples used in this analysis are summarised in [39] for  $t\bar{t}$  production and [40] for vector boson plus jets production. For the generation of the QCD background Pythia was used, which is a leading order generator that adds additional hard radiation in parton showering.

## 4.2 Object Reconstruction

For the reconstruction of semileptonic top pair decays input from the complete detector is needed. Standard reconstruction within CMSSW yields tracks, vertices and clusters [23]. Clusters from Ecal and Hcal are combined into *calotowers*, where several Ecal crystals are contracted with Hcal towers due to the finer granularity. These are combined to form entities that resemble particles like electrons, muons or hadronised partons as jets. In the following subsections a detailed description of the specific object reconstruction in semileptonic  $t\bar{t}$  decays is given.

### 4.2.1 Muon Identification and Reconstruction

Muons can be identified by having matching track segments in both inner tracker and muon chambers. As minimal ionising particles (MIPs) a characteristic small amount of energy is deposited in the calorimeters.

Different algorithms for muon reconstruction exist. For this analysis *global muons* are used, which are built by combining tracks from the inner tracker and the muon system and additional calorimeter information.

Muon candidates are built in several steps. Starting from track segments inside the vertex detector regions of interest are defined in the strip tracker, calorimeters and muon system. Tracks are extrapolated inside out, taking into account the magnetic field and energy loss. From the calorimeters and the muon system a compatibility value is computed, which compares hits and a MIP signature within a search cone in  $\Delta R$ . The different detector inputs and reconstruction objects are weighted with their uncertainty for the computation. Therein the subdetector geometry plays an important role, resulting in  $\eta$  and  $p_T$  dependence of the reconstruction efficiency. Finally a reconstructed muon is then

a track with associated calorimeter information that passed a threshold on track reconstruction quality and compatibility value. A detailed description of muon reconstruction and identification is given in [23].

### Muon Isolation

Muons from semileptonic  $t\bar{t}$  decays are further characterised by being isolated. Identified muons still originate from different sources. There is a fraction of semileptonic decays of hadrons resulting in prompt muons. In addition there is a chance of misidentification arising from tracking and imperfect reconstruction or *punch through* of hadrons, leaking into the muon system.

A signal muon is the direct daughter particle from a  $W$  boson decay with no associated hadronic activity. This decay results in a lepton with high energy, that is in most cases geometrically separated from any other detector activity. Especially in the active environment at a hadron collider lepton isolation is a mandatory requirement. The main isolation criteria are based on tracker and calorimeter information. A straightforward definition of isolation is based on detector activity in close vicinity of the muon. In this case a fixed cone in  $\Delta R$  around the muon direction is searched for tracks and calorimeter activity. For this analysis a cut on relative values of tracker momentum and calorimeter energy is used.

The actual isolation is mapped as a two step procedure. The first step is the determination of a fixed cone size that is searched for detector activity. In the second step the cut value is chosen.

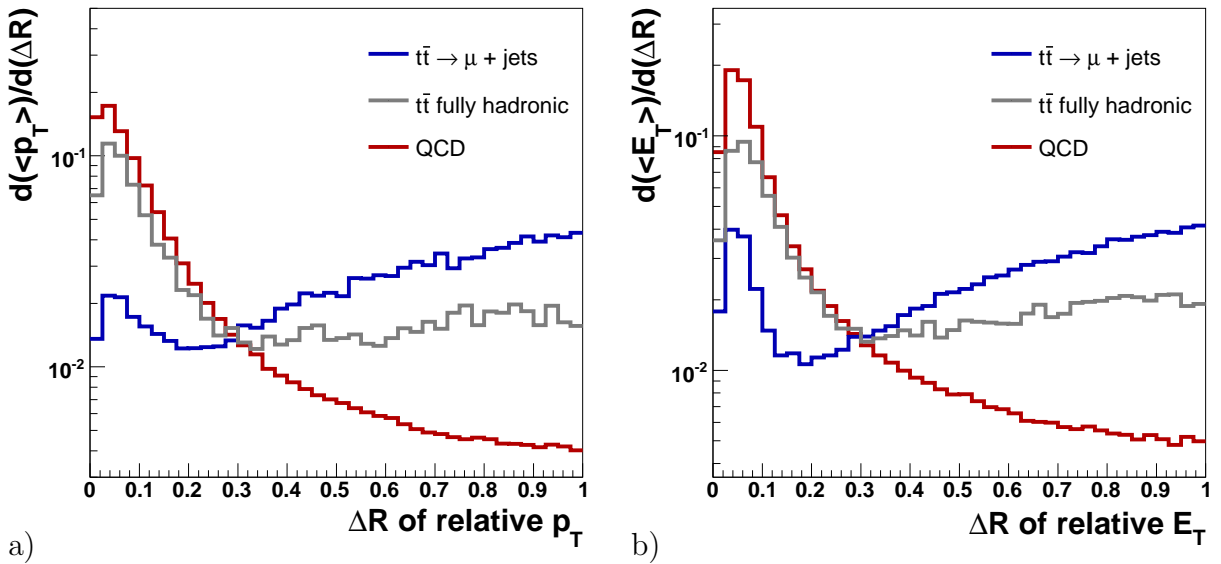
Figure 4.1a) shows the relative track  $p_T$  flow per muon as a function of its distance in  $\Delta R$  to the muon. The muon track itself is not taken into account. The  $p_T$  flow is the amount of track  $p_T$  within the  $\Delta R$  bin, averaged over a large number of events. Relative  $p_T$  means that the  $p_T$  is given in fractions of the muon  $p_T$  itself. Shown are the distributions of semileptonic  $t\bar{t}$  decays (with a muon in the final state), the fully hadronic  $t\bar{t}$  decays and the QCD background. The three channels differ significantly close to the muon itself, until they intersect at about  $\Delta R = 0.3$ . It can be seen that activity in terms of track  $p_T$  is much lower within this cone for signal muons than for the background sources. It can also be seen that therein the activity for the fully hadronic  $t\bar{t}$  decay is slightly less than for the QCD background.  $\Delta R = 0.3$  is chosen, because it was found to be best in terms of distinction power and robustness against small deviations.

Figure 4.1b) shows the average  $E_T$  flow calculated from calorimeters in proximity of the muon direction relative to the muon  $p_T$ . Inside the calorimeter only the MIP signature is collected, thus only a small fraction of the muon momentum is registered as deposition.

The basic behaviour of the three main sources close to the muon direction is the same as for the  $p_T$  flow of the tracks, although the difference between signal and background is smaller. It turns out that the optimal difference between signal and background muons is obtained by choosing a slightly smaller cone of  $\Delta R = 0.25$ .

The integrated transverse momentum of tracks (or  $E_T$  of calotowers) within the cone, divided by the transverse momentum of the muon is shown in figure 4.2. In case of the tracker isolation some mis-reconstructed tracks are found by the method. The muon track itself cannot be directly compared to other tracks due to the additional part in the muon chambers. The correct *standard* track is found by a matching in  $\Delta R$ , which usually gives an identical track. But for some muon tracks no good match is found. These tracks can be excluded by choosing a window of 10 % in summed  $p_T$ . For the calorimeter isolation it turns out, that background muons dominate summed  $E_T$  values below 5 %, which are therefore excluded. The exact values are extracted analytically from the distribution shown in figure 4.2. To summarise, an isolated muon meets the following requirements:

$$\begin{aligned} 0.9 \cdot p_{T,\mu} &\leq \sum_{\text{tracks}} p_T |_{\Delta R \leq 0.3} \leq 1.1 \cdot p_{T,\mu}, \\ 0.05 \cdot p_{T,\mu} &\leq \sum_{\text{calotowers}} E_T |_{\Delta R \leq 0.25} \leq 0.2 \cdot p_{T,\mu}. \end{aligned}$$



**Figure 4.1:** a) The average relative track  $p_T$  as a function of track distance in  $\Delta R$  to the muon without the muon track. b) The average relative calotower  $E_T$  per  $\Delta R$  to the muon including the MIP signature.

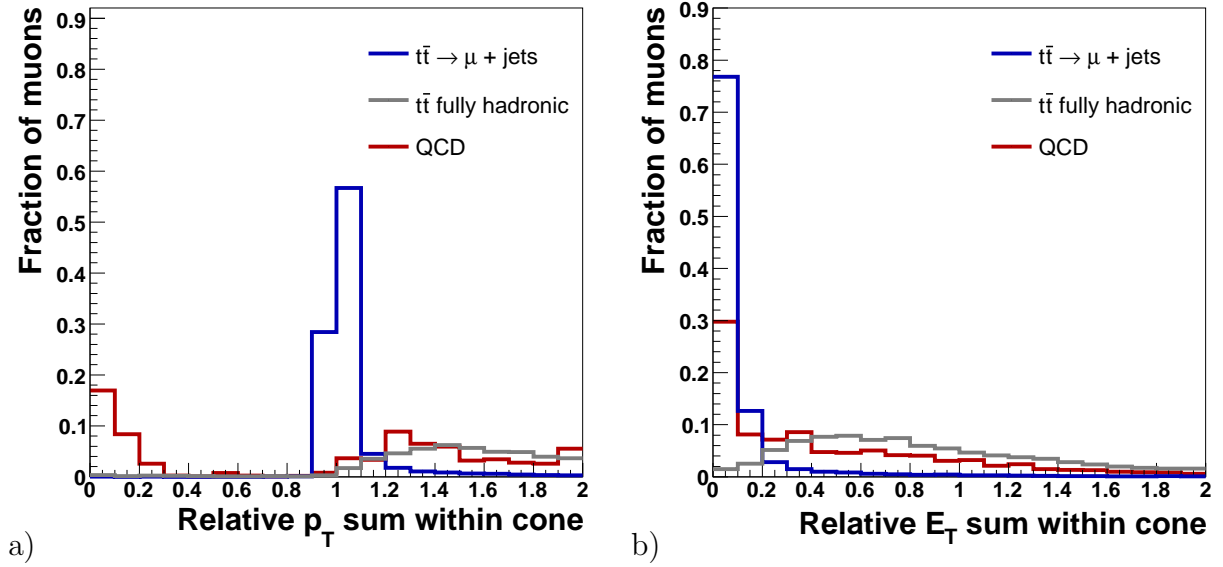


**Figure 4.2:** a) Summed track  $p_T$  within a cone of  $\Delta R = 0.3$ . The entries below 0.8 are mis-reconstructed muon candidates and can be rejected by the isolation criterion. b) Summed calotower  $E_T$  within a cone of  $\Delta R = 0.25$ . Both distributions are normalised to unity area.

## Muon Resolution

The resolution is needed at a later stage of the analysis (in chapter 5.2), so it is given for all physics objects. It is the necessary input for the kinematic fitting of the event. In simulation the angular and momentum resolution of the reconstructed objects can be determined by comparison with generator information. After a loose matching has been applied, the differences between generator and matched reconstruction object can be examined. The resolution of a variable is the width of the distribution, which is determined by a Gaussian fit.

For isolated muons with reconstructed  $p_T \geq 30$  GeV the  $p_T$ ,  $\eta$  and  $\phi$  resolution are of main interest. The largest influence on the resolution of  $\eta$  and  $\phi$  is the detector geometry, which results in a dependency of the resolution on the  $\eta$  value. The  $p_T$  resolution also depends on  $\eta$ , but additionally depends on  $p_T$  itself. Both aspects are illustrated in figure 4.3. The resolution functions from the fits are:

$$\begin{aligned}\sigma_{p_T}(p_T, \eta) &= 1.51 \cdot 10^{-4} (p_T[\text{GeV}])^2 + 0.534 |\eta| + 1.9 \cdot 10^{-2}, \\ \sigma_\eta(\eta) &= 6.2 \cdot 10^{-5} |\eta|^2 - 2 \cdot 10^{-4} |\eta| + 4 \cdot 10^{-4}, \\ \sigma_\phi(\eta) &= 3.7 \cdot 10^{-5} |\eta| + 1.4 \cdot 10^{-4}.\end{aligned}$$

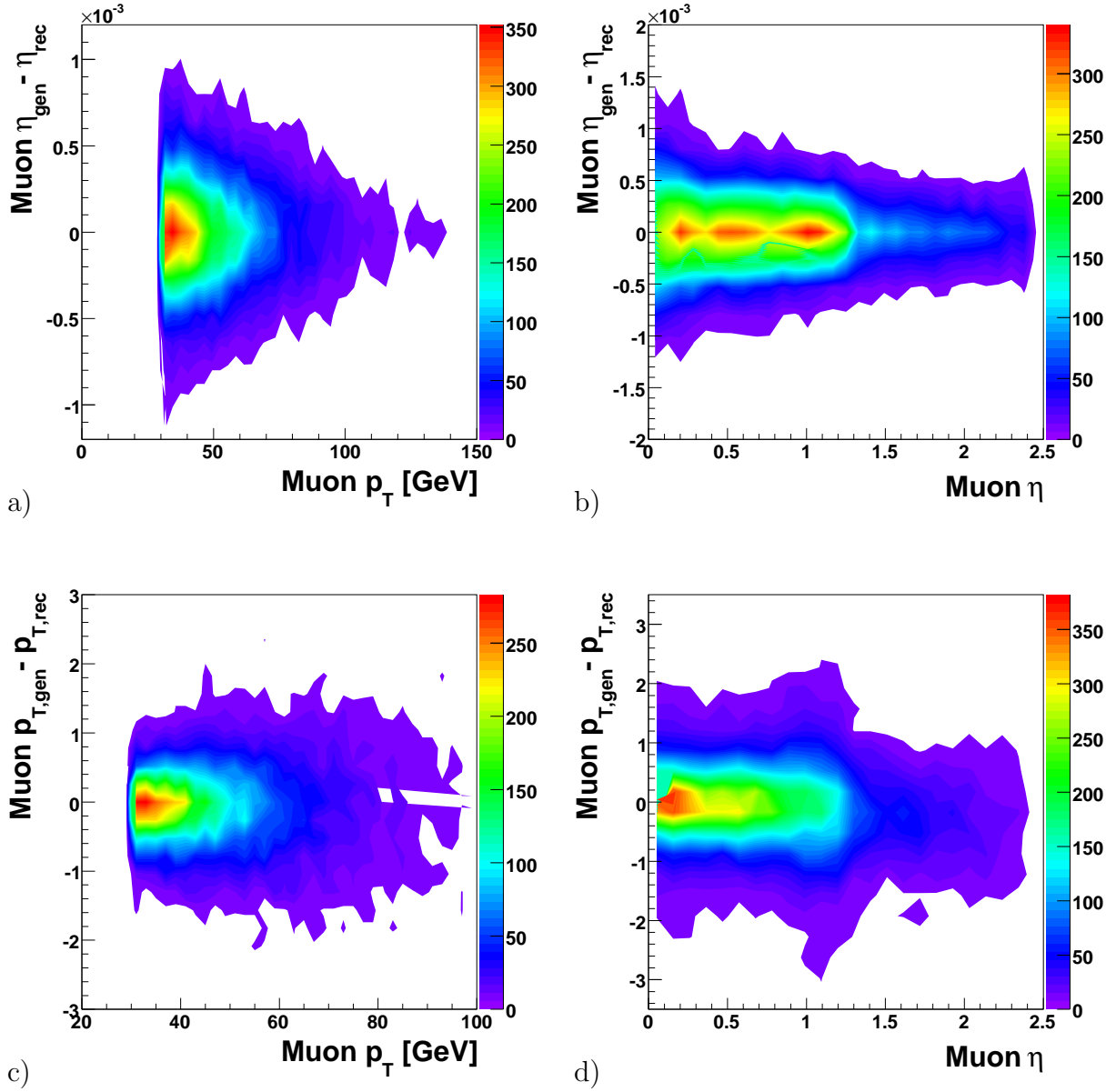


**Figure 4.3:** Example distributions for residuals of muon variables between generator and reconstruction level of  $\eta$  and  $p_T$  plotted against the  $p_T$  and  $\eta$  value of the reconstructed muon. a) shows the  $\eta$  residuals in dependence of the muon  $p_T$ , b) the same variable in dependence of  $\eta$ . c) depicts the  $p_T$  differences versus the  $p_T$  and d) the  $p_T$  residual versus the  $\eta$ . For the  $\eta$  residual width the  $p_T$  dependency is negligible, whereas for the  $p_T$  resolution both dependencies have to be taken into account.

### 4.2.2 Electron Reconstruction

Electrons are reconstructed from electromagnetic clusters inside the Ecal that have a matching track from the tracker. The fundamental challenge for electron reconstruction and identification stems from the amount of material in front of the Ecal, which sums up to 0.4-1.5 radiation lengths, depending on  $\eta$ . Due to interactions of electrons with the material there is a high probability for photon radiation or the start of showering already inside the tracker. The high magnetic field adds a further complication, because the track curvature is increased after energy loss by photon radiation. Simple Ecal cluster reconstruction may lead to an underestimation of the electron energy. Radiated photons (and thus their energy) are not always accounted for in the electron energy, since they might be geometrically separated and therefore not combined into a single cluster. Also the track reconstruction is degraded, since standard track reconstruction assumes a Gaussian distribution for the variation of hit positions from layer to layer. This assumption fails for a large fraction of electrons, since there is a high probability that they lose energy due to radiation. The electron reconstruction is enhanced in efficiency and accuracy by taking this effect into account by using an altered track filter algorithm.

Due to interaction with the tracker material and the high magnetic field the energy of a single electron is usually spread widely in  $\phi$ , due to radiated photons or showering before entering the Ecal. Cluster finding is complicated by this, the different radiated parts of the electron may form clusters that are geometrically separated. This is solved by introducing a procedure that recombines separated electron clusters into super clusters. Two different algorithms have been developed to give a good reconstruction. Starting point for both are seed crystals of relatively high energy.

In the endcaps ( $|\eta| > 1.479$ ) clusters are built from those seed crystals by using the Island algorithm [41]. Energies of adjacent crystals are summed up in both  $\phi$  and  $\eta$  directions. All crystal energies are summed until either a rise in energy or a drop below a threshold value is encountered. In the next step clusters are combined to super clusters based upon geometric selection. Along  $\phi$  a narrow window in  $\eta$  (depending on the resolution in  $\eta$ ) is searched for a possible combination of clusters. A graphical description of the procedure is shown in figure 4.4.

In the barrel ( $|\eta| \leq 1.479$ ) the Hybrid Algorithm is employed, which directly yields super clusters without forming single clusters first. It also starts from a seed crystal. At first a domino of  $1 \times 3$  crystals (or  $1 \times 5$ , depending on the seed crystal energy) in  $\phi \times \eta$  centered around the seed crystal is created. Then further dominoes in both  $\phi$  directions are added in steps, centered around the original seed crystal  $\eta$  position. If a domino has an energy below a certain threshold it is rejected. Finally all remaining dominoes along  $\phi$  are combined into a single super-cluster. A sketch of the algorithm is shown in figure 4.5.

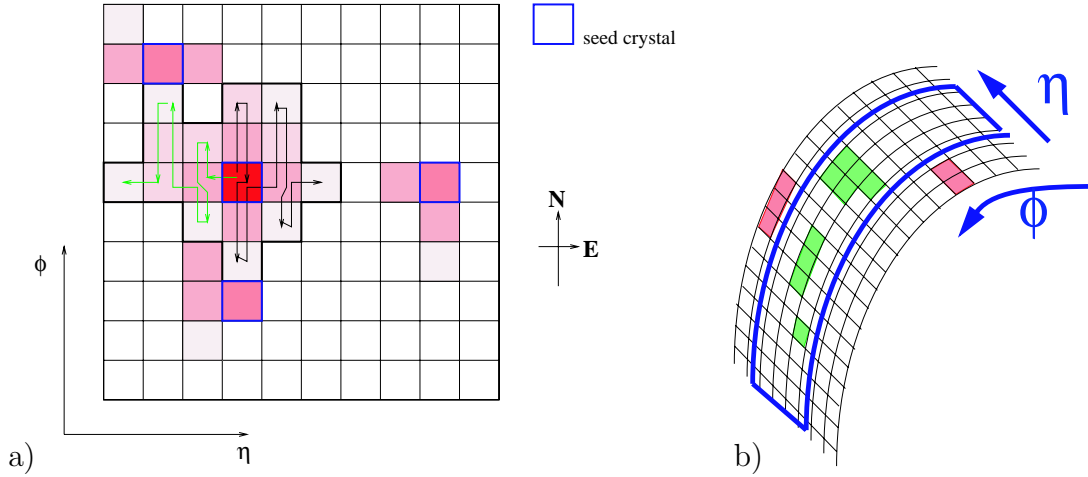


**Figure 4.4:** Schematic description of the island clustering algorithm, as employed for electron cluster reconstruction in the Ecal endcap [41]. a) First electromagnetic clusters are built from crystal hits. b) Then super clusters are built from a combination of clusters by scanning a small window in  $\eta$  along  $\phi$ . A cluster is either found compatible (green) or rejected (red).

The Hybrid Algorithm is better suited to reconstruct high energetic electrons ( $E_T > 10 \text{ GeV}$ ) than the Island Algorithm. But the different detector geometry (for example the preshower device) and a much higher background expectation in the endcap implies the necessity to have the ability to disentangle single clusters, as provided by the Island Algorithm. A detailed description of both clustering algorithms can be found in [41].

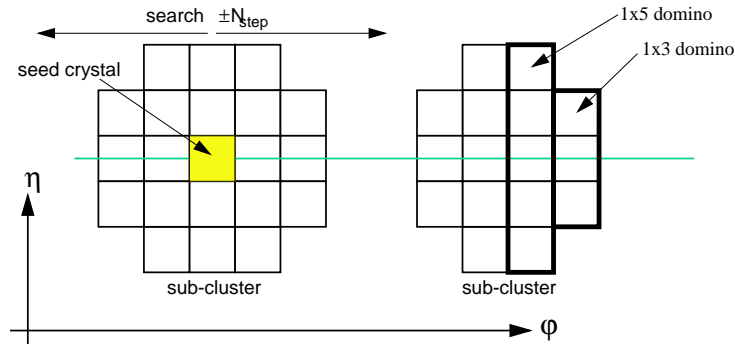


**Figure 4.5:** Graphic description of the hybrid super clustering algorithm, used for electron cluster reconstruction in the Ecal barrel [41].

In the presence of an appropriate super cluster a fixed window in the vertex detector is searched for a compatible track segment. If such a track segment exists, usually a track is built from layer to layer, from the inside to the outside of the tracker. The standard tracks are created by applying a Kalman Filter [42]. Using Kalman filtering, the next hit position is extrapolated under the assumption of a Gaussian deviation in every direction. As a high probability exists for an electron to lose energy by radiation in the tracker, causing an asymmetric distribution in hit positions of adjacent layers. This specific energy loss can be modeled into a different filtering algorithm, called Gaussian Sum Filtering (GSF) [43]. Employment of this specialised kind of track finding leads to consideration of more hits, enhancing the electron track reconstruction especially for low  $p_T$  electrons. Figure 4.6 illustrates this enhancement of using GSF tracks instead of standard Kalman filtered tracks for electrons.

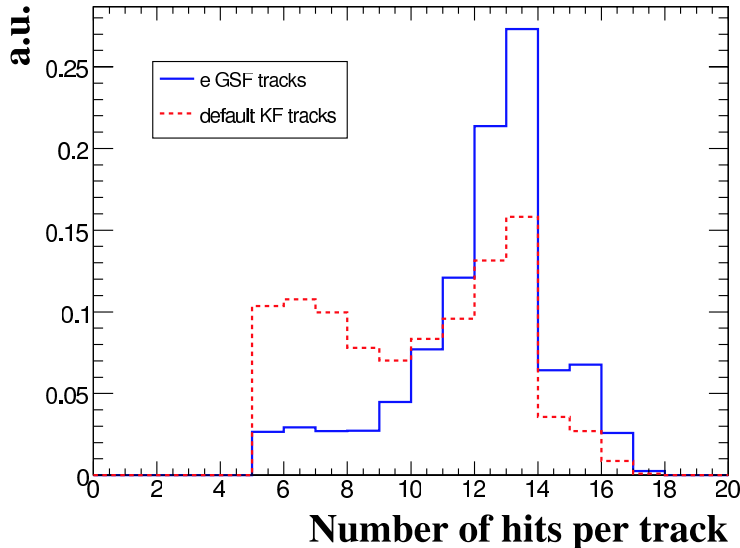


**Figure 4.6:** The number of compatible hits for an electron with  $p_T = 10$  GeV with GSF and Kalman filtered tracks [43]. More hits are taken into account for GSF tracks. Both tracking efficiency and track quality are increased by this.

If both a super cluster and a compatible GSF track exist they are combined into an electron candidate. In order to suppress the fraction of other particles that might also be reconstructed as electrons such as charged pions, kaons or photons a set of loose selection criteria are applied [43]. Basis for these are quantities from the GSF track and the respective super cluster. Additionally the electron candidates are sorted into different classes to facilitate later analysis. These classes are

- Golden electrons, which radiate almost no Bremsstrahlung and therefore are usually measured best.
- Narrow electrons, which radiate a significant part of their energy, but are still reconstructed with a single super cluster.
- Big Brem electrons, which radiate more than 50% of their energy, which is contained in a single additional cluster.
- Showering electrons, which pass the preselection cuts, but do not fit in any of the other classes.

A full and detailed description of the reconstruction procedure can be found in [43]. Test beam data and simulation show that this definition of electron candidates is almost 100% efficient for electrons above 10 GeV. This means that almost all electrons above this  $E_T$  threshold can be reconstructed. But the definition is not very exact, the electron purity of a collection of these objects is not necessarily large. Depending on the specific sample, a large fraction of the reconstructed objects are not truly electrons. Therefore a further identification based on the available observables is needed.

### 4.2.3 Electron Identification

A relatively pure identification of electrons can be achieved by a straightforward cut based approach [43]. But the full potential of electron identification of the detector cannot be exploited by this method. With growing understanding of the detector and careful study of input observables from the two different detector parts more complex methods become possible. A multivariate approach seems well suited to combine all available information, in order to enhance both efficiency and purity of electron identification. Since it is vitally important to have a particularly pure selection of electrons for  $t\bar{t} \rightarrow e + \text{jets}$  decays a multivariate method is implemented.

Several variables exist to distinguish between real and fake electrons in a method resembling a likelihood function. Similar to probability density functions for a likelihood function normalised distributions are created. To create these references a reconstructed electron must be determined to be either a true electron or fake. By comparing generator level electrons and reconstructed electrons a unique distinction can be made [43]. A reconstructed electron *candidate* is considered an electron if it can be unambiguously matched to a generator electron within a cone of  $\Delta R < 0.1$  in  $\eta\phi$  space. All other reconstructed electron candidates are considered as fakes. A technical description of the applied method is given in appendix A.

Different detector geometries and the different super cluster definition make a distinction of a barrel and an endcap part mandatory. To simplify the creation and control of the procedure the four classes mentioned above are merged into two. To introduce nomenclature for this

- the *Non Showering Electrons* comprise the Golden and the Narrow electrons;
- the *Showering Electrons* are the complementary class, a conjunction of the Big Brem and the initial Showering class.

This identification scheme results in two times two different sets of reference distributions for the non showering/showering class and the barrel/endcap part.

The complete list of variables and cut values in dependence of classification is given in Table 4.1. Additional observables exist that can be used for electron identification. But these are either strongly correlated among each other and the ones used here, or do not give much additional distinction power. A proposal is under discussion to fully exploit the discrimination potential of some additional correlated variables [44].

The normalised reference histograms of *showering* electrons in the *barrel part* are shown as example. The distributions of the other classes are shown in appendix B, where also the correlations between the observables are summarised.

The first group of observables compares the geometrical matching between the super cluster and the track. In figure 4.7a) the normalised reference distribution for  $\Delta\eta = \eta_{track} - \eta_{SC}$  is shown, where  $\eta_{track}$  is the  $\eta$  value of the track extrapolated to the vertex, and  $\eta_{SC}$  the  $\eta$  value of the super cluster. The resolution of  $\eta_{SC}$  is only a little wider than

Variable	Non Showering		Showering	
	Barrel	Endcap	Barrel	Endcap
$\Delta\eta$	$[-5, 5] \cdot 10^{-3}$	$[-0.005, 0.005]$	$[-0.015, 0.015]$	$[-0.01, 0.01]$
$\Delta\phi_{in}$	n.a.	$[-0.02, 0.02]$	$[-0.1, 0.1]$	$[-0.1, 0.1]$
$\Delta\phi_{out}$	$[-0.02, 0.02]$	n.a.	n.a.	n.a.
$ \frac{1}{E_{SC}} - \frac{1}{p_{track}} $	$[0, 0.03]$	$[0, 0.1]$	$[0, 0.1]$	$[0, 0.15]$
$\frac{E_{Hcal}}{E_{Fcal}}$	$[-0.05, 0.1]$	$[-0.02, 0.05]$	$[-0.05, 0.19]$	$[-0.03, 0.19]$
$\sigma_{\eta\eta}$	$[0, 2.3] \cdot 10^{-4}$	$[0, 1] \cdot 10^{-3}$	$[0, 4] \cdot 10^{-4}$	$[0, 0.0015]$
$E_{\frac{3 \times 3}{5 \times 5}}$	$[0.75, 0.99]$	$[0.9, 1]$	$[0.5, 1]$	$[0.5, 1]$

**Table 4.1:** The cut values for electron candidates in the different classes that are taken into account for identification.

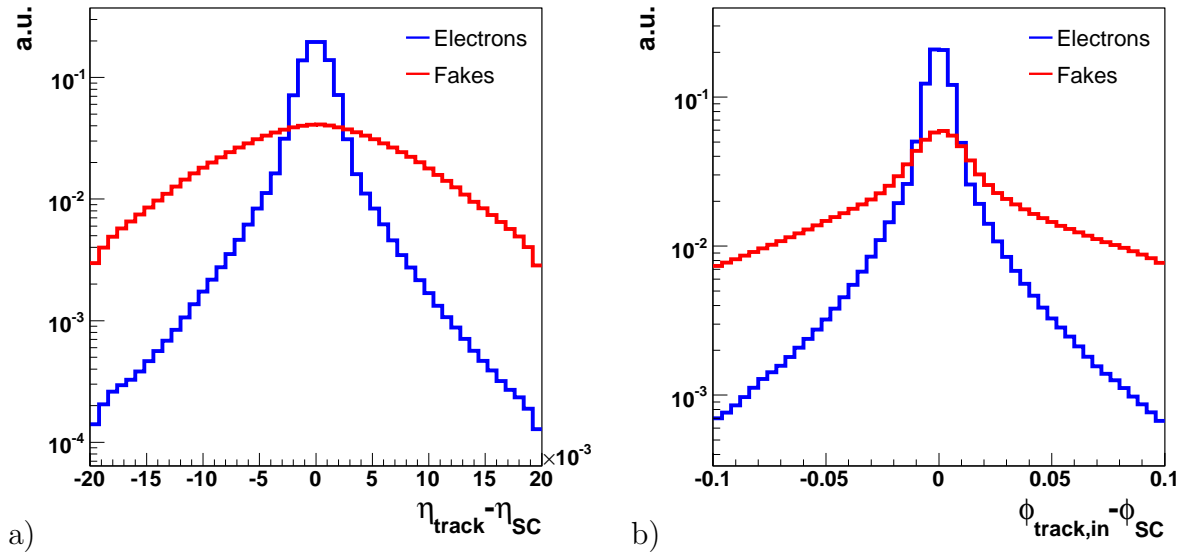


**Figure 4.7:** a) Pseudorapidity difference of the track extrapolated to the vertex and the super cluster, shown for showering electron candidates in the barrel. b) Difference between the  $\phi$  position for track (at vertex position) and super cluster, for showering electron candidates in the barrel. The absolute matching is worse by an order of magnitude, which results from the looser and more complicated definition of the  $\phi$  position of the super cluster. The distributions are normalised to unity area.

the width of a crystal. Usually the super cluster and the track of an electron have the same  $\eta$  value. This variable is very well suited for the identification in all classes.

Figure 4.7b) depicts the normalised reference distribution for  $\Delta\phi_{\text{in}} = \phi_{\text{track,in}} - \phi_{\text{SC}}$ , where the  $\phi$  of the track is extrapolated to the vertex. In comparison to the  $\eta$  difference, the  $\phi$  position of a super cluster is harder to compute for any of the electron classes but those that contain only a single cluster. As a result the distribution is much broader than for  $\Delta\eta$ . But still the matching between the  $\phi$  of the track and the super cluster is better for electrons. The discrimination power is given in all classes.

For the non showering electron class in the barrel a better choice is given by comparing the  $\phi$  values at the interface of tracker and Ecal. In all other classes the  $\phi$  position of the super cluster is not well enough defined.

Figure 4.8 depicts the normalised reference distribution for  $|\frac{1}{E_{\text{SC}}} - \frac{1}{p_{\text{track}}}|$ . In all classes a good distinction is possible. Different choices are possible for the combination of track momentum and super cluster energy. This choice has the lowest correlations to the other

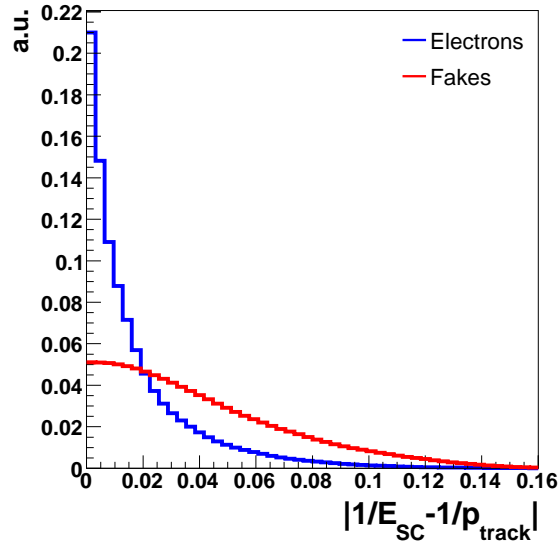


**Figure 4.8:** The observable  $|\frac{1}{E_{SC}} - \frac{1}{p_{track}}|$  for showering electron candidates in the barrel. True electrons tend to have similar values for track momentum and cluster energy, making the difference of the inverse values very small. The distributions are normalised to unity area.

variables. The inverse track momentum is the actual observable in track reconstruction.

Figure 4.9a) shows the reference distribution of the ratio of energies deposited in the Hcal and the Ecal  $\frac{E_{Hcal}}{E_{Ecal}}$ . The Hcal energy is taken from the Hcal deposition that is geometrically matched to the Ecal super cluster position. This variable is well suited to distinguish any of the classes. It takes advantage of the fact that electrons alone do not have any associated hadronic activity. The distinction power gets decreased by not demanding to have isolated electrons. Due to this some electrons have an association with energy depositions in the Hcal.

In figure 4.9b) the normalised reference distribution for another shower shape variable,  $\sigma_{\eta} = \sum_{5 \times 5} (\eta_{crystal} - \eta_{seed\ crystal})^2 \cdot \frac{E_{crystal}}{E_{5 \times 5}}$  is depicted. It quantifies the longitudinal shower spread, the  $\eta$  extension of the super cluster. Usually the  $\eta$  spread is no more than a few crystals, leading to small values of the observable for true electrons. The observable helps to distinguish within all classes of electron candidates.

Figure 4.10a) shows the normalised reference distribution of a variable sensitive to the lateral shower shape both in  $\eta$  and  $\phi$  direction:  $E_{\frac{3 \times 3}{5 \times 5}}$ . It is the ratio of the energies deposited in a  $3 \times 3$  crystal matrix over the deposition in a  $5 \times 5$  crystal matrix, centered to the same crystal. Figure 4.10b) shows a figurative description of the observable for a hadronic particle and an electron. Due to the broader lateral extension of the hadronic

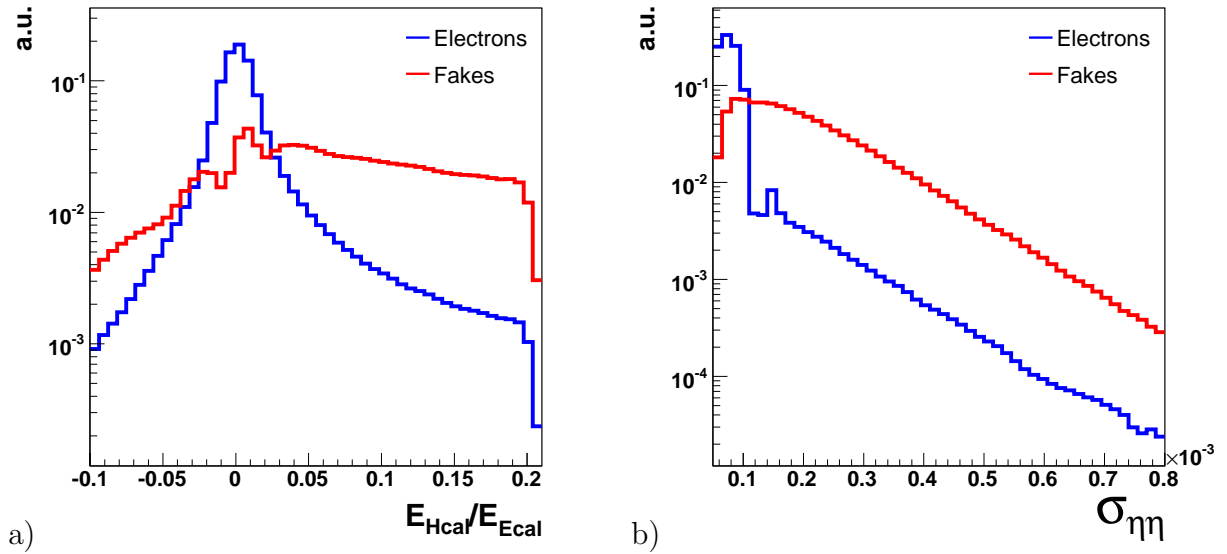


**Figure 4.9:** a) Ratio of energies deposited in the Hcal and the Ecal, for showering electron candidates in the barrel. Most of the true electrons do not have any hadronic activity, resulting in values around zero. The small fluctuations mainly come from Hcal calibration, which allows values below zero. Included are electrons that are part of jets, thus being associated to hadronic activity which gives rise to the tail to higher values. Fakes can be seen to be mainly of hadronic nature, showing a significant amount of deposited energy in the Hcal. b) The longitudinal ( $\eta$ ) shower spread  $\sigma_{\eta\eta}$  for showering electron candidates in the barrel. Since true electron showers are well contained in  $\eta$  this leads to small values in  $\sigma_{\eta\eta}$ . The somewhat irregular structure for electrons is a result of the crystal segmentation in  $\eta$  [44].

shower the ratio tends to be larger than for the relatively narrow electromagnetic showers created by electrons (and photons). It helps to distinguish all electron classes, with less power in the showering class due to the non-trivial calculation of the  $\phi$  position of a super cluster.

### Electron Identification Performance

The final step in the electron identification is the extraction of the final cut value on the likelihood ratio LHR (definition see appendix A).

Since the a-priori probability for the occurrence of electrons is unknown at present the performance prediction of electron identification is an approximation. The two main

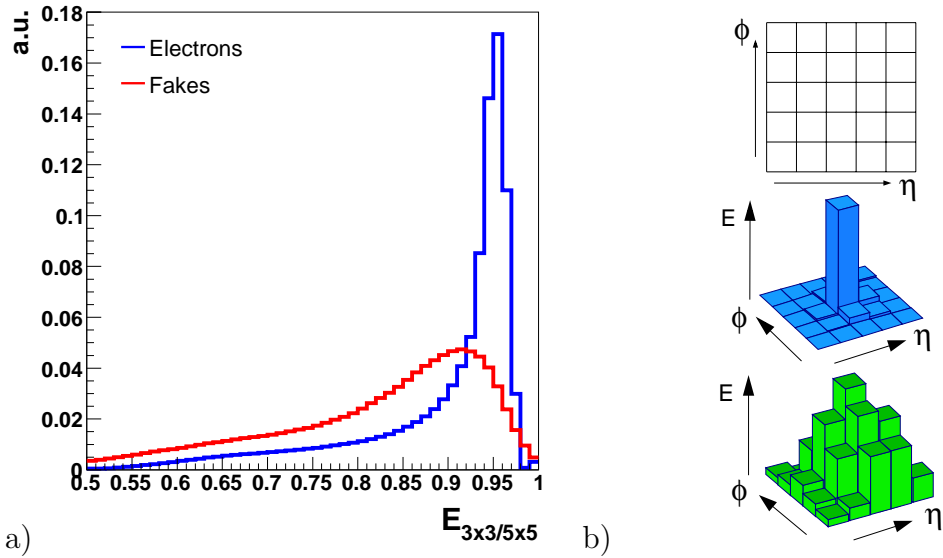


**Figure 4.10:** a) The normalised reference distribution for  $E_{\frac{3 \times 3}{5 \times 5}}$  for showering electrons in the barrel. The ratio is close to one for electromagnetic showers arising from true electrons. Fakes show a different peak position and have a much broader distribution. b) A graphical explanation for this shower shape variable. A  $5 \times 5$  crystal array is considered. In the middle the energy profile of an electromagnetic shower is shown; the energy is mostly contained in a single crystal. Below the energy profile for a hadronic shower is depicted, showing a larger spread in both directions.

measures of performance are the purity and the efficiency of the identification procedure. Purity  $p$  and efficiency  $\epsilon$  for a certain cut value on the likelihood ratio are defined as:

$$p = \frac{N_{\text{electrons}}|_{\text{after cut}}}{N_{\text{electrons}}|_{\text{after cut}} + N_{\text{fakes}}|_{\text{after cut}}}$$

$$\epsilon = \frac{N_{\text{electrons}}|_{\text{after cut}}}{N_{\text{electrons}}|_{\text{before cut}}}$$

Especially the purity depends heavily on the data input. If for example an inclusive  $t\bar{t}$  sample is used for performance evaluation, the achievable purity is high. A lot of true electrons are present in this sample and the number of fakes is limited. If a pure di-jet sample is used, almost no electrons are present, leading to a very low purity.

To determine the likelihood ratio cut values the following evaluation scheme has been applied. Unbiased (without the application of triggers or any other cuts than those needed for electron identification) event samples have been used for the performance evaluation.

For the background a QCD multi-jet sample has been used, for the true electrons an additional semileptonic  $t\bar{t} \rightarrow e + \text{jets}$  sample.

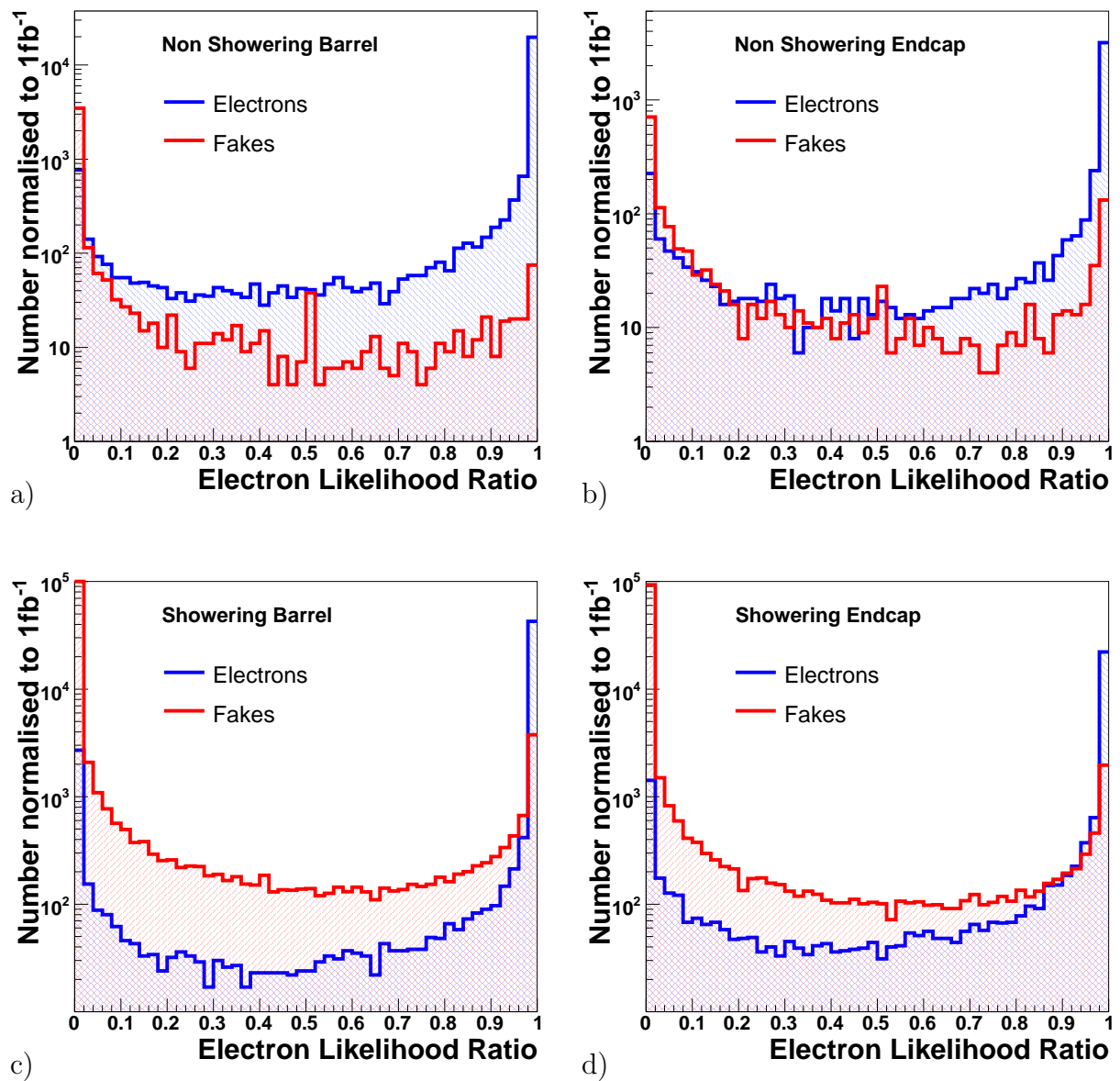
The purity and efficiency values shown here are underestimated, since the inclusion of triggers and quality cuts are more likely to enhance the signal fraction. It should be also noticed that for the given values the detector input needs to be well understood and under control.

Figure 4.11 shows the resulting likelihood ratio distributions for all four classes. It can be seen that a good identification is well possible for the non showering electrons, especially in the barrel. Here it is particularly difficult to obtain a good background description due to low statistics. The situation is different for the showering classes, especially in the endcap, where the amount of background is substantially larger. The identification is still well possible.

The final cut value has been determined from maximising the product of purity  $\times$  efficiency. The likelihood ratio cut values are summarised in table 4.2 along with the efficiency and purity values.

	LHR cut	efficiency	purity
non showering barrel	0.4	0.97	0.96
non showering endcap	0.99	0.93	0.86
showering barrel	0.999	0.89	0.92
showering endcap	0.999	0.86	0.87

**Table 4.2:** The cut values on the likelihood ratio for the four different electron candidate classes. The efficiency and purity values are only estimates as described in the text. Still it can be seen that the identification of the non showering classes is both simpler and more efficient.



**Figure 4.11:** Likelihood ratio performance distributions for the four classes. True electrons are taken only from semileptonic  $t\bar{t} \rightarrow e + jets$  events, fakes are sampled from QCD events only. All entries are normalised to the expected number in  $1 \text{ fb}^{-1}$ . a) is for the non showering barrel, b) for the non showering endcap. c) is the distribution for showering barrel and d) is the result of the showering endcap.

## Electron Isolation

In principle the same argumentation about isolation of muons is true for electrons. It also follows the same scheme as for muons in terms of tracker and calorimeter isolation. But the actual method is more complicated than for muons. The background rates are much higher because of the more complicated reconstruction based on clusters and tracks. In addition the electron isolation is more complicated to define. The actual comparison of tracks and clusters is less straightforward. As mentioned before electron reconstruction uses special electron clusters and tracks. This implies the usage of a geometrical matching in  $\Delta R$  of the electron objects to the standard tracks and calotowers.

Figure 4.12a) shows the relative  $p_T$  flow of tracks around the direction of the electron track. Direct track subtraction is not possible due to the different nature of tracks, but a clear distinction between the different sources is possible. Figure 4.12b) shows the relative  $E_T$  flow of calotowers around the position given by the electron track. The loose definition of the super cluster position makes a clear subtraction of the clusters more complicated. Instead of assembling clusters in a complicated procedure calotowers can be used, even though the electron cluster is quite extended in its geometrical radius in  $\Delta R$ . Optimal for both isolations is a cone size of  $\Delta R = 0.3$ . This is determined analytically from computing the ratio of summed  $p_T$  of the different sources within this cone. Figure 4.13 shows the summed track and calotower energies. The optimal cut values are extracted again analytically from these distributions. An isolated electron has the following properties:

$$\begin{aligned} \sum_{\text{tracks}} p_T |_{\Delta R \leq 0.3} &\leq 1.05 \cdot p_{T,e}, \\ \sum_{\text{calotowers}} E_T |_{\Delta R \leq 0.3} &\leq 1.08 \cdot p_{T,e}. \end{aligned}$$

## Electron Resolution

Again only isolated electrons with  $p_T \geq 30$  GeV are examined analogous to the muons (see section 4.2.1). The detector geometry has an influence on all reconstruction variables, resulting in a  $\eta$  dependency of the resolutions of  $p_T$ ,  $\eta$  and  $\phi$ . Also the electron  $p_T$  resolution depends on the  $p_T$  itself.

Due to the highly varying amount of material in the barrel part, the  $\eta$  dependence of the  $p_T$  resolution needs to be distinguished in three regions. The endcap is a single region, but the barrel needs to be distinguished into a central and an outer part.

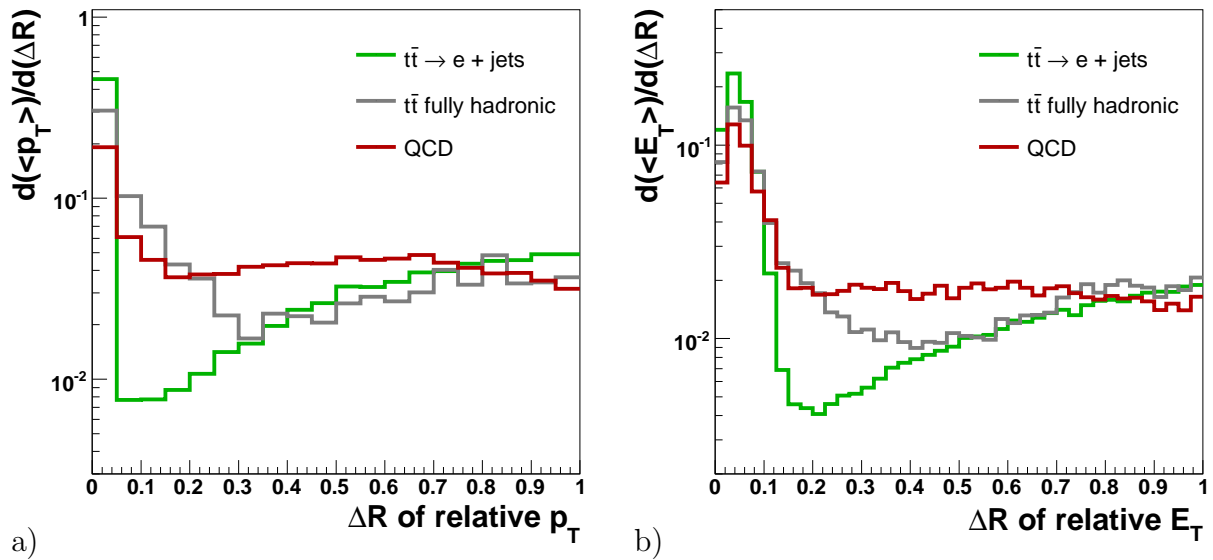


**Figure 4.12:** a) The average relative track  $p_T$  as a function of track distance in  $\Delta R$  to the electron track. b) The average relative  $E_T$  calculated from calorimeters as a function of  $\Delta R$  distance with respect to the electron track.

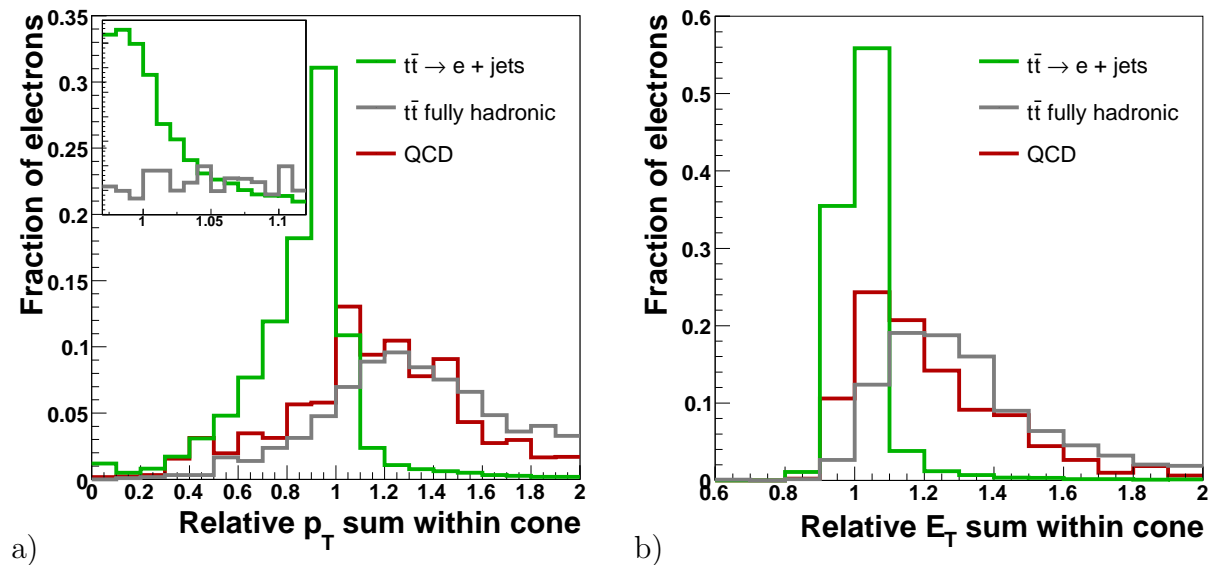


**Figure 4.13:** a) Summed track  $p_T$  within a cone of  $\Delta R = 0.3$ . The insert shows the region of interest, indicating the chosen cut value of 1.05 at the crossover point. b) Summed calorimeter  $E_T$  within a cone of  $\Delta R = 0.3$ . Both integrals are given as fractions of the electron  $p_T$ .

The fitted resolutions for isolated electrons are:

$$\begin{aligned}\sigma_{p_T}(p_T, \eta) &= 0.201 \cdot \sqrt{p_T[\text{GeV}]} + \begin{cases} -0.28 |\eta| + 0.54 & , |\eta| \leq 0.8 \\ 1.52 |\eta| - 1.07 & , \text{in between} \\ -0.158 |\eta|^2 + 0.97 & , |\eta| \geq 1.4 \end{cases} \\ \sigma_\eta(p_T) &= -8.5 \cdot 10^{-5} |\eta| + 4 \cdot 10^{-4} \\ \sigma_\phi(p_T) &= 7.6 \cdot 10^{-5} |\eta|^2 - 7.7 \cdot 10^{-5} |\eta| + 5.8 \cdot 10^{-4}\end{aligned}$$

#### 4.2.4 Jet Reconstruction

The direct observation of partons in the detector is impossible. Partons that were produced in a collision immediately hadronise and if they have sufficient transverse momentum they interact with the detector. To reconstruct the partons the detector input of calorimeters is clustered and combined by a jet algorithm. The jet algorithm is defined as a two steps procedure. First associations between the objects are determined, and in the second step the objects that belong together are recombined into jets. An overview of jet definitions for hadron colliders is given in [45].

For this analysis the  $k_T$  clustering algorithm is chosen [46]. It is theoretically well defined in terms of infra-red safety, collinear safety and order independence.

The algorithm starts with an empty list of jets and a list of pre-clusters (in the beginning: calorimeters). The procedure is:

1. Define for each pre-cluster  $i$  the value  $d_i = p_{T,i}^2$  and for each pair  $(i, j)$  with  $(i \neq j)$

$$d_{ij} = \min(p_{T,i}^2, p_{T,j}^2) \frac{(y_i - y_j)^2 + (\phi_i - \phi_j)^2}{R^2},$$

where  $R$  is a parameter of the jet algorithm.

2. Find the minimum  $d_{\min}$  of all  $d_i$  and  $d_{ij}$ .
3. If  $d_{\min}$  is a  $d_{ij}$ , then merge the calorimeters by the recombination scheme and put it into the list of pre-clusters.
4. If  $d_{\min}$  is a  $d_i$  (a pre-cluster), then remove it from the list of pre-clusters and add it to the list of jets.
5. Repeat from step 1, until no pre-cluster is left.

The recombination scheme determines how the four-vectors are added. In the analysis a mass-less scheme was used. The recombined objects including the final jets have zero mass.

Besides the choice of input, the algorithm is fully determined by the choice of a  $R$  parameter value. The  $R$  parameter is usually considered to be a distance-like quantity, since it is used as a denominator to the angular distance in rapidity and azimuth.

For this analysis a value of  $R = 0.6$  was chosen.

### Jet Energy Correction

The reconstructed jet is correlated in its kinematical properties with the parton, but additional correction is needed. Especially the jet energy is subject to large modification. The reason is the underlying hadronic calorimeter response, which is non-linear in energy and  $\eta$ , leading to a complex correction.

With data the  $\eta$  calibration can be extracted from the  $p_T$  balance of di-jet events. In this method two hard jets recoiling against each other are taken to be balanced, additional hard radiation is rejected by cutting on the third highest jet  $E_T$ . The  $E_T$  dependent calibration can be extracted from  $\gamma/Z + jets$  events, with the  $Z$  decaying in  $e^+e^-$  or  $\mu^+\mu^-$  pairs. In those events a hard photon or a  $Z$  boson recoils against a hard jet. Momentum conservation forces a balance in  $E_T$ . This technique exploits the much better absolute energy resolution of the electromagnetic calorimeter and/or the tracker. It is crucial for these data driven methods to gain control of the systematic influences. The full description of these methods, including a description of Monte Carlo based approaches is given in [47].

A generalised method exists for simulation [48]. One option is to perform a single jet energy correction for all kinds of jets. Another option is to factorise it, that is to mix identification with the correction process, since heavy flavour jets need a significantly different correction. The factorised approach seems better suited for semileptonic  $t\bar{t}$  decays, since half of the expected jets are b-jets (see next subsection). As it is not available for the used software version, a similar, completely Monte Carlo based method is implemented here.

The fundamental problem for any correction or calibration procedure is the huge asymmetric spread in reconstructed energy. This can be seen from looking at the ratio of energies of a matched pair of reconstructed jet (*RecJet*) and jet on generator level (*GenJet*). The RecJets are built from calotowers and the GenJets from final state hadrons, respectively. Figure 4.14a) shows the ratio of GenJet and RecJet energy as a function of

the reconstructed jet  $E_T$  and jet  $\eta$  position. The huge spread especially at low energies makes an effective straightforward correction algorithm very hard to define.

For the comparison a matching between generator and reconstruction level is needed. A jet is called matched if the two jet axes are no further apart than  $\Delta R = 0.05$ . To suppress ambiguities no other jet may exist within in a cone of  $\Delta R = 0.6$ . To determine a correction factor the  $E_T$  ratio of the paired jets is studied in dependence of the  $E_T$  and  $\eta$  values of the reconstructed jet.

To find a parametrisation of the correction the ratio  $R_0$  can be determined as a function in  $\eta$  and  $E_T$ :

$$R_0(\eta, E_T) = \frac{E_{T,GenJet}}{E_{T,CaloJet}}.$$

The functional form can be extracted by fitting a Gaussian distribution, which is an approximate description around the peak position. An unbinned maximum likelihood method is used for the fitting procedure. Closure is tested by applying the parametrised correction to the sample from which the correction was extracted, which should yield a ratio of one after correction. It is possible to distinguish the jet flavour on generator level, especially if it is a b- or a non-b-jet [49]. The correction is extracted in dependence of the determined flavour, as well as without this information. Both corrections are used in the analysis. The flavour-independent correction is used in the generic event selection in the next chapter, the additional flavour correction is applied for specific event reconstruction.

The jet energy ratios as a function of  $E_T$  and  $\eta$  after applying the correction are shown in figure 4.15.

The  $\eta$  correction is divided into two regions for the barrel and the endcap part. The correction functions for b-jets  $c_B$  and for non b-jets  $c_{NB}$  is are:

$$c_B(E_T, \eta) = \frac{1}{4.33 \cdot 10^{-3} (E_T[\text{GeV}])^2 - 0.209} + \begin{cases} 0.063 |\eta|^2 + 1.34 & , |\eta| < 1.4, \\ -0.321 |\eta| + 1.89 & , |\eta| \geq 1.4, \end{cases}$$

$$c_{NB}(E_T, \eta) = \frac{1}{2.32 \cdot 10^{-2} (E_T[\text{GeV}])^2 - 0.209} + \begin{cases} 0.062 |\eta|^2 + 1.44 & , |\eta| < 1.4, \\ -0.423 |\eta| + 2.13 & , |\eta| \geq 1.4. \end{cases}$$

## Jet Resolution

The resolution of jet  $E_T$ ,  $\eta$  and  $\phi$  is determined in the same way as for the muon and electron (see section 4.2.1). Since the definition of jets is less precise, the matching criterion has to be chosen more loosely to suppress the introduction of a bias by comparing only tightly matched objects. The main influence on the resolution is the jet  $p_T$ , which is a feature of the jet algorithm. The geometry influence that shows as  $\eta$  dependency can be neglected for the resolution of the angular variables.

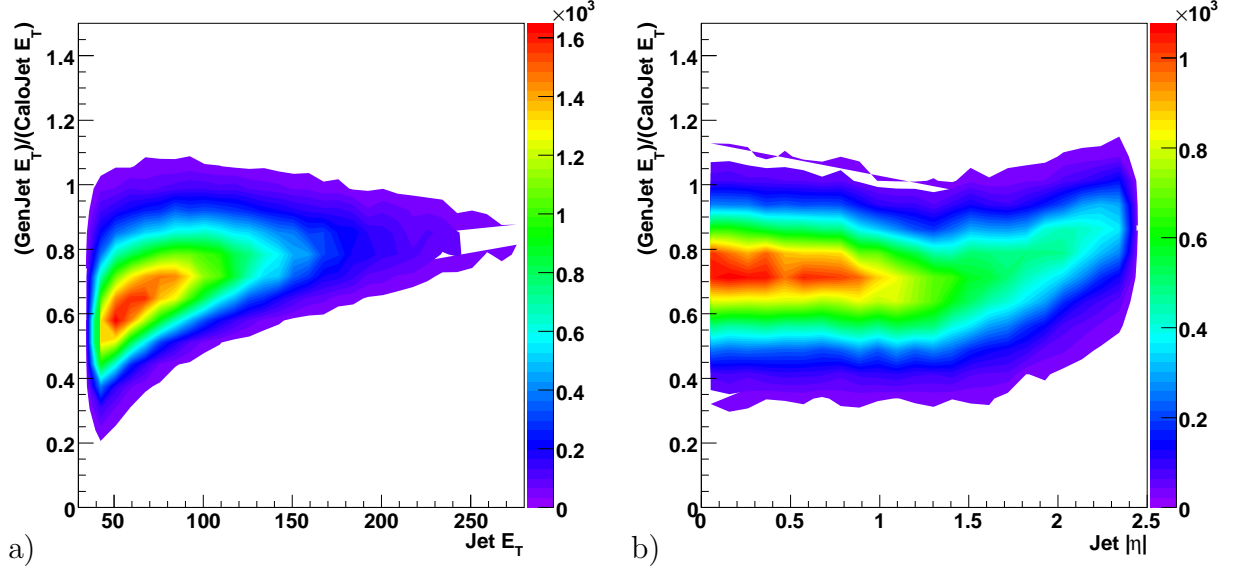


**Figure 4.14:** The ratio of transverse energies of matched jets on reconstructed and generator level (after hadronisation) before any correction. a) The distribution as a function of the reconstructed jet  $E_T$ . b) The distribution of ratios as a function of the reconstructed jet  $\eta$ .

The transverse momentum resolution depends on  $p_T$  and  $\eta$  for the endcap. In the central detector part the  $\eta$  dependency is also negligible. Since the flavour information is important a distinction is made between b- and non-b-jets. The identification of b-jets on reconstruction level is explained in the following section.

For the non-b-jets the resolution can be parametrised as:

$$\begin{aligned}\sigma_{E_T}(E_T, \eta) &= 0.29 \cdot \sqrt{E_T[\text{GeV}]} + \begin{cases} 6.68 & , |\eta| < 1.4 \\ -3.14 \cdot |\eta| + 11.89 & , |\eta| \geq 1.4 \end{cases} \\ \sigma_\eta(E_T) &= -1.5 \cdot 10^{-4} E_T[\text{GeV}] + 0.049 \\ \sigma_\phi(E_T) &= -2.7 \cdot 10^{-4} E_T[\text{GeV}] + 0.06\end{aligned}$$

Resolutions for the b-jets are:

$$\begin{aligned}\sigma_{E_T}(E_T, \eta) &= 0.333 \cdot \sqrt{E_T[\text{GeV}]} + \begin{cases} 6.57 & , |\eta| < 1.4 \\ -1.09 \cdot |\eta| + 8.50 & , |\eta| \geq 1.4 \end{cases} \\ \sigma_\eta(E_T) &= -1.2 \cdot 10^{-4} E_T[\text{GeV}] + 0.047 \\ \sigma_\phi(E_T) &= -2.1 \cdot 10^{-4} E_T[\text{GeV}] + 0.054\end{aligned}$$

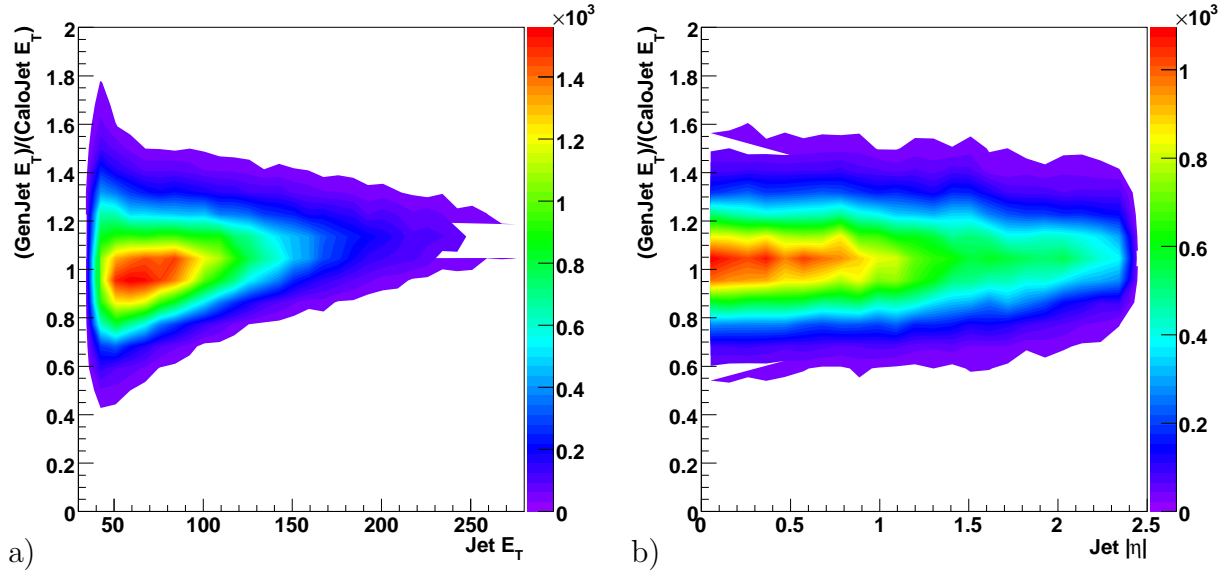


**Figure 4.15:** The ratio of transverse energies of matched jets on reconstructed and generator level (after hadronisation) after applying the correction. a) shows the distribution as a function of the reconstructed jet  $E_T$ , b) depicts the ratio as a function of jet  $\eta$ .

### 4.2.5 B-Jet Identification

The decay chain of any top quark contains almost always a bottom quark. With b-tagging it is possible to identify b-quark decays based on detector reconstruction objects.

B-hadrons, which are instantly formed from the bare bottom quark are relatively long lived. The decay into its doublet partner is kinematically forbidden and cross-generation decays are suppressed. B-hadrons have a lifetimes of about  $\tau_b \approx 1.6$  ps, resulting in decay lengths of up to macroscopic distances of several mm (including a Lorentz boost  $\gamma$ ):

$$d = \gamma \cdot c \cdot \tau_b \approx \gamma \cdot 500 \mu\text{m}.$$

On average five charged particles are produced in a B-hadron decay. Both properties are exploited in track and impact parameter based b-tagging [50].

A jet is associated to a certain vertex by reconstructed tracks. In the *probabilistic method* these tracks are input to a computation that checks the compatibility to the primary vertex. If this probability is low, the jet is likely to be a b-jet [50]. Of key importance is the track impact parameter, the smallest distance of a track to the primary vertex. Since the LHC beam spot is very small in the transverse plane (about  $15 \mu\text{m}$ ), especially the transverse impact parameter is well defined.

Experimentally the impact parameter significance is a suitable observable, which is the ratio of the track impact parameter and its uncertainty. Figure 4.16 shows the asymmetric distributions of the two-dimensional transverse and the three-dimensional track impact parameter significances for different flavours of jets. Light quark and gluon jets (udsg-

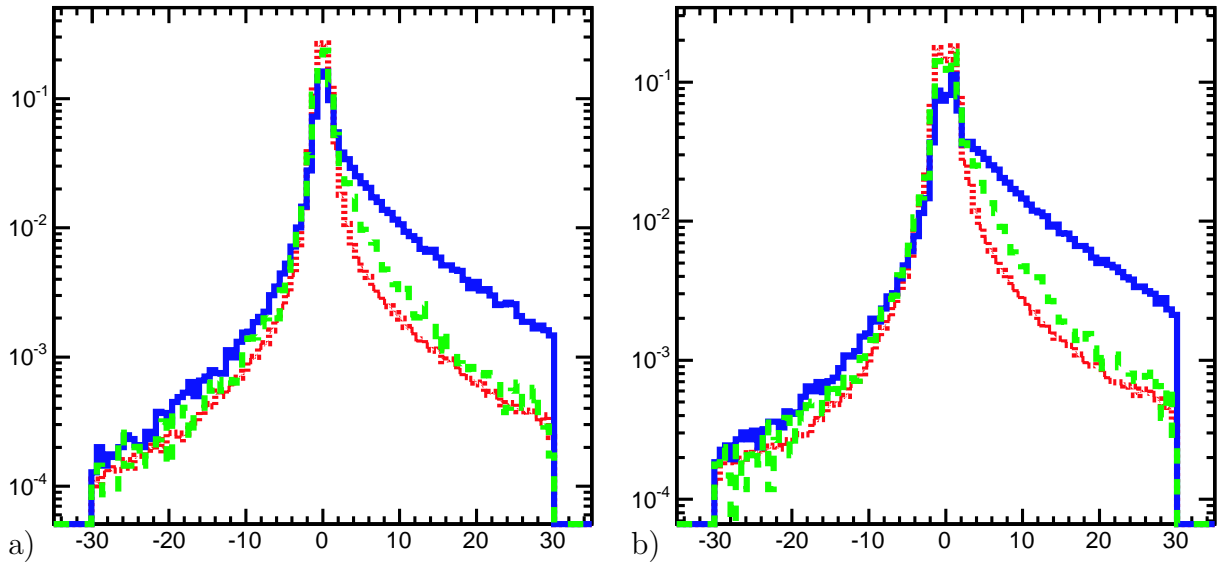


**Figure 4.16:** a) Transverse and b) three-dimensional impact parameter significance distributions [50]. B-jet distributions are drawn with blue solid lines, charmed jets with green dashed lines and the udsg-jets with the red dotted line.

jets) are centered around zero and have unit width. Tracks from b- and c-jets show an asymmetric distribution to positive values, reflecting the longer lifetimes of B- and C-hadrons [50]. Negative values of the track impact significance corresponds to tracks that have their smallest distance on the other side of the vertex with respect to the associated jet.

It is possible to compute a resolution function from the tracks with negative impact parameters, which is used to define a significance function. The jet probability is defined as the confidence level for a number of tracks with zero lifetime to be compatible with measured tracks associated with a jet. From this probability a discriminating value can be computed. Figure 4.17 shows the distribution of discriminator values for b-, c- and the light quark jets in  $t\bar{t}$  events [50].

This approach is relatively simple and robust, although some irreducible background is also collected from other long-lived hadrons. Higher efficiency and lower mis-tagging rates can be achieved by using more complex techniques. Since these were still in development for the present software version, the track impact parameter based *Jet Probability* is used.

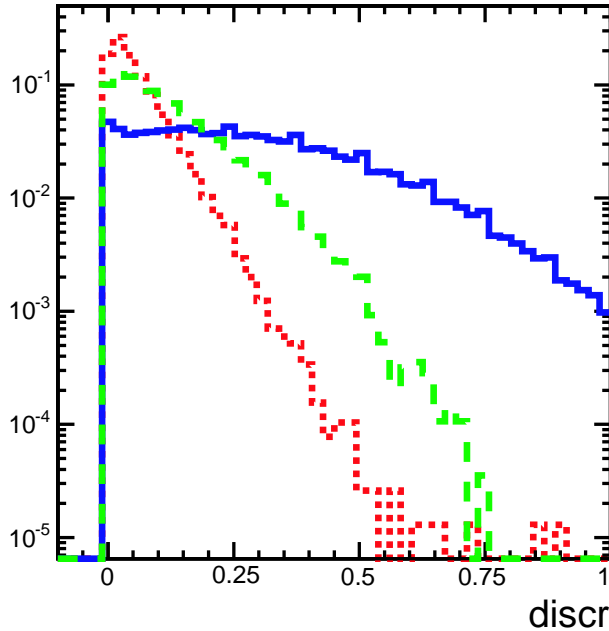


**Figure 4.17:** The distribution of discriminator values for b-jets (solid blue line), c-jets (dashed green line) and udsg-jets (dotted red line) determined in  $t\bar{t}$  events [50].

#### 4.2.6 Missing Transverse Energy Reconstruction

Due to the neutrino in the final state of semileptonic  $t\bar{t}$  decays the transverse momentum in an event is not fully balanced. The almost hermetic detector coverage can be used to sum up all visible energy. Different approaches for summation exist, summarised for example in [51]. From the imbalance of this vector sum the missing energy can be determined in x- and y-direction. The resulting observable is the missing transverse energy  $\cancel{E}_T$  (or MET), the length of the vector. It is composed of the projections in x- and y-direction ( $\cancel{E}_x$  and  $\cancel{E}_y$ ), from which the  $\phi$  direction is determinable.

Previous studies have shown that the average resolution of  $\cancel{E}_T$  is in the order of the expected amount in semileptonic  $t\bar{t}$  decays [51]. In the case when the missing transverse energy is large enough, the observable retains some information. For  $t\bar{t}$  decays with a neutrino in the final state a correlation between  $\cancel{E}_T$  and the signal neutrino exists, especially for large values of  $\cancel{E}_T$ . In figure 4.18 the two determined resolutions for  $\cancel{E}_T$  and its  $\phi$  are shown. The value of  $\cancel{E}_T$  itself holds a little information. Especially at low values of  $\cancel{E}_T$  the uncertainty is very large. The angular information is already usable for relatively low values of  $\cancel{E}_T$ .

The analytical fit to determine the resolution yields:

$$\begin{aligned}\sigma_{\cancel{E}_T}(\cancel{E}_T) &= 1.14 \cdot \exp(-2.16 \cdot 10^{-3} \cancel{E}_T [\text{GeV}]) + 0.258 \\ \sigma_{\phi}(\cancel{E}_T) &= 1.35 \cdot 10^{-3} (\cancel{E}_T [\text{GeV}])^2 + 0.137 \cancel{E}_T [\text{GeV}] + 1.454\end{aligned}$$

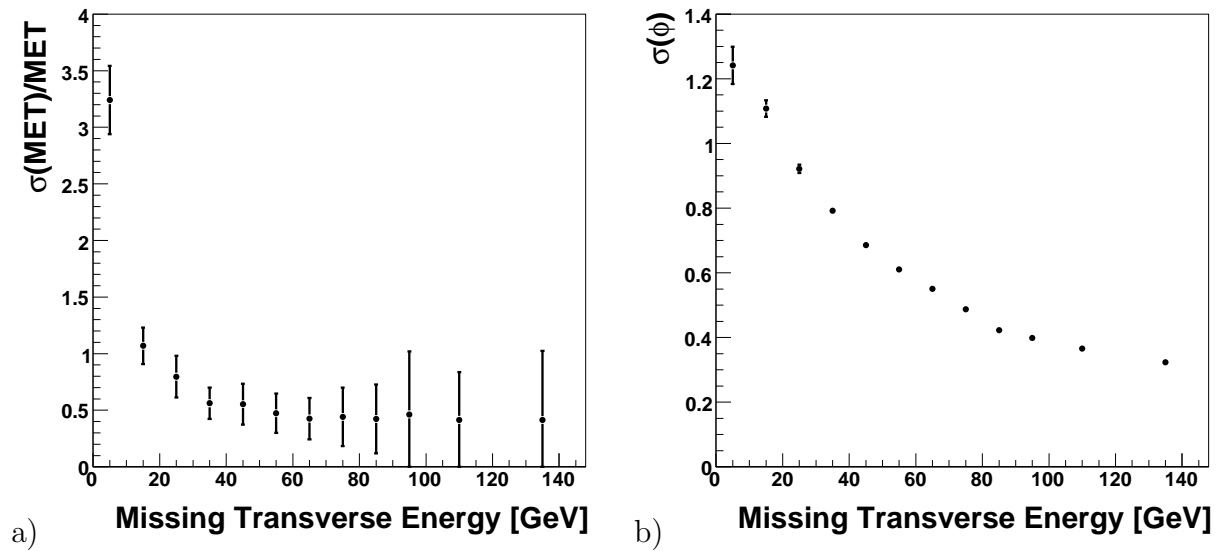


**Figure 4.18:** The  $\phi$  and missing  $E_T$  resolutions of the neutrino from measuring the missing  $E_T$  in the event. Both values depend dominantly on the missing  $E_T$  value. a) shows the relative  $\cancel{E}_T$  resolution, b) the  $\phi$  resolution.



# Chapter 5

## Event Selection and Interpretation

The event selection is divided into two steps. The first step mainly reduces the number of events by a large factor to deal with manageable amounts of data. It also ensures that all particles needed for a reconstruction as semileptonic  $t\bar{t}$  decay are present in every event. This preselection uses only directly accessible information that needs little or no additional computation. More time-consuming selection methods are applied only on a much smaller data sample in a second step.

In this analysis two different signal channels are investigated:

- semileptonic  $t\bar{t}$  decays into  $\mu + jets$  (*muon channel*),
- semileptonic  $t\bar{t}$  decays into  $e + jets$  (*electron channel*).

In figure 5.1 an exemplary event display is shown of a semileptonic  $t\bar{t}$  decay with a muon in the final state. An example of an event display in the electron channel is shown in figure 5.2. In both the lepton can be identified, as well as the minimum of four jets, indicated by large Hcal tower energies.

The major background processes considered here are  $W/Z + jets$ , QCD multi-jet production and other  $t\bar{t}$  decays. Main data samples were produced for the CSA07 [52]. For this the event numbers for an integrated luminosity of  $1\text{fb}^{-1}$  were fully simulated in  $t\bar{t}$ . Almost the full statistics for the same luminosity were simulated for  $W/Z + jets$ . The QCD background was simulated with differing equivalents of luminosities in bins of  $\hat{p}_T$ . For the combination to the target luminosity the events in these ranges are scaled accordingly. The actual scale factors for the QCD events range from several hundred thousands for the lowest  $\hat{p}_T$  bins to less than one for the highest ones.

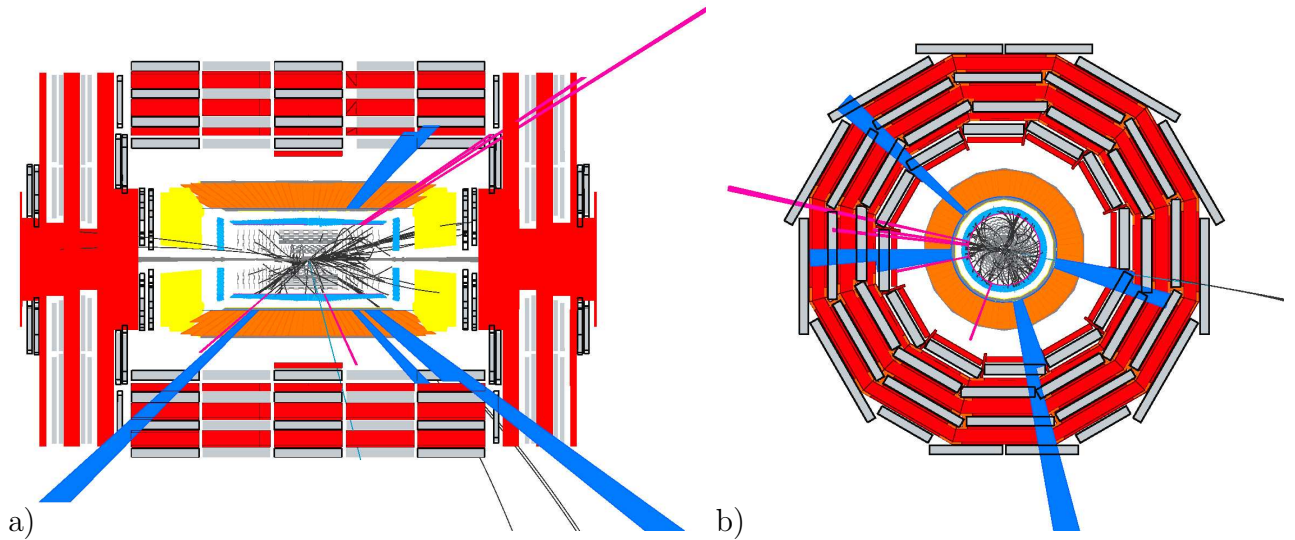


**Figure 5.1:** An event display of a  $t\bar{t} \rightarrow \mu + jets$  event, a) in  $rz$  and b) in  $r\phi$ . Hcal towers are blue, Ecal clusters pink and tracks are black lines; the size indicates the (transverse) energy or momentum. The muon is shown as a blue line, pointing downward in the  $rz$  plot and to the right in the  $r\phi$  plot.

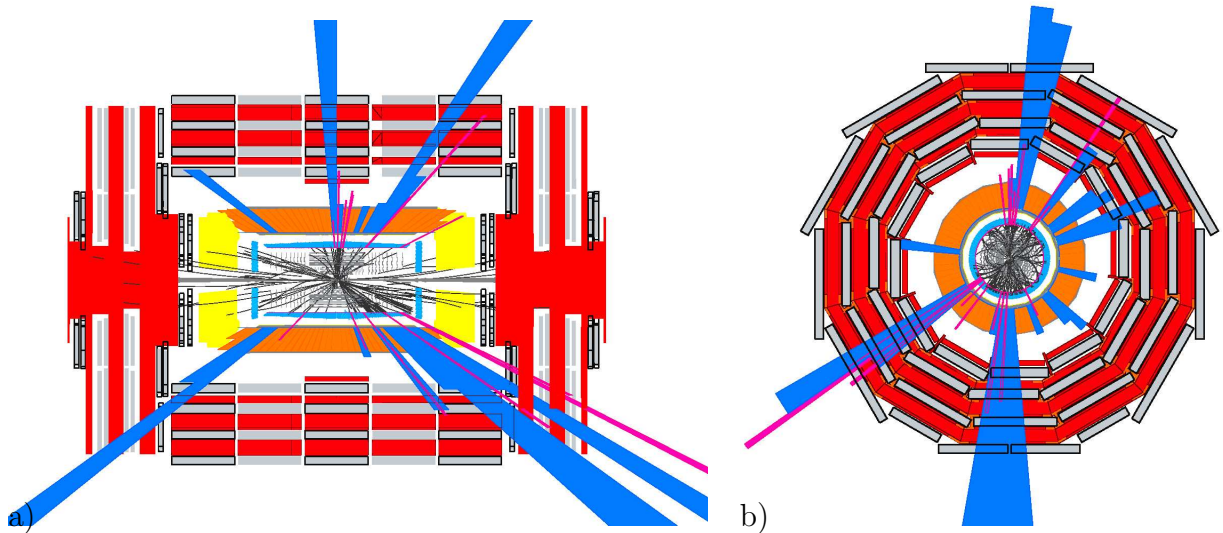


**Figure 5.2:** A  $t\bar{t} \rightarrow e + jets$  event, a) in  $rz$  and b) in  $r\phi$ . The electron is measured in the endcap as a separated large Ecal cluster (pink colour) in the lower right corner in the  $rz$  plot and the lower left corner in the  $r\phi$  plot.

## 5.1 Preselection step

To allow the full event reconstruction at least four jets and one lepton (either electron or muon) must be present in the event. Cut values are defined for the lepton and the jets.

### 5.1.1 Lepton Selection

The presence of a high- $p_T$  lepton is the strongest handle on the selection of semileptonic top pair events. As described before the lepton is demanded to be isolated. The two samples vary only in the selection of the lepton.

For the muon selection exactly one isolated muon with  $p_T \geq 30 \text{ GeV}$  in  $|\eta| < 2.4$  is required and no other isolated lepton. A muon is considered to be isolated when it fulfils the requirements (see section 4.2.1):

$$\begin{aligned} \sum_{\text{tracks}} p_T \Big|_{\Delta R \leq 0.3} &\in [0.9, 1.1] \cdot p_{T,\mu} \quad \text{and} \\ \sum_{\text{calotowers}} E_T \Big|_{\Delta R \leq 0.25} &\in [0.05, 0.2] \cdot p_{T,\mu}. \end{aligned}$$

In the electron selection an event contains exactly one isolated electron with  $p_T \geq 30 \text{ GeV}$  and  $|\eta| < 2.4$ . Other than this electron no other isolated lepton is allowed in the event. An isolated electron has the properties (see section 4.2.3):

$$\begin{aligned} \sum_{\text{tracks}} p_T \Big|_{\Delta R \leq 0.3} &\leq 1.05 \cdot p_{T,e} \quad \text{and} \\ \sum_{\text{calotowers}} E_T \Big|_{\Delta R \leq 0.3} &\leq 1.08 \cdot p_{T,e}. \end{aligned}$$

Figure 5.3 shows the numbers of isolated muons and electrons for the initial event sample of  $1 \text{ fb}^{-1}$ . The event numbers for the different channels before and after the cuts are summarised in table 5.1.

A minimal value of  $30 \text{ GeV}$  is well above the trigger threshold of about  $20 \text{ GeV}$ , the resulting trigger efficiency is about 100%.

The lepton selection is most efficient in reducing the very large backgrounds from QCD jet-production and the hadronic  $t\bar{t}$  decays. In addition also  $t\bar{t}$  decays that include more than one lepton in the final state are reduced. Because of the very similar signature of at least one isolated high- $p_T$  lepton, the number of  $W/Z + jets$  events is not reduced much.

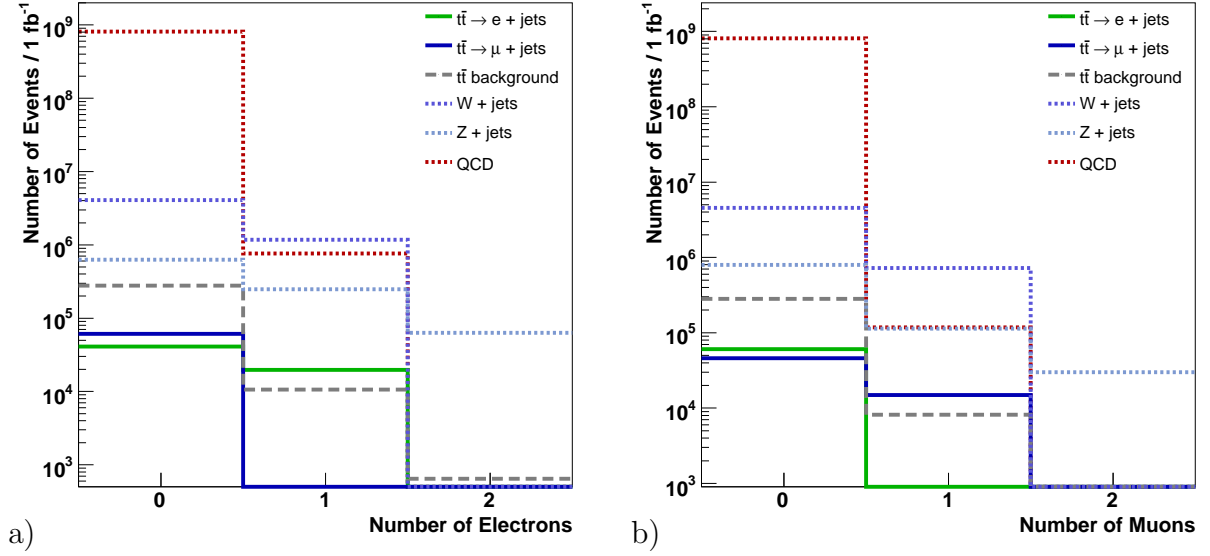


**Figure 5.3:** The number of isolated leptons with  $p_T \geq 30$  GeV before applying any further cut for the different event types. a) The number of isolated electrons, b) the number of isolated muons. Both leptons are required to have  $|\eta| \leq 2.4$ . In both cases 'background' denotes those  $t\bar{t}$  decays that are not the two considered semileptonic signal channels.

### 5.1.2 Jet Selection

The jet selection is expressed in a cut on the number of jets above a given  $E_T$  threshold. The  $E_T$  threshold is relevant in two ways. As discussed in the description of the jet

	Initial	Muon Cut	Efficiency	Electron Cut	Efficiency
$t\bar{t} \rightarrow e + jets$	60828	4	$6.6 \cdot 10^{-5}$	17984	0.296
$t\bar{t} \rightarrow \mu + jets$	60926	14968	0.246	9	$1.46 \cdot 10^{-4}$
$t\bar{t} \rightarrow \tau + jets$	60692	899	0.015	834	0.013
$t\bar{t} \rightarrow$ dileptonic	46035	6378	0.139	7841	0.170
$t\bar{t} \rightarrow$ hadronic	183384	12	$6.5 \cdot 10^{-5}$	23	$1.2 \cdot 10^{-4}$
$W + jets$	5266k	723527	0.137	925085	0.176
$Z + jets$	938k	113163	0.121	220177	0.235
$QCD$	811326k	118222	$1.46 \cdot 10^{-4}$	72578	$6.6 \cdot 10^{-5}$

**Table 5.1:** The efficiencies of the lepton preselection cuts and the event numbers for a luminosity of  $1 \text{ fb}^{-1}$ .

reconstruction and energy correction (section 4.2.4) the jet energy is only well defined for an  $E_T$  well above 20 GeV. Figure 5.4 shows the energies of the four highest energetic jets in an event.

The greatest potential to distinguish the different processes lies in the third and fourth highest energies. In order to enable a high selection efficiency a relatively low cut on these two energies is chosen. The jet selection is independent of the lepton selection. An event that passes the jet preselection is demanded to have

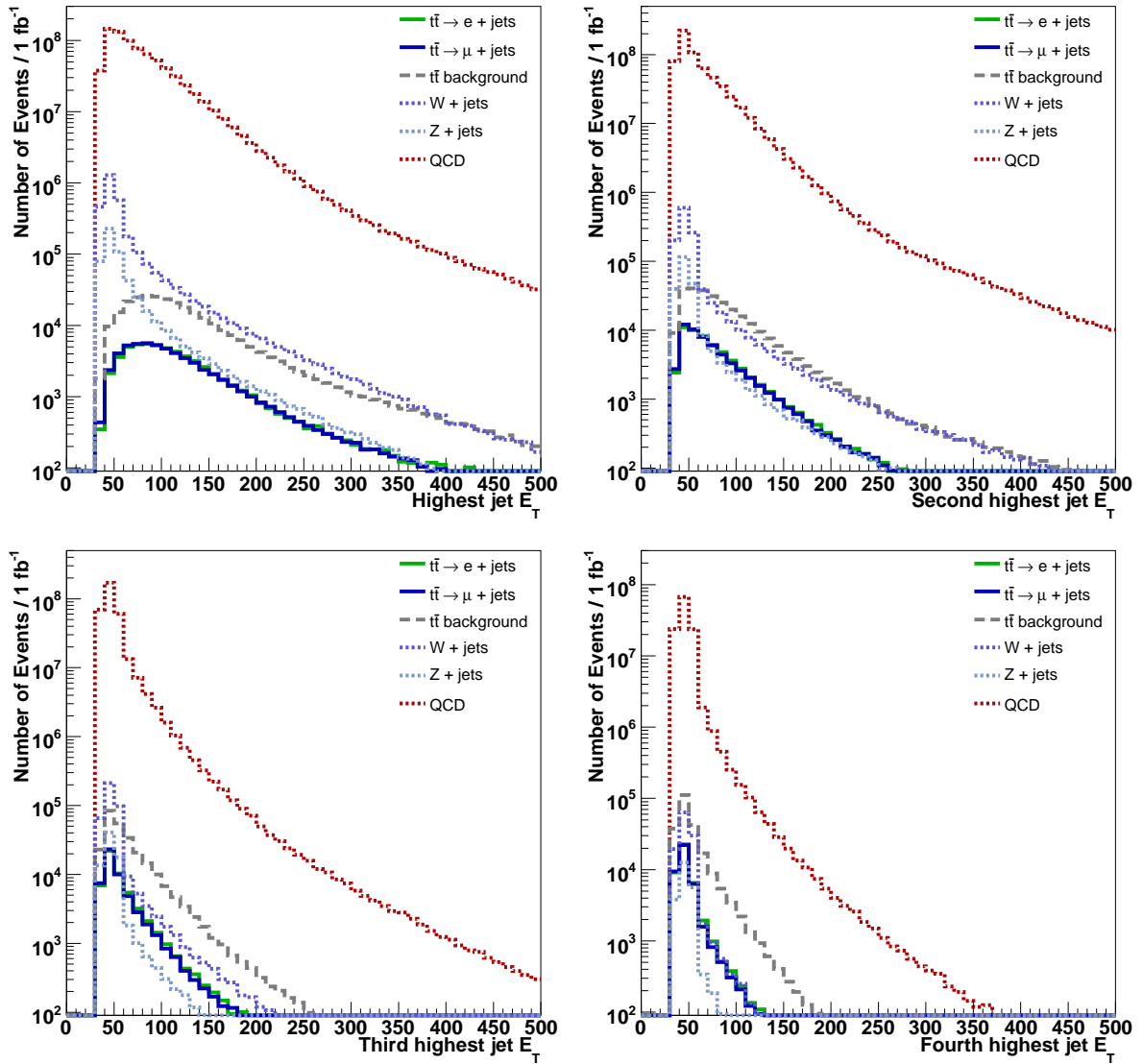


**Figure 5.4:** The distributions of the transverse jet energies for the four leading jets for different simulated processes at a target luminosity of  $1\text{fb}^{-1}$ .

	Before	Jet Cut	Efficiency
$t\bar{t} \rightarrow e + jets$	60828	42035	0.691
$t\bar{t} \rightarrow \mu + jets$	60926	40826	0.670
$t\bar{t} \rightarrow \tau + jets$	60692	45225	0.745
$t\bar{t} \rightarrow$ dileptonic	46035	17469	0.379
$t\bar{t} \rightarrow$ hadronic	183384	166597	0.908
$W + jets$	5266k	108194	0.021
$Z + jets$	938k	21003	0.022
$QCD$	811326k	111947k	0.139

**Table 5.2:** The jet selection efficiencies and event numbers for a luminosity of  $1\text{fb}^{-1}$ .

- at least 3 jets with  $E_T \geq 40$  GeV and
- at least 4 jets with  $E_T \geq 30$  GeV.

In table 5.2 the event numbers and efficiencies before and after the jet preselection cut are summarised. This cut is rather inefficient against hadronic backgrounds, both from QCD and particularly from the hadronic top pair decays. But it is very effective in reducing the leptonic vector boson decays and dileptonic  $t\bar{t}$  decays.

In qualitative terms this jet preselection cut can be motivated from the model on parton level. In semileptonic  $t\bar{t}$  always four quarks are present in the final state, resulting in four reconstructed jets. Due to the high mass of the top quark most jets have high energy and therefore in most cases also large transverse energy. QCD background is dominated by di-jet events. Additional hard parton radiations are suppressed by factors of  $\alpha_s$ . The same suppression is intrinsically true for the jet multiplicity in  $W/Z + jets$  events. Semileptonic top pair decays exhibit a different property, in any decay at least four jets are present.

### 5.1.3 Preselection Summary

The application of both selection cuts combines the rejection power of hadronic and partially leptonic background sources. Figure 5.5 shows the distributions before the application of the cut on the variable that is shown, but with the other cut already applied (N-1 plot) for the two cuts of the electron and the muon preselection.

The preselection is summarised in numbers in table 5.1.3. For the muon channel a signal to background ratio  $S_\mu : B = 1 : 2$ , for the electron channel it is slightly worse with  $S_e : B = 1 : 2.3$ .

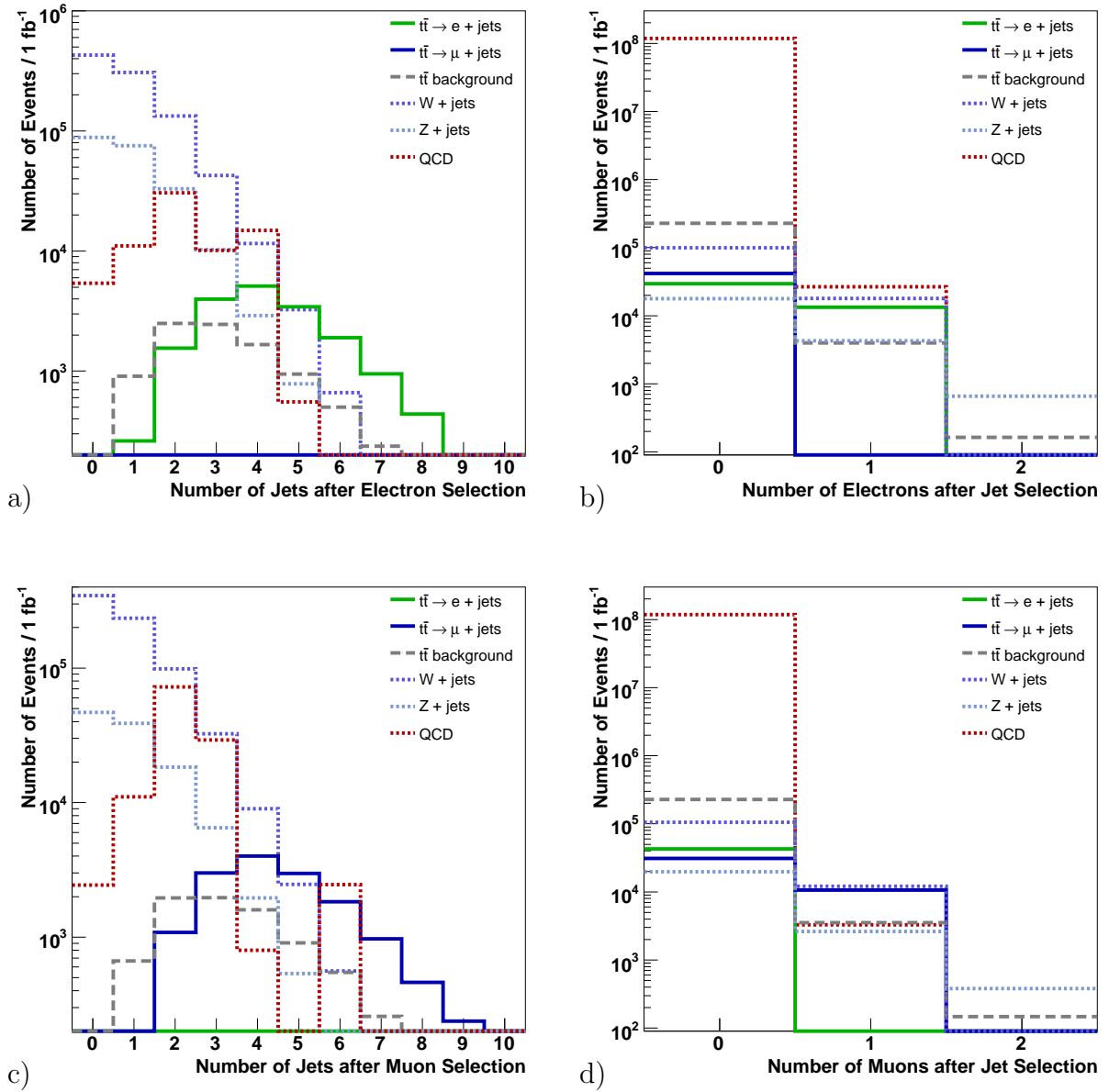


**Figure 5.5:** The N-1 distributions for the electron (a) and b) ) and the muon(c) and d) ) preselection. a) and c) show the number of jets (above the  $E_T$  threshold) in events with exactly one isolated lepton. b) and d) show the number of isolated leptons with  $p_T \geq 30$  GeV with the condition that at least four jets above the preselection cut are present.

	Muon Preselection	Efficiency	Electron Preselection	Efficiency
$t\bar{t} \rightarrow e + jets$	1	$1.6 \cdot 10^{-5}$	11861	0.195
$t\bar{t} \rightarrow \mu + jets$	10422	0.171	6	$9.7 \cdot 10^{-5}$
$t\bar{t} \rightarrow \tau + jets$	640	0.011	533	$9 \cdot 10^{-3}$
$t\bar{t} \rightarrow$ dileptonic	2724	0.059	2579	0.056
$t\bar{t} \rightarrow$ hadronic	8	$4.3 \cdot 10^{-5}$	18	$9.8 \cdot 10^{-5}$
$W + jets$	10975	$2.1 \cdot 10^{-3}$	14310	$2.7 \cdot 10^{-3}$
$Z + jets$	2403	$2.6 \cdot 10^{-3}$	3770	$4.0 \cdot 10^{-3}$
$QCD$	3286	$4.1 \cdot 10^{-6}$	6340	$7.8 \cdot 10^{-6}$

**Table 5.3:** Expected event numbers and efficiencies after the cuts for the muon and the electron preselection for an integrated luminosity of  $1\text{fb}^{-1}$ .

## 5.2 Selection

For further selection three kinds of observables are used, which are explained in more detail. Event shape variables are the most simple, based on direct calculations. Also used is the discriminator value of b-tagging, which exploits the occurrence of two b-quarks in the final state. The third kind of observables is based on the reconstruction of the event with a kinematic fit. For example can be taken from the kinematic fit how well the top quark and  $W$  boson masses can be simultaneously reconstructed in an event.

In the following figures the QCD multi-jet background is not shown anymore, although in the tables the numbers are still given. The reason is a fundamental technical problem that all current analyses suffer from. The tremendously large cross section of inclusive QCD processes makes it virtually impossible to simulate even an approximately equivalent number of events for an integrated luminosity of  $1\text{fb}^{-1}$ . Although a full sample does not necessarily need to be generated, still considerably higher statistics are needed than currently available.

The available simulated events are generated in sub-samples of  $\hat{p}_T$  bins. The events of those bins are combined to a common integrated luminosity by scaling them accordingly with respect to their initial luminosity. No problems are encountered when sufficient unscaled event numbers are considered. But with effective selection methods this leads to unphysical distributions, single events remain that contribute with weights of more than one thousand. The integral number itself is the best approximation possible for now.

It is not expected that the fundamental impossibility of the simulation of large enough statistics will change, even after the start of data taking. The general agreement on the treatment of this problem is the extraction of this background from data.

## Event Shape Variables

Event shape variables are commonly used at colliders where the centre-of-mass frame is equal to the laboratory frame. Analysis of hadron collider data enforces the use of longitudinal boost-invariant observables for event classification

The  $E_T$  spectra in figure 5.4 show, that the transverse energy spectrum of jets in  $t\bar{t}$  events is harder than for the vector boson backgrounds. Due to the higher mass of the produced particles, the boost is smaller, leading to more central jets in  $t\bar{t}$  events than for the other backgrounds. Instead of defining explicit cuts on the ordered jet  $E_T$  values it is possible to use event shape variables.

A good inclusive measure of the  $E_T$  distribution is the scalar sum of transverse jet energies  $Ht$ . To be more sensitive to the hard process only the four highest transverse energies are considered, where  $Ht$  is defined for an  $E_T$  ordered list from high to low values:

$$Ht = \sum_{i=1}^4 E_{T,jeti}.$$

In addition to the transverse energy sum the *centrality*  $C$  is a measure of the  $\eta$  distribution of energy in the detector, where the centrality is defined as the ratio of the transverse energy sum ( $Ht$ ) and the total energy:

$$C = \frac{Ht}{\sum_{i=1}^4 E_{jet_i}}.$$

Both observables can be used to distinguish between the leptonic vector boson decays and signal events.  $W/Z$  bosons decay preferentially into the forward direction, causing an asymmetric centrality distribution to lower values. Semileptonic top pair decays are more evenly distributed, leading to a symmetric centrality distribution centered around a higher value.

Figure 5.6 shows the distributions of  $Ht$  and centrality for the events that passed the preselection.

## Tagging of b-jets

B-jets can be distinguished from other jet flavours based on the discriminator value (see section 4.2.5). In the decay of  $t\bar{t}$  events there are always two b-jets present, leading to a high probability for two large b-tag values. The b-tagging algorithm described in 4.2.5 is used here. In figure 5.7 the highest and the second highest b-tag values for the preselected events are shown.

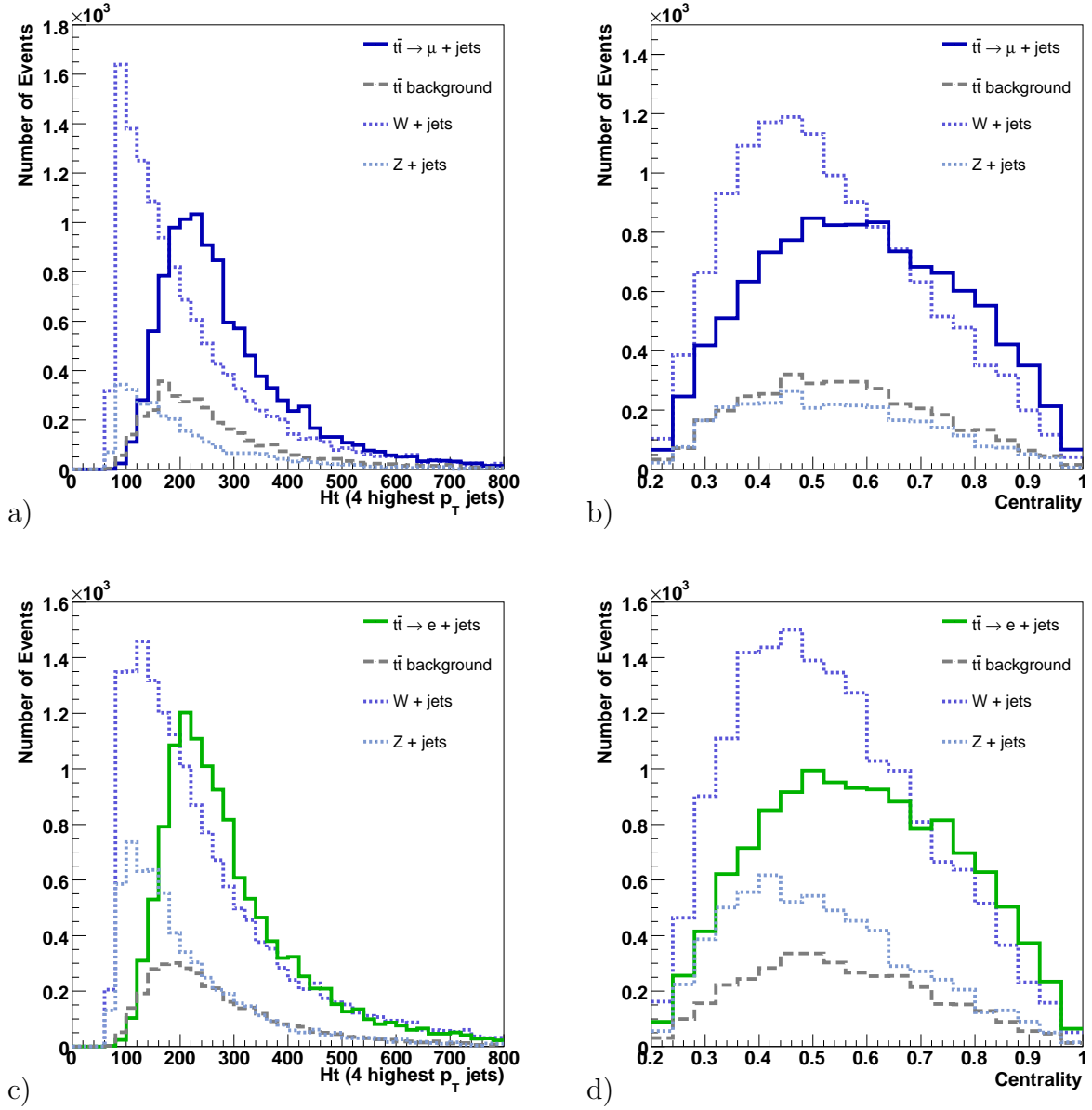


**Figure 5.6:** Event shape variables for the events after the preselection. a) and b) for the muon preselection, c) and d) for the electron preselection. a) and c) show  $Ht$ , the scalar sum of the four highest jet  $E_T$  values. b) and d) show the centrality.

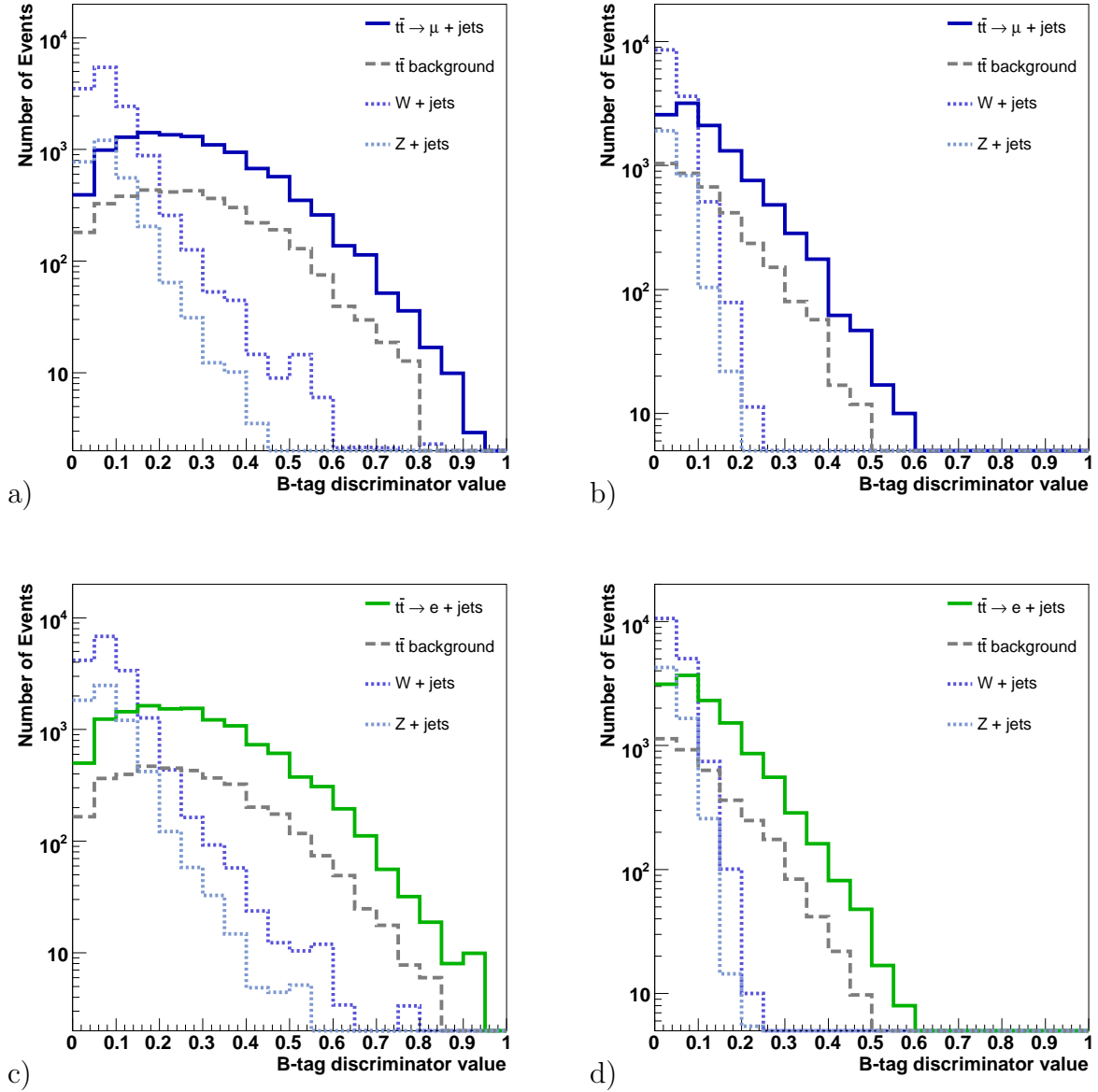


**Figure 5.7:** The discriminator values of the *track probability tag* for the remaining events of the preselection. a) and b) for the muon preselection, c) and d) for the electron preselection. a) and c) The highest discriminator value of all jets with  $p_T \geq 30$  GeV. b) and d) the second highest discriminator value for the same jets.

## Kinematic Fitting

The presence of a high  $p_T$  lepton and four high  $p_T$  jets allows a hypothetical interpretation of the event as semileptonic  $t\bar{t}$  decay. A determination to which degree a reconstructed event is signal-like can be derived from a kinematic fit.

A kinematic fit is a least square fit with external constraints, based on the kinematical content of the event. Input to the fit are the measured particles and their resolutions: the jets, the lepton and the missing energy. In qualitative terms the fit varies the measured quantities like angles and transverse energy within their experimental resolution. In an iterative procedure the solution is found which fulfils the applied constraints best. It may be that the fit does not converge, which means that no solution could be found within the allowed number of iterations. The resulting  $\chi^2$  value of the fit can be used as basis for the computation of a probability of an event to fulfil the imposed kinematic hypotheses. A full mathematical reference can be found in [53], a short mathematical description is given in appendix C.

A semileptonic  $t\bar{t}$  decay can be characterised by the possibility to reconstruct the following particles simultaneously in a single event:

- one completely hadronically decaying top,
- one leptonically decaying top (shorthand for the decay chain with a leptonically decaying  $W$  boson),
- one hadronically decaying  $W$  boson and
- one leptonically decaying  $W$  boson.

These requirements are formulated as mass constraints. This means for example that the invariant mass of two jets must be the  $W$  boson mass and the total invariant mass with a third jet is supposed to be the top quark mass. In this example the first two jets would be the jets from the hadronic  $W$  decay and the third jet would be the b-jet from the hadronic top quark decay.

A fundamental difference to the other classes of selection variables is that for each given event several possible combinations exist. This results in a large number of fits for each event, in particular one fit for every combination of particle assignments.

The lepton and the neutrino are unambiguous in an event, in the sense that exactly one of each particles is reconstructed. Either the electron or muon are very well reconstructed in their complete four-vector. The neutrino is less straightforward, since it is underdetermined in its reconstruction from the missing transverse energy (see section 4.2.6). At

least four jets above the  $E_T$  threshold are reconstructed in an event. This means that if exactly four reconstructed jets are present 12 different assignments to the hadronic top pair decay particles are possible. For each of these assignments a fit is performed. In case there are at least five jets reconstructed above the  $E_T$  threshold the full combinatorics would already mount up to 60. The actual number of fits can be slightly reduced to decrease the needed computation time. B-jets tend to be of higher  $E_T$  than the jets resulting from the hadronic  $W$  decay. Therefore the b-jet candidates are taken from the four highest  $E_T$  jets and only the  $W$ -jet candidates are taken from the first five.

The fit of the full event with all constraints is very time-consuming. A reduction of the number of fits is therefore advisable. Most combinations are random assignments of the measured particles. The chance to fulfil the mass constraint on both sides at the same time is rather small for most of these combinations. The needed computation for each event can be severely reduced, if this is taken into account. On each combination a sequence of three fits is performed, where the execution of each depends on the convergence of the fit before:

1. a fit of the **leptonically decaying top quark**;  
with mass constraints on the top quark and the leptonically decaying  $W$ ;
2. a fit of the **fully hadronically decaying top quark**;  
with mass constraints on the top quark and the hadronically decaying  $W$ ;
3. the **full event fit** of all particles with all mass constraints.

The simplest fit is the leptonically decaying top due to the relative large uncertainty of the neutrino reconstruction. If this fit converges the complementary particles are used to fit the hadronically decaying top side. Only if these faster and simpler fits converge the complete kinematic fit is executed. The time needed for the two simpler fits is negligible compared to the fit of the full event.

If no combination yields a convergence of all fits, the event is rejected. The combination with the smallest  $\chi^2$  sum is considered the best fit. This best fit is also taken as the best reconstruction of the event.

From the result of this best fit different properties can be extracted that are usable for the selection. The smallest  $\chi^2$  value is used to compute a probability that quantifies how consistent the fit result is with the implied constraints. Under certain circumstances this resulting distribution can be interpreted as a probability. For ease of notation this is simply referred to as  $\chi^2$  *fit probability*. The mathematical definition is given in appendix C.

Figure 5.8 shows the most distinguishing probability distributions for the hadronic side and the full event fit.

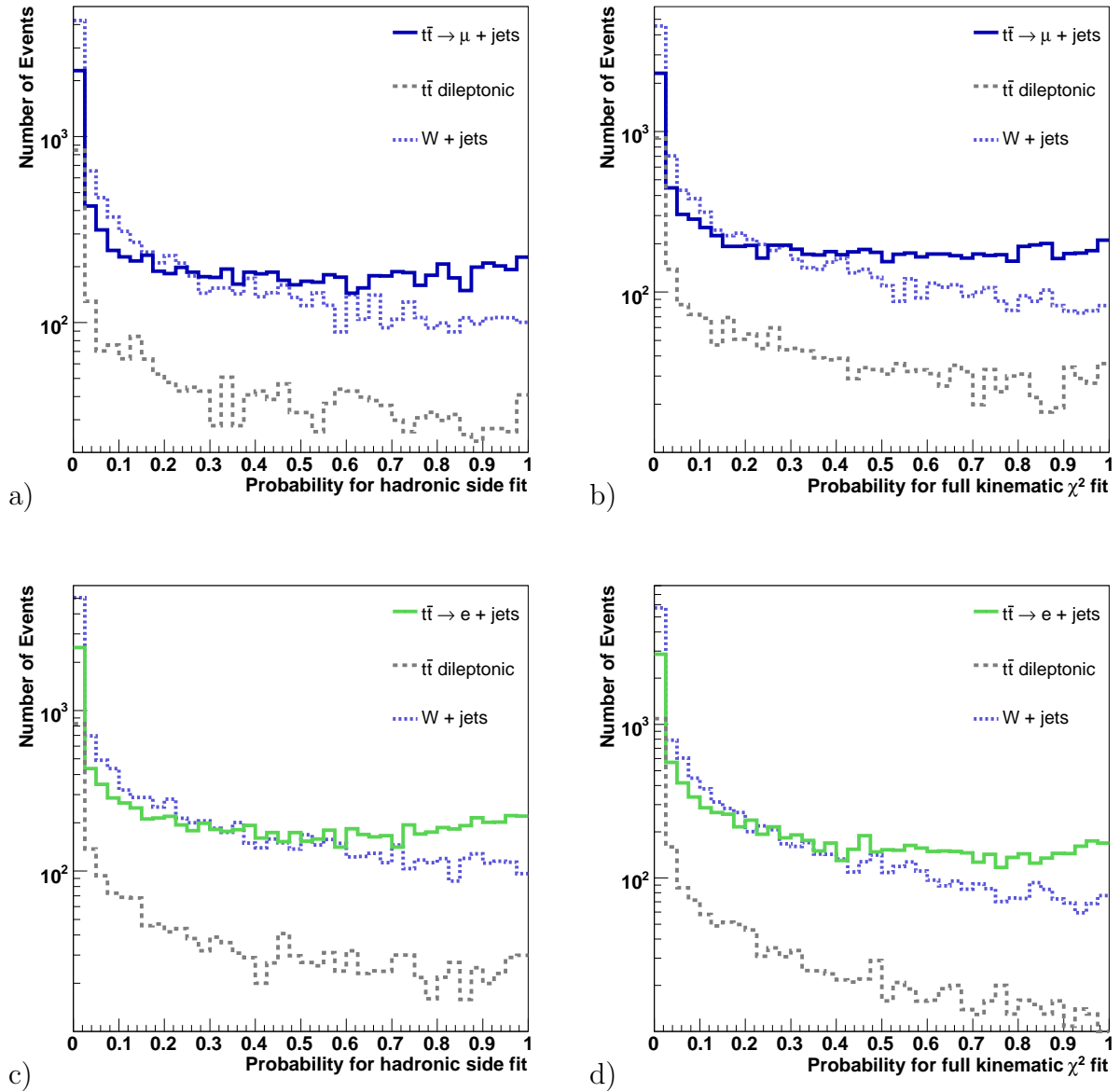


**Figure 5.8:** The probability distributions of converged fits. a) and c) Only for the hadronic side and b) and d) for the full event. a) and b) show the events for the muon preselection, c) and d) for the electron preselection.

## Selection Methods

Each of the variables show significant differences between signal and background processes. Here two methods of using these variables are shown and compared. For this comparison a target efficiency of 10 % for the signal is chosen.

The most straightforward method to use the differences is to simply cut on each of the variables. It is simple and robust, but not the most efficient method in terms of background rejection power. To exploit the full distinction possibility a multivariate approach is better suited. A neural network is implemented for this purpose.

### 5.2.1 Cut-based Selection

For the cut-based selection only observables are used, that can be separated by a linear cut. An example for this is the  $Ht$ , as shown in figure 5.6a). The centrality exhibits an opposite behaviour by showing a difference in the shape of the distribution, as shown in figure 5.6b). No clear linear distinction is possible between signal and background.

Best suited for the cut approach are the  $Ht$ , the highest b-tag discriminator value and the fit probability of the full event. The complete and the N-1 distributions of  $Ht$  are shown in figure 5.9. Figure 5.10 shows the distributions of the highest b-tag value. Figure 5.11 depicts the fit probability of the full event. The cut values for a selection efficiency of 10 % are summarised in table 5.2.1. The cut efficiencies and resulting event numbers for an integrated luminosity of  $1\text{fb}^{-1}$  are given in table 5.2.1.

Observable	Selection Cut
$Ht$ [GeV]	$\geq 150$
Highest b-tag	$\geq 0.4$
Probability of full event fit	$\geq 0.01$

**Table 5.4:** The cut values for the cut-based event selection for both muon and electron channel.

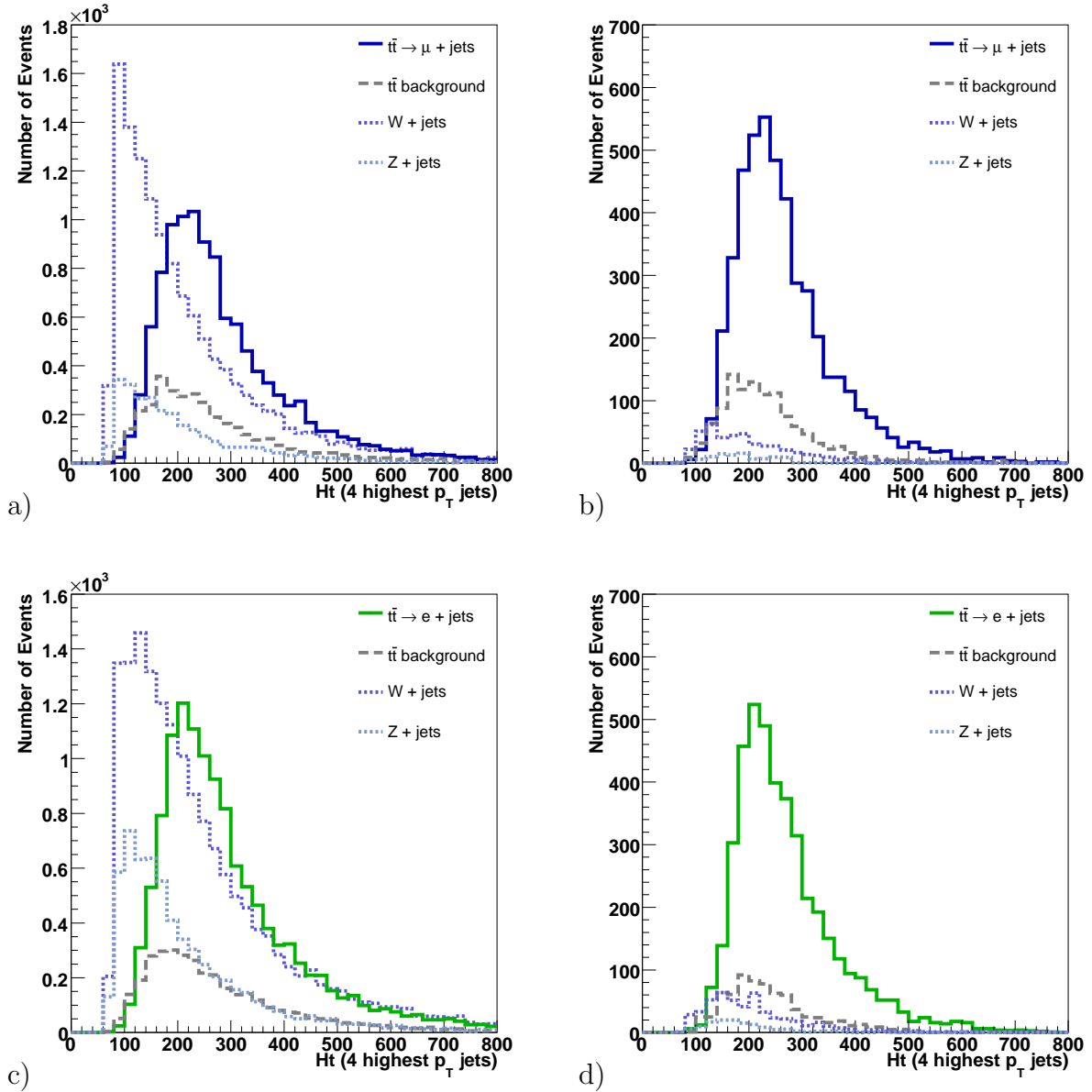


**Figure 5.9:**  $H_t$  distributions for the cut-based selection of the muon channel in a) and b), for the electron channel in c) and d). a) and c) before the application of any other cut. In b) and d) as N-1 distribution.

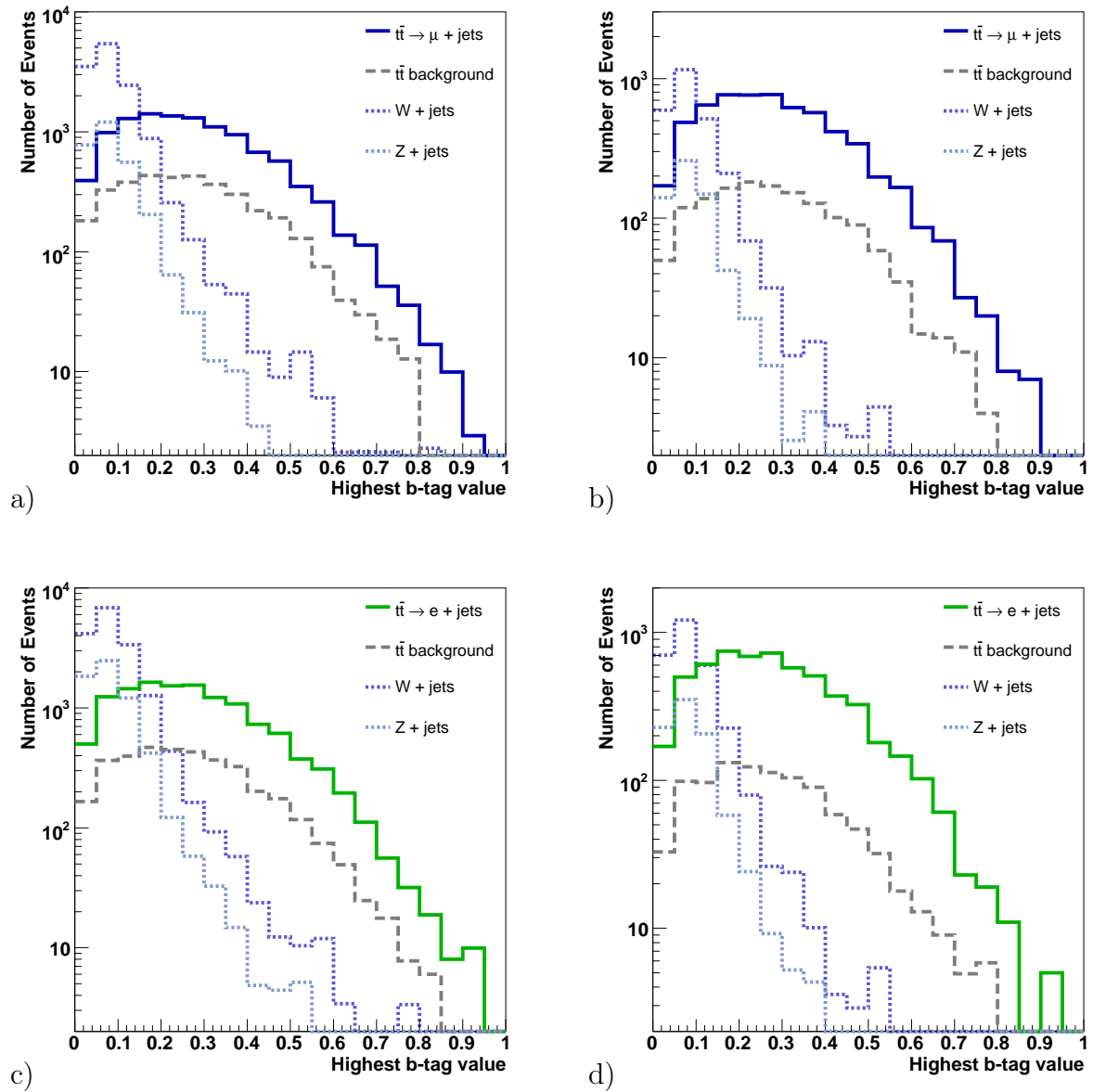


**Figure 5.10:** B-tag discriminator values for the cut-based selection of the muon channel in a) and b), for the electron channel in c) and d). Shown are the distributions a) and c) before any other cut, and as N-1 distribution in b) and d).

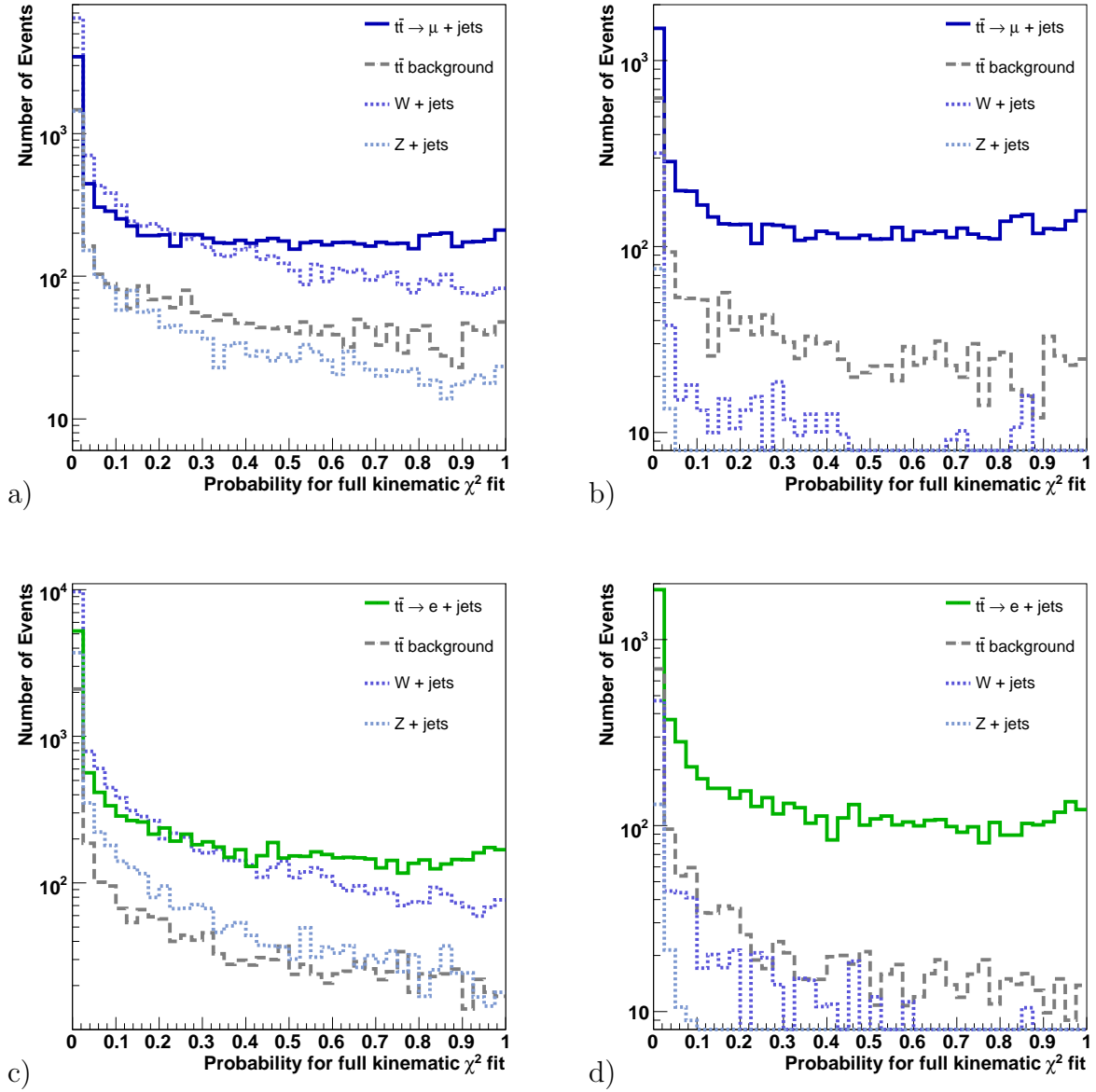


**Figure 5.11:** Fit probabilities for the full event for the cut-based selection. For the muons in a) and b), for the electron selection in c) and d). In a) and c) the distributions are shown before any cuts, in b) and d) the N-1 distribution.

	Muon Selection	Efficiency	Electron Selection	Efficiency
$t\bar{t} \rightarrow e + jets$	1	$1.6 \cdot 10^{-5}$	6159	0.100
$t\bar{t} \rightarrow \mu + jets$	6054	0.100	2	$3.3 \cdot 10^{-5}$
$t\bar{t} \rightarrow \tau + jets$	379	$6 \cdot 10^{-3}$	262	$4.3 \cdot 10^{-3}$
$t\bar{t} \rightarrow$ dileptonic	1153	0.025	941	0.020
$t\bar{t} \rightarrow$ hadronic	3	$1.6 \cdot 10^{-5}$	6	$3.3 \cdot 10^{-5}$
$W + jets$	641	$1.2 \cdot 10^{-4}$	834	$1.6 \cdot 10^{-4}$
$Z + jets$	167	$1.7 \cdot 10^{-4}$	253	$2.7 \cdot 10^{-4}$
$QCD$	127	$1.6 \cdot 10^{-7}$	87	$1.1 \cdot 10^{-7}$

**Table 5.5:** The efficiencies and event numbers for an integrated luminosity of  $1\text{fb}^{-1}$  for the cut-based muon and electron selection.

### 5.2.2 Neural Network Selection

The need for feature-based classification or pattern recognition is a recurring task not only in particle physics. Linear separation (like the cut-based method) has the main advantage of being comprehensible. But there are two prominent shortcomings of the cut-based approach. Firstly, it neglects correlations between observables. Secondly, it is limited to variables that can be separated sufficiently well by a linear cut, which excludes for example the centrality shown in figure 5.6b).

A complementary approach that avoids some of the limitations is chosen here in form of an *Artificial Neural Network*. Neural networks can be used in pattern recognition as needed for the selection, incorporating both correlations and non-linearities. An extensive reference can be found in [54].

For the selection a feed-forward neural network is employed, trained with supervised learning using backpropagation with a momentum term. Eight input nodes are used, the observables are described below. One hidden layer with 15 nodes yields good performance, showing no significant indication of over-training. Two output nodes are used to leave an additional degree of freedom to describe the signal-likeness and the background-likeness in independent numbers. The full technical description is given in appendix D.

Input to the network are eight observables. Three of these are already used and shown for the cut-based selection. These are the  $Ht$  value (presented in figure 5.9), the highest b-tagging value (shown in figure 5.10) and the fit probability of the full event (depicted in figure 5.11). With a neural network shape-based distinction is also possible. This enables the use of the centrality (shown in figure 5.6b)). In addition to these also the second highest b-tagging value is considered (depicted in figure 5.7).

Besides these directly distinguishing variables some additional observables are used that quantify how well the event reconstruction matches the template of a semileptonic  $t\bar{t}$  decay. The first one is the sum of the transverse jet energies of the reconstructed  $W$  boson jets. For random combinations this is an exponentially falling spectrum starting at a minimal value due to the mass constraint. For signal events it also start at the minimal value, but it peaks at a higher value and are more evenly distributed. While this is influenced by the decay kinematics (especially the boost of the top),  $W$  bosons originating from top decays have a minimal energy due to the top mass. In turn this leads on average to higher energies, and thus transverse energies.

Also two angles are taken as input values for the neural network. The opening angles between the decay products of the top quarks are usually smaller than the values for random combinations, which fulfil the mass constraints. Considered are the angles

- between the lepton and the associated b-jet from the leptonically decaying top quark and
- between the reconstructed  $W$  candidate and the corresponding b-jet from the hadronically decaying top quark.

The idea behind the use of these angles is the basic geometry of the decay in which both decays happen in separate hemispheres. This results in smaller values for the true combination, although the actual kinematics still play an important role. The three additional variables for the muon selection are shown in figure 5.12.

A central point for the employment of a neural network in favour of other multivariate techniques is the possibility to use correlated variables without distorting the result. In fact the correlations are also learned in the training process of the neural net, as they are also a feature of the observables. As an illustration the linear correlations between the input observables are shown in figure 5.13 for both channels.

The answer distribution  $A$  of the output nodes  $out_1$  and  $out_2$  of the trained neural network as the normalised ratio

$$A = \frac{out_1}{out_1 + out_2}$$

is given in figure 5.14.

In order to allow the comparison to the cut-based selection the same selection efficiency of 10% has been chosen. For the electron network this is achieved by cutting at  $A_e \geq 0.812$ , for the muon network this corresponds to  $A_\mu \geq 0.77$ .

The resulting event numbers and efficiencies are summarised in table 5.6.

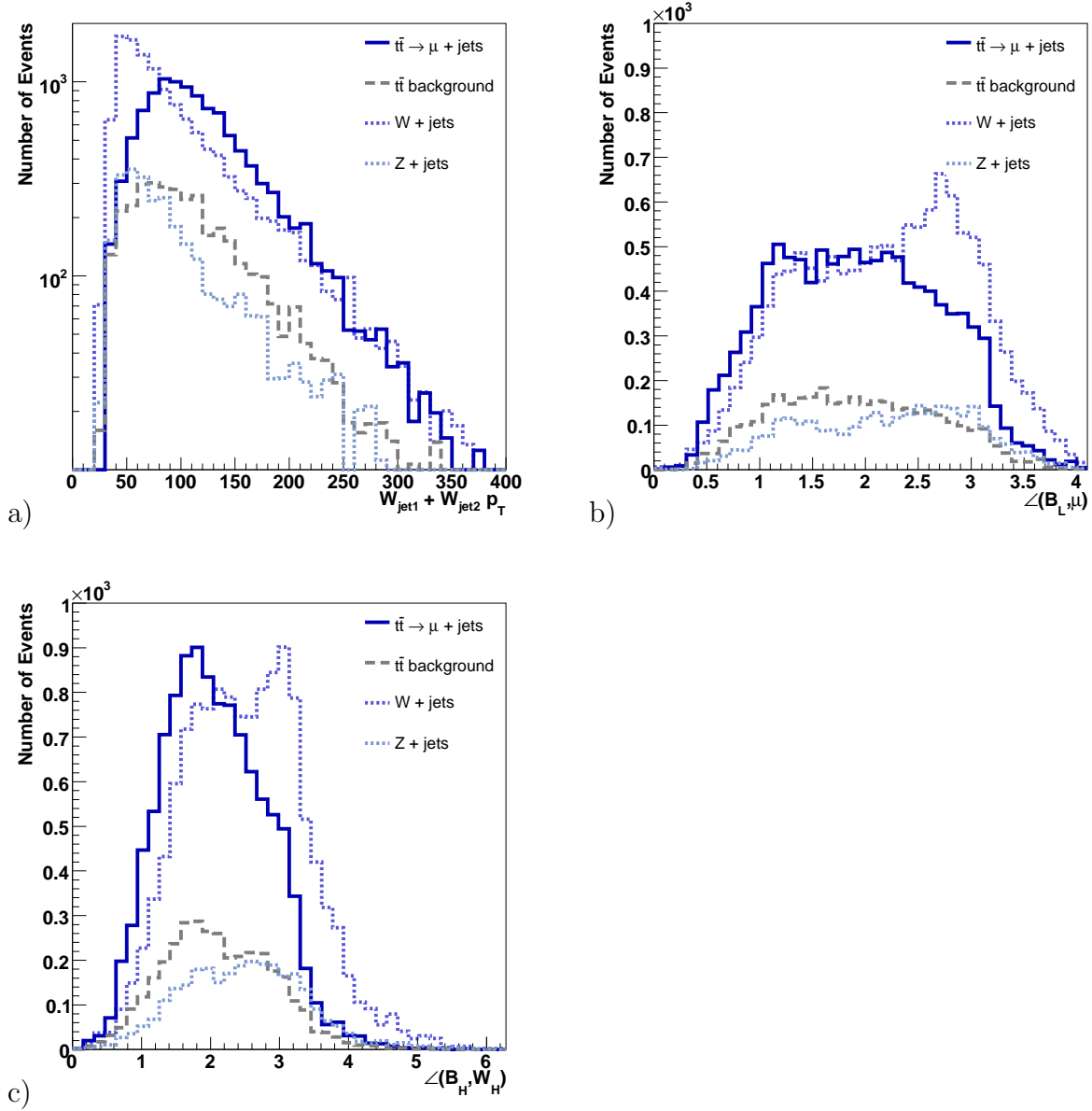


**Figure 5.12:** The three additional variables for the neural network selection that help to quantify the reconstruction quality. As an example the distributions from the muon selection are shown. a) shows the sum of the two jet  $p_T$  values from the two jets assigned to the hadronic  $W$  decay. b) depicts the opening angle between the b-jet from the leptonically decaying top quark and the lepton. c) shows the angle between the reconstructed hadronically decaying  $W$  and the associated b-jet.

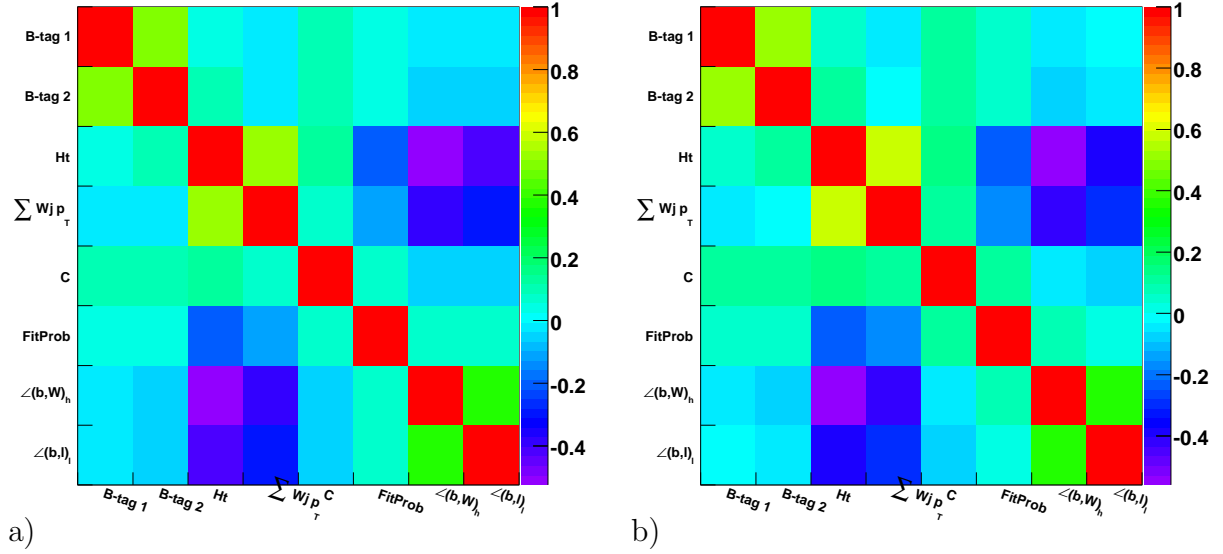


**Figure 5.13:** The correlation values of the variables used as input to the neural network. a) The values for the electron selection and b) for the muon selection.

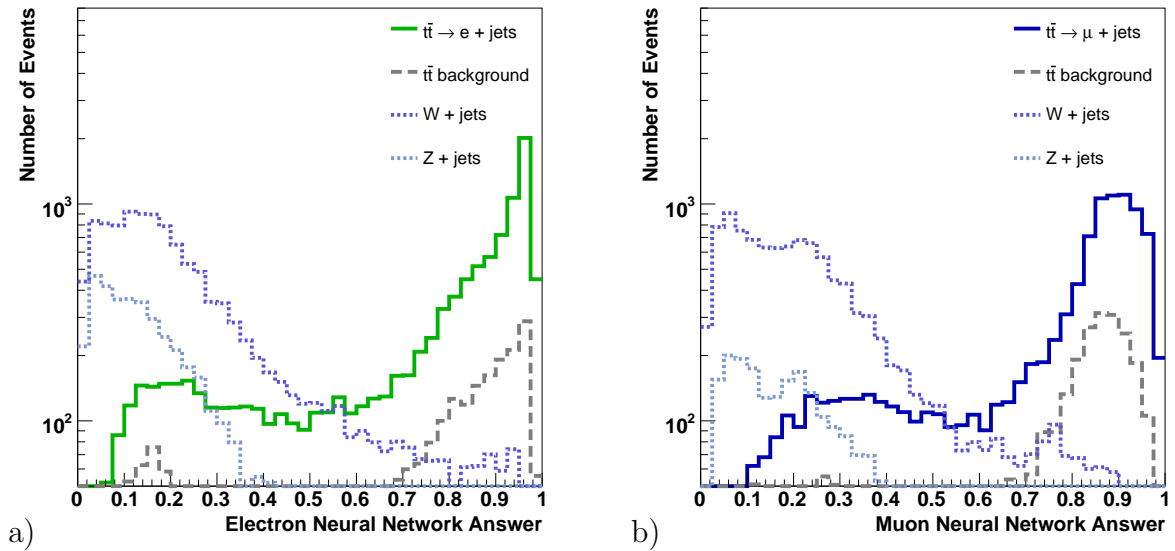


**Figure 5.14:** The neural network answers for the two trained networks. a) For the electron network and b) for the muon network. Higher values indicate the signal-likeness.

	Muon Selection	Efficiency	Electron Selection	Efficiency
$t\bar{t} \rightarrow e + jets$	1	$1.6 \cdot 10^{-5}$	6093	0.100
$t\bar{t} \rightarrow \mu + jets$	6108	0.100	2	$3.3 \cdot 10^{-5}$
$t\bar{t} \rightarrow \tau + jets$	364	0.006	271	$4.5 \cdot 10^{-3}$
$t\bar{t} \rightarrow$ dileptonic	1220	0.026	1000	0.021
$t\bar{t} \rightarrow$ hadronic	3	$1.6 \cdot 10^{-5}$	4	$2.2 \cdot 10^{-5}$
$W + jets$	314	$6.0 \cdot 10^{-5}$	418	$7.9 \cdot 10^{-5}$
$Z + jets$	72	$7.6 \cdot 10^{-5}$	95	$1.0 \cdot 10^{-4}$
$QCD$	204	$2.5 \cdot 10^{-7}$	92	$1.1 \cdot 10^{-7}$

**Table 5.6:** The total selection efficiency and the event numbers for an integrated luminosity of  $1 \text{ fb}^{-1}$  for a neural network based selection as described in the text.

### 5.2.3 Selection Summary

A comparison of both selection methods shows that the neural network is about twice as effective in the suppression of the non- $t\bar{t}$  backgrounds. Also the signal fraction is larger for the neural network.

Considering only semileptonic  $t\bar{t}$  decays as signal, the signal to background ratio for the cut-based approach is  $S_\mu : B|_{\text{cut}} = 2.5 : 1$  for the muon selection and  $S_e : B|_{\text{cut}} = 2.6$  for the electron selection is achieved. In the neural network the ratios are  $S_\mu : B|_{\text{NN}} = 2.8 : 1$  for the muon channel and  $S_e : B|_{\text{NN}} = 3.2$  in the electron channel.

If only the non- $t\bar{t}$  events are considered as background (so every  $t\bar{t}$  decay is considered as signal), the ratios rise to  $S'_\mu : B'|_{\text{cut}} = 8.1 : 1$  for the muon cut selection and  $S'_e : B'|_{\text{cut}} = 6.3$  for the electron cut selection. For the neural network selection these ratios are  $S'_\mu : B'|_{\text{NN}} = 13.5 : 1$  for the muon and  $S'_e : B'|_{\text{NN}} = 12.2$  for the electron channel.

The non-signal  $t\bar{t}$  decays become the main background source. A closer inspection shows that especially the dileptonic  $t\bar{t}$  decays with one hadronically decaying tau lepton dominate, where the other leptonic top quark decay has a signal-lepton (either a muon or electron) in the final state. A smaller, but still significant fraction within the dileptonic  $t\bar{t}$  decays consists of an unidentified electron on one side (thus reconstructed as jet), and again the other leptonic decay has a either a muon or an electron in the final state.

To reduce the amount of hadronic  $\tau$  decays the possibility of  $\tau$ -jet identification is investigated, which is summarised in appendix E. The identification method does not perform well enough to be used, further dedicated studies are ongoing in the b/tau group of CMS.

For the further analysis the events of the neural network selection are used.

### 5.3 Event Interpretation

The event reconstruction is taken from the best result of the kinematic fit, which is the one with the smallest summed  $\chi^2$  of all three consecutive fits (see section 5.2). The actual four-vectors of the reconstructed particles are taken after the kinematic fit, which improves the kinematic properties of the particles on average.

#### Reconstruction Performance

The reconstruction can be checked by comparison with simulation information. For this the reconstructed top quarks are compared with the information of the initial top quarks in the simulation. Two values are of particular interest, the resolution and the bias value of the four-vector components. These are extracted by a fit to the residual distribution, the distribution of differences between generated and reconstructed value. At peak position this distribution can be approximated by a Gaussian, whose width is taken as resolution. The bias is the average shift of the mean value of the same fit with respect to zero. Zero is the expectation value for an unbiased distribution. In a simple procedure the fit is performed on a binned sample, the bin widths determined by demanding equally populated bins. The bin centre is determined by the centre-of-gravity of the actual distribution within the bin.

The masses of the top quarks are fixed to the constraint value that entered into the fit. In simulation this is determined from the input mass, in experimental data dedicated studies exist how to extract this value [55]. Examined are therefore  $p_T$ ,  $\eta$  and  $\phi$  values of the reconstruction of the hadronically and the leptonically decaying top quark.

#### $p_T$ reconstruction performance

Figure 5.15 shows the resolution and bias of the reconstructed  $p_T$  of the leptonically decaying top quark. Figure 5.16 shows the same for the hadronically decaying top.

From both resolutions can be seen that intermediate values of  $p_T$  are reconstructed best, which is also the statistically most important region. The reconstruction of the basic objects is better above a certain threshold of  $p_T$ , which in turn yields a well reconstructed composite object.

A bias can be seen, which needs to be corrected for. At low values the  $p_T$  is underestimated, which is slightly more pronounced for the leptonically decaying top. This bias is introduced by the combination of the kinematic fit and the properties of the basic recon-

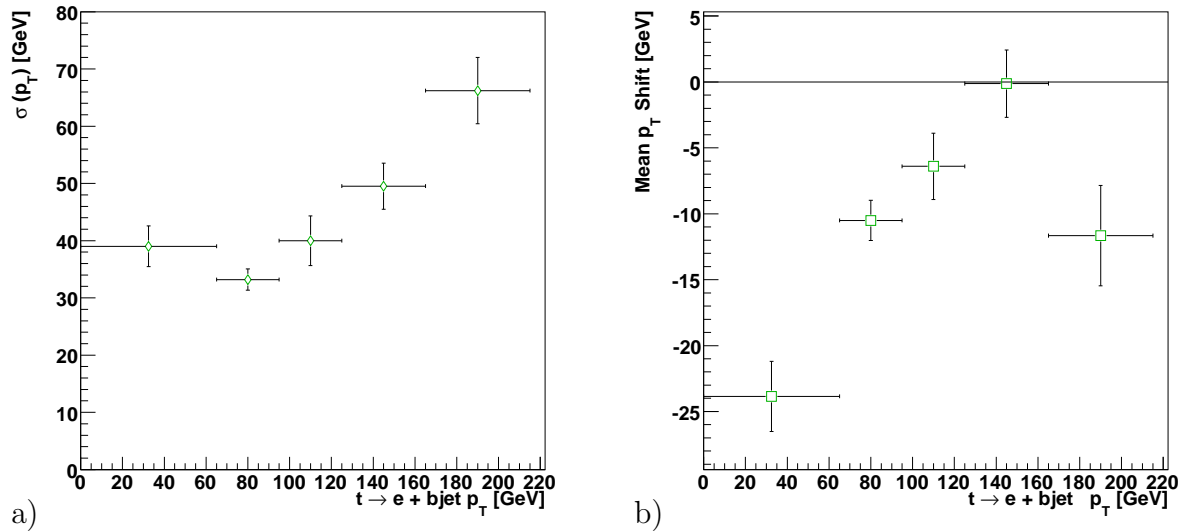


**Figure 5.15:** a) The  $p_T$  resolution of the leptonically decaying top quark and b) its bias. As example the result of the electron selection is shown, the muon selection has very similar shape.

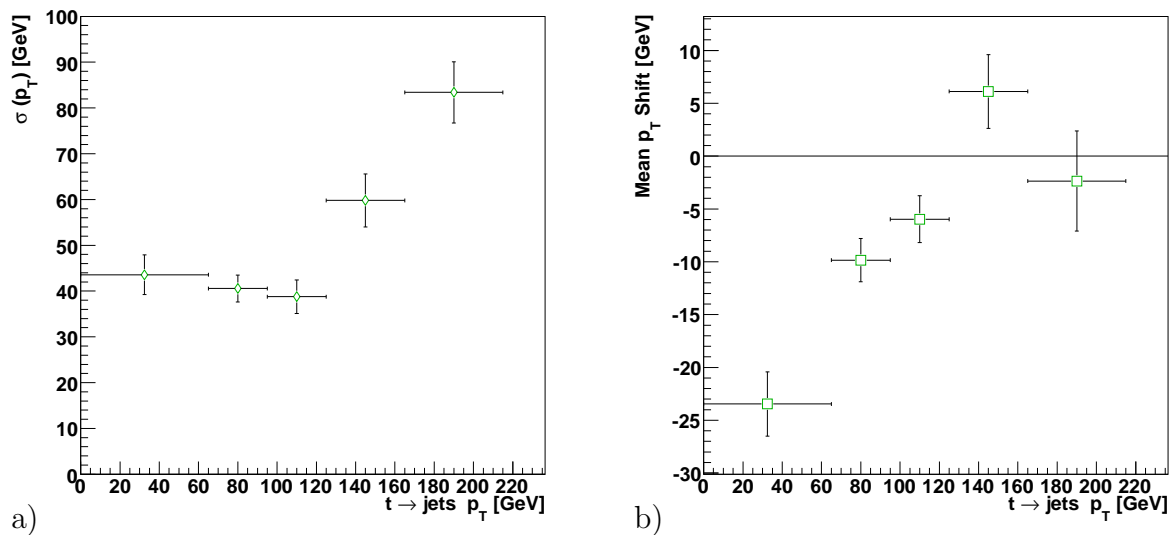


**Figure 5.16:** a) The  $p_T$  resolution of the hadronically decaying top quark. b) The reconstruction bias, again for the electron selection.

struction objects. The lepton is measured almost perfectly in comparison to the other objects. The neutrino is reconstructed via the  $W$  mass constraint.

As explained in the jet reconstruction and energy correction section 4.2.4 the jet resolutions are improvable. After the application of the energy correction the mean value of the residual distribution is one, but the spread is sizeable and asymmetric. Especially the asymmetry causes a systematic shift if several jets are combined. The influence on the performance and the result of the kinematic fit is more complicated, since the transformations are non-linear.

The bias of the reconstruction method can be reduced by applying a correction. Two constraints are imposed for the correction. The well reconstructed rapidity and the mass of the top quark remain constant. In the chosen parametrisation the correction is applied only on  $p_T$  and depends only on the  $p_T$  of the top quark.

This  $p_T$  correction is almost independent of the lepton flavour. The leptonically and the hadronically decaying top quark show a little difference. For  $p_T$  values in GeV the corrections are:

$$\begin{aligned} t_\ell : \quad p_T' &= 1.8 \cdot 10^{-3} p_T^2 + 0.44 p_T + 44 \quad \text{and} \\ t_h : \quad p_T' &= 1.5 \cdot 10^{-3} p_T^2 + 0.47 p_T + 43, \end{aligned}$$

where  $t_h$  indicates the hadronically and  $t_\ell$  the leptonically decaying top quark.

### Angular reconstruction performance

The reconstruction bias of  $\eta$  is negligible, being in the order of a few percent. Figure 5.17 shows the bias of the  $\eta$  reconstruction in the muon selection as an example.

No bias is present in the reconstruction of the azimuthal angle.

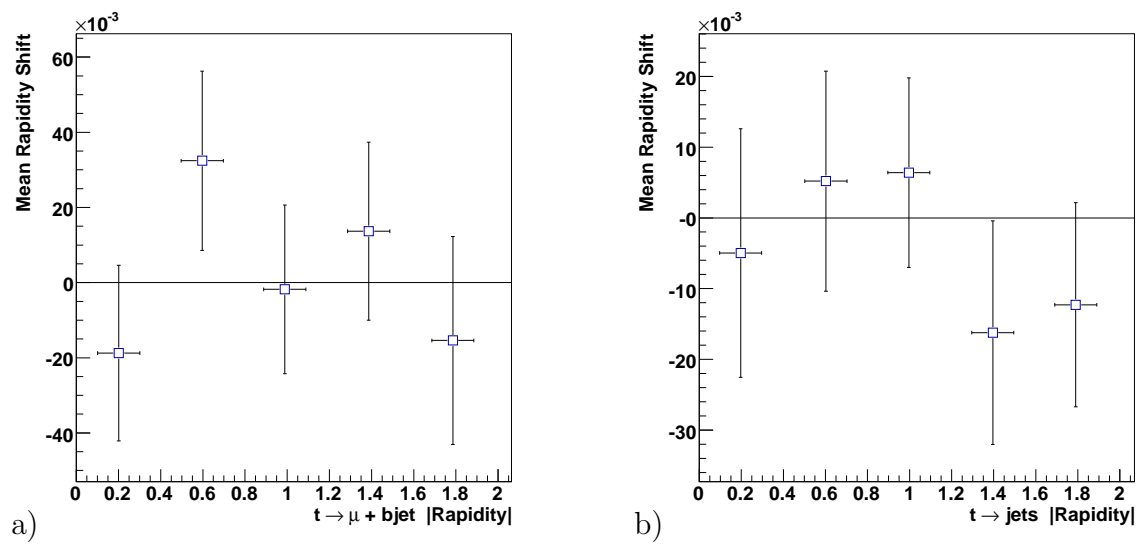


**Figure 5.17:** The bias in the reconstruction of  $\eta$  in the muon selection. a) shows the leptonically decaying top quark, b) the hadronic decay. The bias is compatible with zero.



# Chapter 6

## Differential Distributions of $t\bar{t}$ pairs

With the full event reconstruction as given in chapter 5.3 it is possible to analyse the complete  $t\bar{t}$  system. Differential cross sections within the  $t\bar{t}$  system are a powerful test of the underlying theory. The chosen observables cover several different aspects:

- the rapidity, which is sensitive to the production process;
- the invariant mass, an important measure both within the Standard Model (for properties like the production polarisation [56], which can be measured as Spin-correlation), as also an indicator for heavy particle decaying resonantly into  $t\bar{t}$ , thus enhancing the cross section at the mass peak;
- the transverse momentum, which is particularly sensitive to the influence of additional radiation.

From the experimental side the expected performance is important. The key point here is the examination of the quality and the representativeness of the complete reconstruction chain.

In the preparatory steps for the creation of the differential distributions care has been taken to identify possible bias and correct for it where possible. Several additional quality markers can be defined to determine the reconstruction quality. The ones examined here are the efficiency, purity, stability, the resolution and the shift of the mean value. The influence of the selection is also examined by determining the influence of the background uncertainty on the distributions.

Of great importance is the overall efficiency of reconstruction with respect to all  $t\bar{t}$  events within this decay channel. This efficiency  $e$  is defined for each bin  $i$  as the ratio of the

numbers of reconstructed events  $N_{\text{rec}}$  and generated events  $N_{\text{gen}}$ :

$$e_i = \frac{N_{\text{rec}}}{N_{\text{gen}}}.$$

By this number the representativeness of the selection and reconstruction is quantified.

Purity  $p$  and stability  $s$  are defined as the number of signal events  $N_{\text{rec}|gen}$  that are reconstructed and generated in the same bin, with respect to the reconstructed and the initially generated number in that bin:

$$p_i = \frac{N_{\text{rec}|gen}}{N_{\text{rec}}},$$

$$s_i = \frac{N_{\text{rec}|gen}}{N_{\text{gen}}}.$$

They quantify the migration effects, how many events are reconstructed in the same or another bin as they are generated. Purity, stability and efficiency range between zero and one.

Important is also the actual resolution of the given observable within this bin. As in the event reconstruction (section 5.3) also the shift of the mean value is given. For the distributions of the resolution  $\sigma$  and the bias which are shown here the determination method is slightly different than for the individual top quarks. To keep the maximal comparability to the other distributions the same bin sizes have been chosen. A Gaussian fit to the peak position of the difference between generated and reconstructed values is performed. The width and the peak position are extracted.

The influence of the background uncertainty is also examined. For this first the initially observed ratio of generated and reconstructed event numbers is evaluated. Then the amount of background is varied and a new ratio is computed. Since the actual uncertainties of the background contributions are hard to determine at present a variation of 100% is assumed. The variation of this ratio is shown as maximum and minimal deviation from unity in the shown distributions. The influence of the QCD background is not taken into consideration, due to the insufficient statistics.

## Rapidity distributions

The rapidity  $y$  is defined as

$$y = \frac{1}{2} \ln \frac{E + p_z}{E - p_z}.$$

In case of a massless object it is identical to the pseudorapidity. It is an invariant indicator of the motion of the centre-of-mass frame of the  $t\bar{t}$  system. The rapidity of the  $t\bar{t}$  is determined by the production, and thus correlated to the initial particle momenta.

The distributions can be assumed symmetrical around zero. To increase the number of well-populated bins the absolute value has been chosen for presentation.

The distributions for the rapidity are shown in figure 6.1 for the muon selection and in figure 6.2 for the electron selection. Part a) in both figures shows the resulting distribution. Comparing both selections it can be noticed that the events of the muon selection are more central than those of the electron selection on reconstruction level.

In part b) the overall efficiency is shown. The selection for the muon channel is more efficient in the central region and less efficient towards higher rapidity values than the electron selection. Within the electron channel the efficiency is completely even, showing no bias. In the muon channel a slight preference for small values of rapidity is given. The source of this difference could not be determined.

The information of the migration effects and about the reconstruction quality is given in the distributions of purity, stability and the resolutions. Stability and purity are shown in part c) of the figures, the resolutions in part d). The electron channel is of higher reconstruction quality and more uniform in both aspects. The migration effects are controlled, stability and purity are above or around 50%. At higher values of  $t\bar{t}$  rapidity the performance of muon reconstruction is improvable. The degradation of the resolution is reflected in stability values below 30% and the dropping efficiency. No bias is visible in the rapidity reconstruction, as shown in part e) of both figures.

The uncertainty of the background is shown in part f) of the figures, where both channels show a maximum deviation of about 7%.

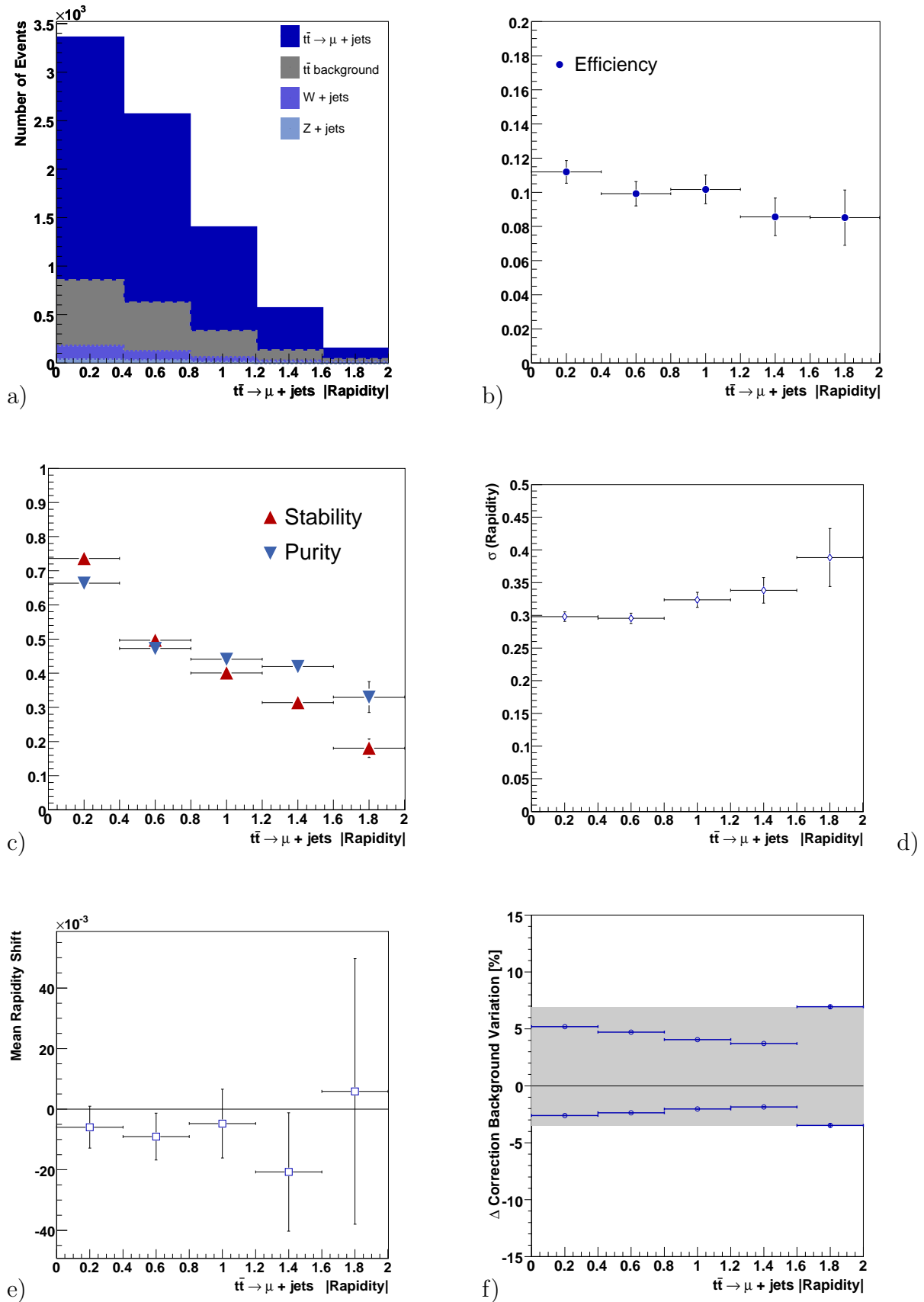


Figure 6.1: Differential distributions for the rapidity in the muon selection.

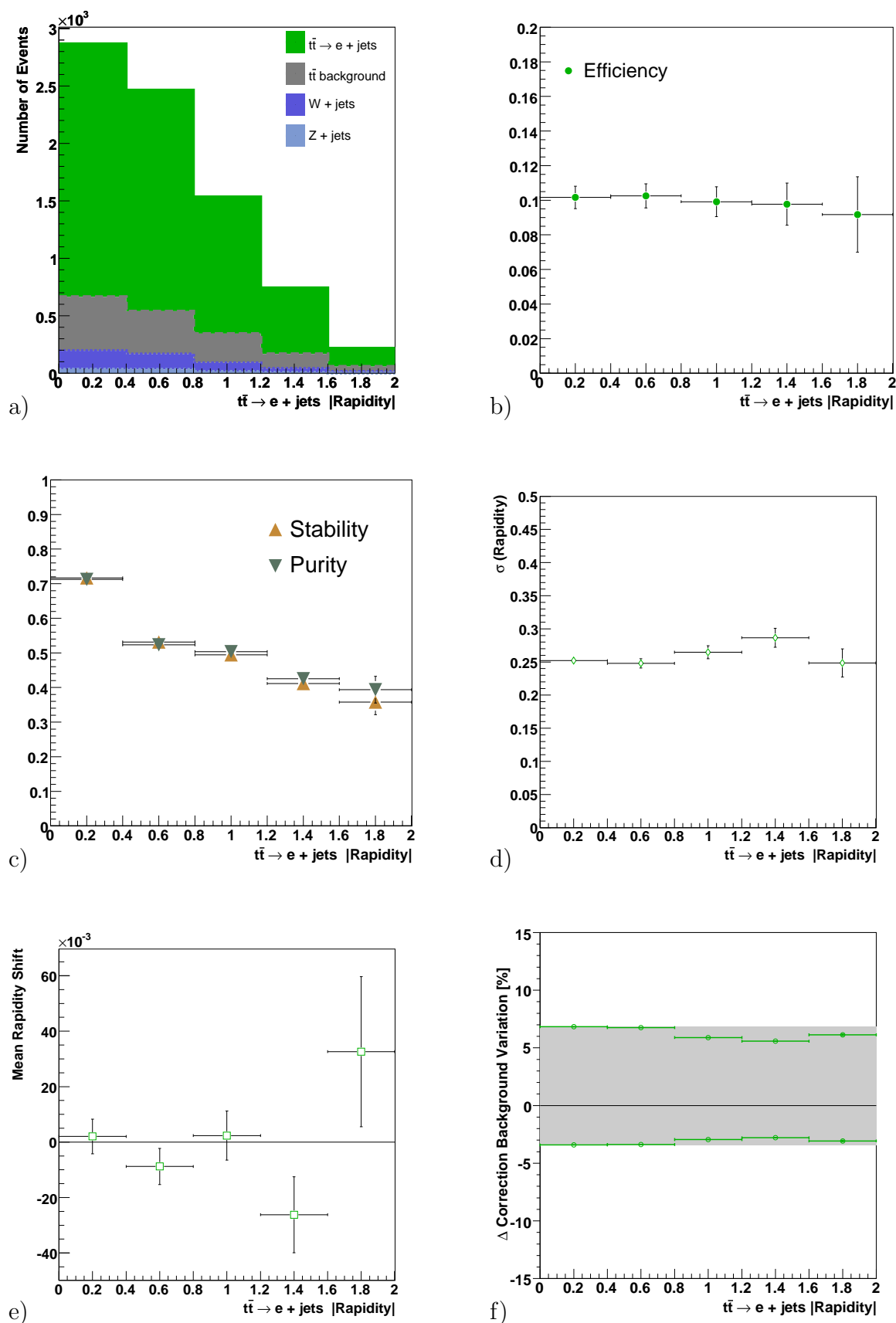


Figure 6.2: Differential distributions for the rapidity in the electron selection.

## Invariant Mass Distributions

The distributions for the invariant mass spectrum of the  $t\bar{t}$  system in the muon channel are shown in figure 6.3). The results of the electron selection are given in figure 6.4.

The  $m_{t\bar{t}}$  spectrum in the muon channel is shown in figure 6.3a), for the electron selection in figure 6.4a). The requirement to have a sufficient number of events sets an upper limit of about one TeV for the considered luminosity due to the rapidly falling distribution.

The overall efficiency (shown in part b)) is approximately constant over the chosen range, besides a slightly higher value for low masses.

As can be seen from the stability and purity distributions in part c) of the figures the actual distribution is a good description only for rather low masses up to 500 to 600 GeV, here shown in the first two bins. The mass resolution is good within these bins for both channels as shown in part d). But the reconstruction has a non-negligible bias, which can be seen in the figures part e). For the first two bins the resolution is in the order of the chosen width of the bins; for higher values the resolution is larger. The systematic shift of the mean value is related to the combination of a rapidly falling spectrum and the increasing resolution. If the values of a rapidly decreasing distribution are evenly smeared, the resulting distribution will have a bias to higher values. The effect here is even more pronounced, since the resolution also worsens with larger values of  $m_{t\bar{t}}$ . The resulting bias is below half of the resolution for all bins.

The influence of the background uncertainty is about two times higher for the electron channel than for the muon channel. In both cases the variation is less than 10% as depicted in part f) of the figures.

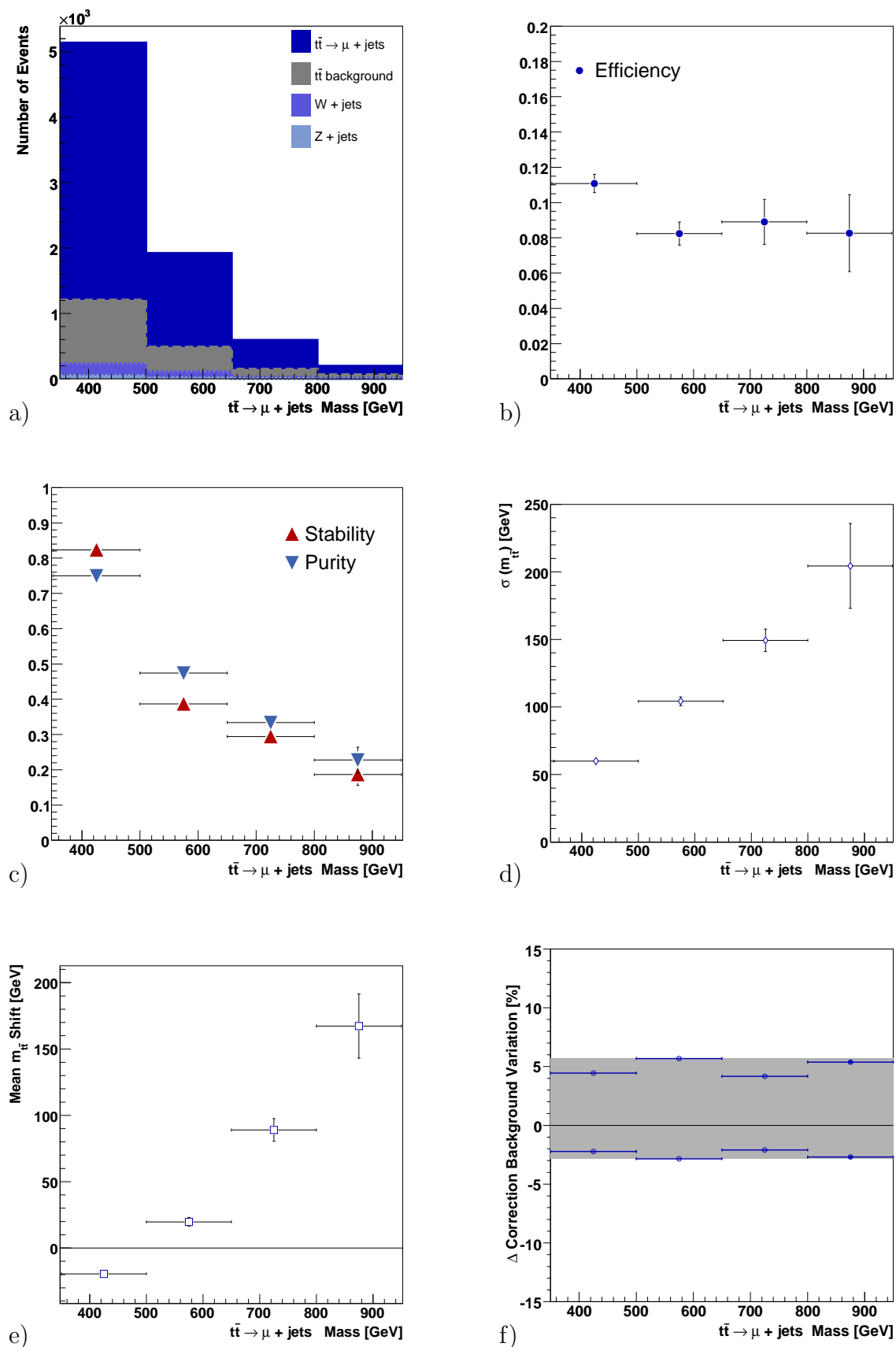


Figure 6.3: Differential distributions for the  $m_{t\bar{t}}$  in the muon selection.

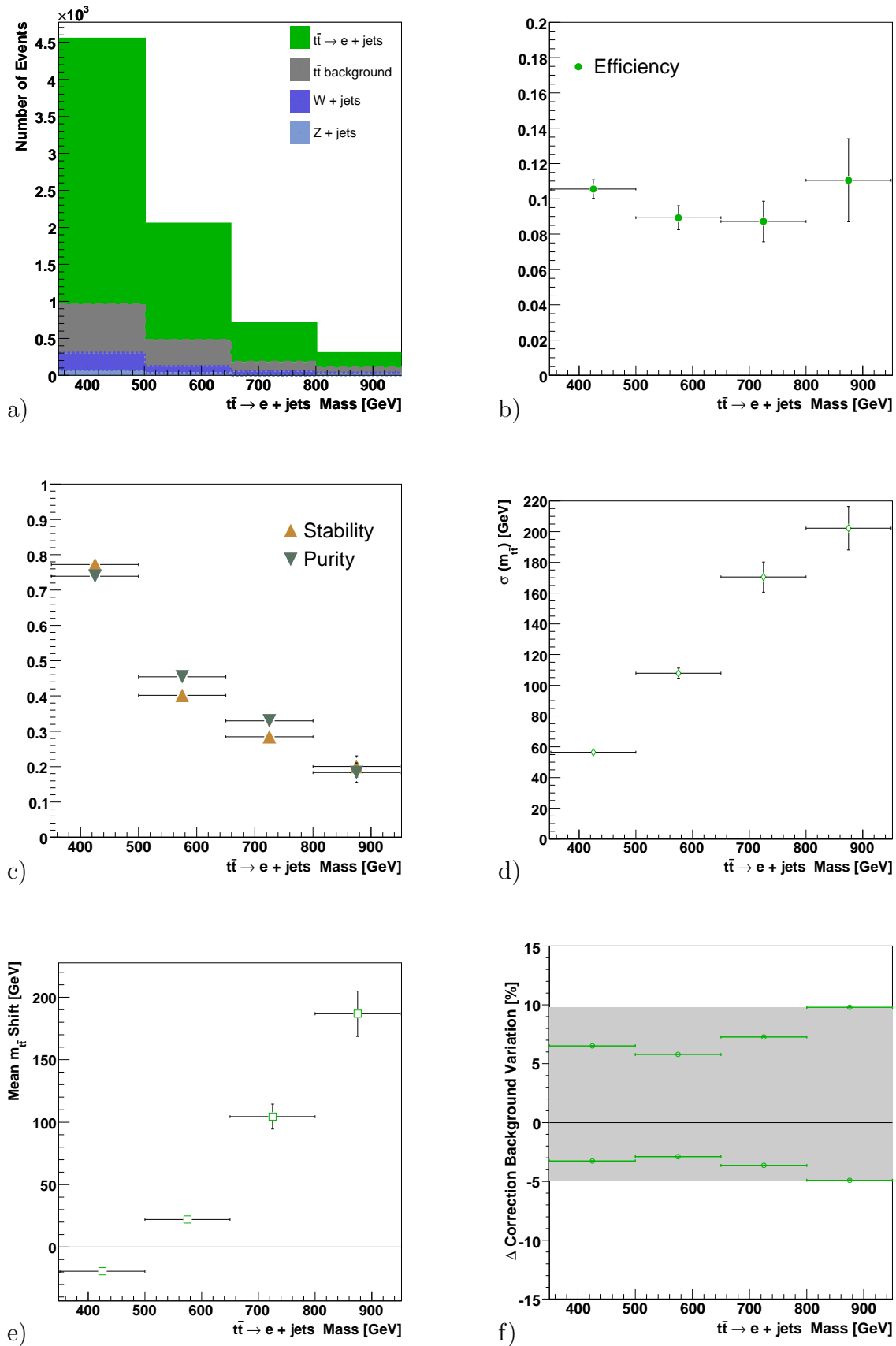


Figure 6.4: Differential distributions for  $m_{t\bar{t}}$  in the electron selection.

---

## $p_T$ Distributions

The  $p_T$  dependent distributions of the  $t\bar{t}$  system in the muon channel are shown in figure 6.5). The electron selection results are given in figure 6.6.

As part a) of the figures indicates, the  $p_T$  spectrum decreases even more rapidly than the invariant mass spectrum for larger values of  $p_T$ . This imposes a limit to the representative description to transverse momentum values of at most 200 GeV.

The overall efficiency in part b) clearly shows a dependency of the reconstruction on the  $p_T$  value of the  $t\bar{t}$  system. It has the highest efficiency for intermediate values between 50 and 150 GeV. Too low and high values are suppressed in the reconstruction and selection. The low values are most probably shifted to higher values, leading to the simultaneous increase of intermediate values.

These migration effects can be seen in the stability and resolution distributions. Both purity and stability drop significantly for transverse momenta larger than 50 GeV as depicted in part c) of the figures. As part d) and e) show the reason is the same as for the invariant mass spectrum. Although the resolution is good below 150 GeV, the reconstruction shows a strong bias. The underlying reason is the same as for the mass distribution, the exponentially decreasing spectrum is reconstructed with a method that has a worsening resolution. The consequence is a systematic shift, which is even more pronounced than in the case of the invariant mass spectrum.

The background uncertainty is at most 7% for both channels, as depicted in part f) of the figures.

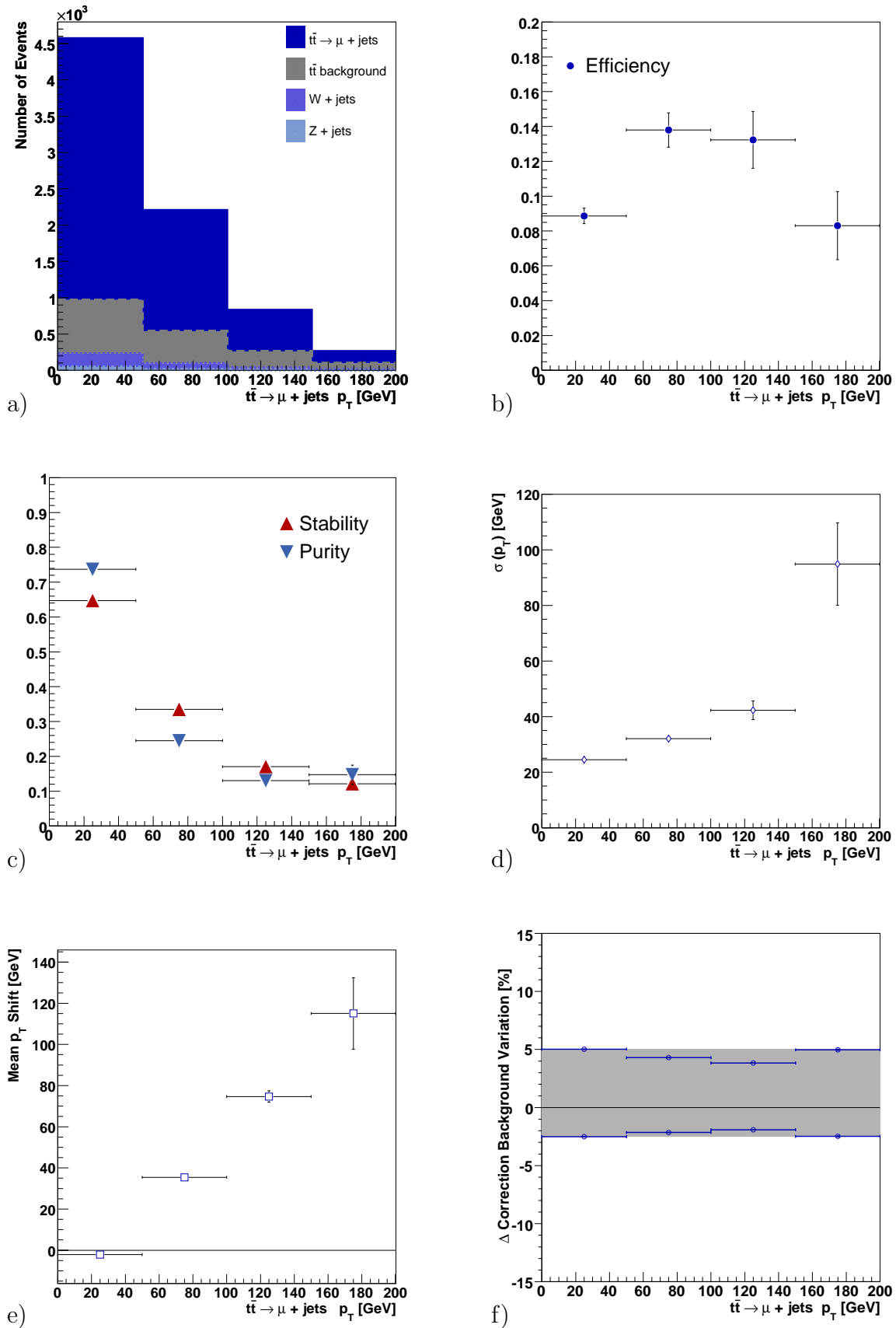


Figure 6.5: Differential distributions for the  $p_T$  in the muon selection.

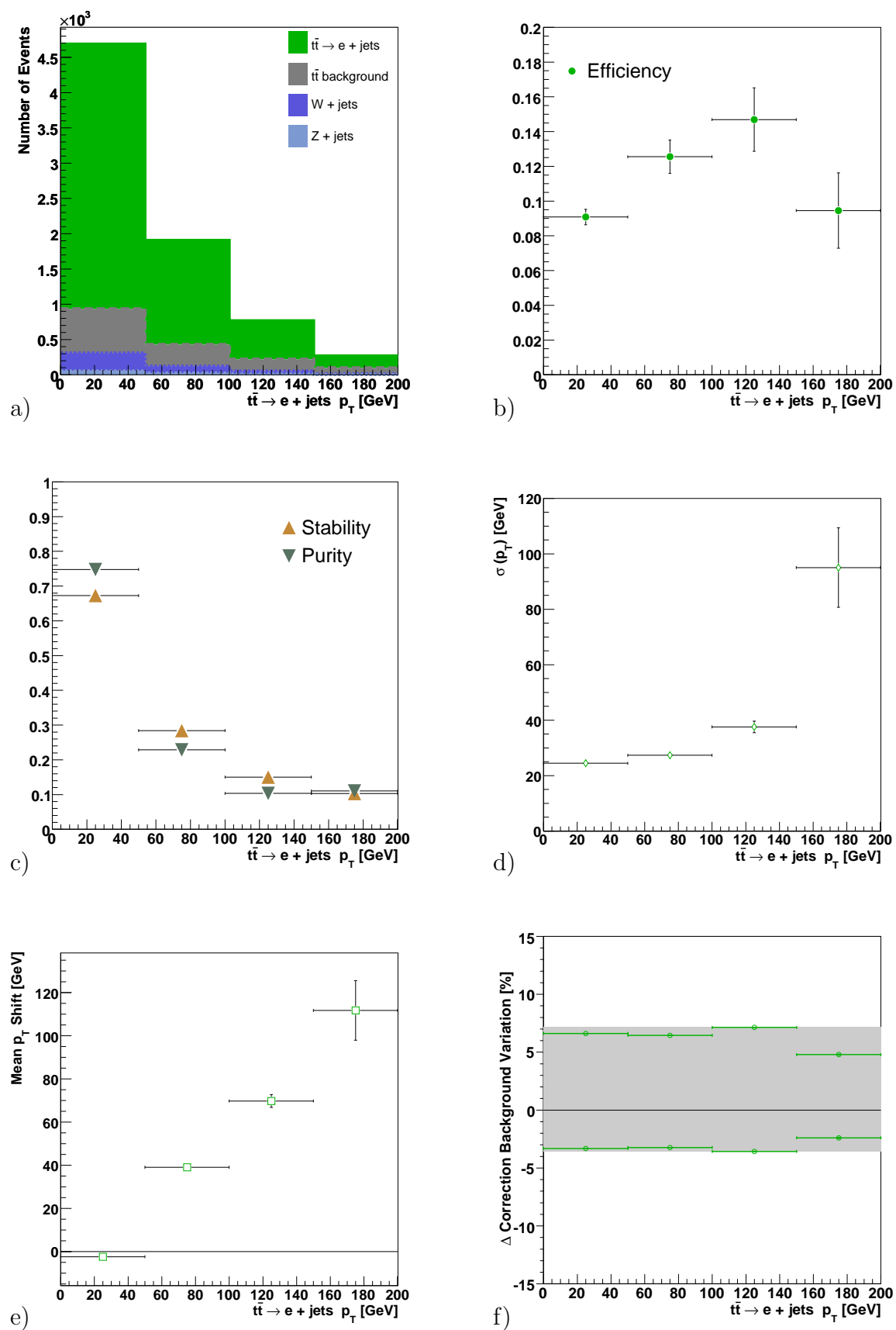


Figure 6.6: Differential distributions for  $p_T$  in the electron selection.

## 6.1 Summary

The differential cross sections show significantly different reconstruction qualities in the different observables. An assumed background uncertainty of 100% has an effect of less than 10% on the result. The overall reconstruction efficiency is largely unbiased, the small bias to reconstruct intermediate transverse momenta is explainable. Also the resolution of the variables is good. Especially the resolutions of the two most sensitive observables, the invariant mass and the transverse momentum, look promising.

The rapidity reconstruction works very well, without the application of any correction the reconstruction quality is unbiased over a large rapidity range. The reconstruction of the transverse momentum and the invariant mass does not perform as well as for the rapidity.

The underlying reason is the same, the large decrease in statistics with increasing values. The rapidly falling spectra are reconstructed with a worsening resolution. The outcome is an increasing bias, because of the shape of the initial distribution and the behaviour of the resolution.

For low invariant masses or for low transverse momenta even the naive method is very useful, showing little bias in combination with a good resolution. The measurement quality of a spectrum of either observable is biased, though.

# Chapter 7

## Conclusion and Outlook

### 7.1 Conclusion

With the foreseen start of collisions at the LHC in 2009 it should become possible to take a closer look at top quarks than ever before. For top physics the greatest advantage of the LHC will be the large production cross section for  $t\bar{t}$  pairs at its centre-of-mass energy. At the proposed  $\sqrt{s} = 14 \text{ TeV}$  a natural suppression factor of more than two orders of magnitude for  $W + jets$  production with respect to the Tevatron prevails. In connection with the large luminosity  $t\bar{t}$  events will be produced with rates in the order of one per second. These large advantages are linked with severe challenges. The main challenges determined the detector design. But even with a well understood detector the reconstruction and selection remains a complex task.

The subject of this analysis is the preparation of a measurement of differential cross sections in semileptonic  $t\bar{t}$  decays. The goal of measuring differential cross sections requires special attention in the reconstruction. Semileptonic  $t\bar{t}$  are very well suited for this examination from this technical point of view. Basically every detector component and subsequently every reconstruction object is needed.

The first central focus is therefore an accurate description and definition of the specific reconstruction objects like leptons or jets. For both leptons in the semileptonic  $t\bar{t}$  decay, either a muon or an electron, a dedicated isolation procedure is formulated. A dedicated and highly efficient identification method for electrons is developed. The leptons as very well defined objects are the most effective and accurate handle in the harsh environment of a hadron collider. Also they are the clearest signature of semileptonic  $t\bar{t}$  pair decays. Jet reconstruction is much more challenging. Especially the jet energy is not very well measured. An energy correction method is implemented to obtain a stronger correlation

between the reconstructed jets and initial partons.

The second central part of the thesis is the development of an efficient selection procedure. For this a two step approach is taken. The first step reduces the number of events and data volume by more than an order of magnitude, which makes the complex calculations of the second step feasible. In this second step two different methods are compared, a cut-based approach and the use of a neural network as multivariate technique. Either method reduces effectively the dominant background of  $W + jets$ . The neural network is found to be twice as effective as the cut based method in reducing the considered non- $t\bar{t}$  background processes.

The benchmark selection efficiency of 10% is achievable with a signal to background ratio of about three. The largest contribution to the background arises from other  $t\bar{t}$  decays. These events are dominated by those that contain hadronic  $\tau$ -lepton decays, mostly in dileptonic  $t\bar{t}$  decays. When counting only every  $t\bar{t}$  decay as signal and only non- $t\bar{t}$  as backgrounds, signal to background ratios of more than ten are achievable.

In the course of the selection also an event reconstruction is implemented. A kinematic fit procedure is developed for this. The outcome of the fit is used both for the selection and the final event interpretation.

As a test of the complete analysis chain the differential cross sections of the  $t\bar{t}$  system in rapidity, invariant mass and transverse momentum are examined. In analysis of collision data these will provide powerful tests on both the theoretical and experimental side. The Standard Model will be tested at the currently highest known particle mass with the potential to observe direct and indirect influences inside and beyond the Standard Model. Also the object and event reconstruction will be tested in a full combination of all available parts. Study of the spectra and their properties reveals that an efficient reconstruction with good resolution is possible. The influence of an estimated background uncertainty (excluding the QCD multi-jet background) is less than 10% for any of the observables in either decay channel. In some of the observables a little explicable bias is present.

The fundamental challenge is the accurate jet energy reconstruction, which appears in every part of the analysis chain.

## 7.2 Outlook

In the object reconstruction the jet energy scale is the most prominent topic for further studies, since it has the largest influence. For this the combination of jet energy correction methods and jet definition need to be studied. A smaller parameter size of  $R = 0.4$  might be better suited, but could not be further investigated for this thesis. Further studies

of the reconstruction of missing transverse energy are needed. The resolution directly influences the performance of the kinematic fit.

Different more efficient b-tagging algorithms have been investigated and implemented by the CMS b/tau group. These show promising performance, but were not available in the used software version. Also the inclusion of the b-tagging information in the reconstruction procedure has the possibility to improve the result.

The biggest improvement in the selection can be achieved by an efficient tagging of  $\tau$ -jets. Dileptonic  $t\bar{t}$  decays with at least one hadronically decaying tau lepton constitute the largest source of background after the full selection.

It could be attempted to determine the true differential distributions by the application of statistical methods like unfolding. These could be based upon the good resolution of the observables.

The availability of larger QCD samples is definitely needed. The currently available statistics are too small to make reliable predictions. Most important are efficient methods for the background estimation from data.

In addition dedicated studies of trigger efficiencies on the whole analysis are needed.

Some top quark properties cannot be determined at the LHC, for example the width. The exact determination of these properties will most probably be reserved to the production and detection at a lepton collider with sufficient centre-of-mass energy. The major advantages over a hadron collider is the much cleaner environment and the well-defined, possibly adjustable centre-of-mass energy. A possibility for this is the International Linear Collider ILC [57].



# Appendix A

## Electron Likelihood technique

For a particular value  $\chi_0$  of an electron candidate a likelihood value  $\mathcal{L}$  can be determined from the reference distributions. This needs to be done in each category (either electron or fake) and in each variable. In all generality the probability  $p$  for a certain class  $i$  in a certain observable  $\psi$  at the value  $\chi_0$  can be defined as

$$p_{i,\psi} = \frac{pdf_{i,\psi}|\chi_0}{\sum_j pdf_{j,\psi}|\chi_0}$$

For the two basic classes here (electron, fake) this yields two probabilities  $p$ :

$$\begin{aligned} p_{electron,\psi} &= \frac{pdf_{electron,\psi}(\chi_0)}{pdf_{electron,\psi}(\chi_0) + pdf_{fake,\psi}(\chi_0)} \\ p_{fake,\psi} &= \frac{pdf_{fake,\psi}(\chi_0)}{pdf_{electron,\psi}(\chi_0) + pdf_{fake,\psi}(\chi_0)} \end{aligned}$$

These values can be combined into a likelihood value  $\mathcal{L}_i$  for each category  $i = \text{electron, fake}$ .

$$\mathcal{L}_i(\chi_0) = \prod_{\psi} \frac{p_{i,\psi}(\chi_0)}{\sum_j p_{j,\psi}(\chi_0)}$$

The electron likelihood ratio LHR is the final value, derived from the Likelihood values:

$$\text{LHR}_{\text{electron}} = \frac{\mathcal{L}_{\text{electron}}}{\mathcal{L}_{\text{electron}} + \mathcal{L}_{\text{fake}}}.$$

A probabilistic interpretation of the likelihood ratio is only possible if the observables are uncorrelated. If only distinction between different classes is asked, not orthogonalised input variables are also usable. Still it needs to be emphasised that it is of highest importance to understand the input, including the source of any correlation.

# Appendix B

## Electron Probability Density Functions

On the following pages the probability density distributions are given, used for the electron likelihood as described in section 4.2.3. The distributions for the showering barrel class were already presented in the main text.

Important are the correlations between the different observables that enter the likelihood function. For a probabilistic interpretation of the likelihood results, the observables need to be uncorrelated. The chosen set of observables fulfils this requirement for all classes.

In figure B.1 the correlation coefficients are summarised. The correlation coefficient  $\rho_{xy}$  is defined as the covariance  $\sigma_{x,y}$  of two variables  $x, y$  normalised to their variances  $\sigma_x, \sigma_y$ :

$$\rho_{xy} = \frac{\sigma_{xy}}{\sqrt{\sigma_x^2 \sigma_y^2}}.$$

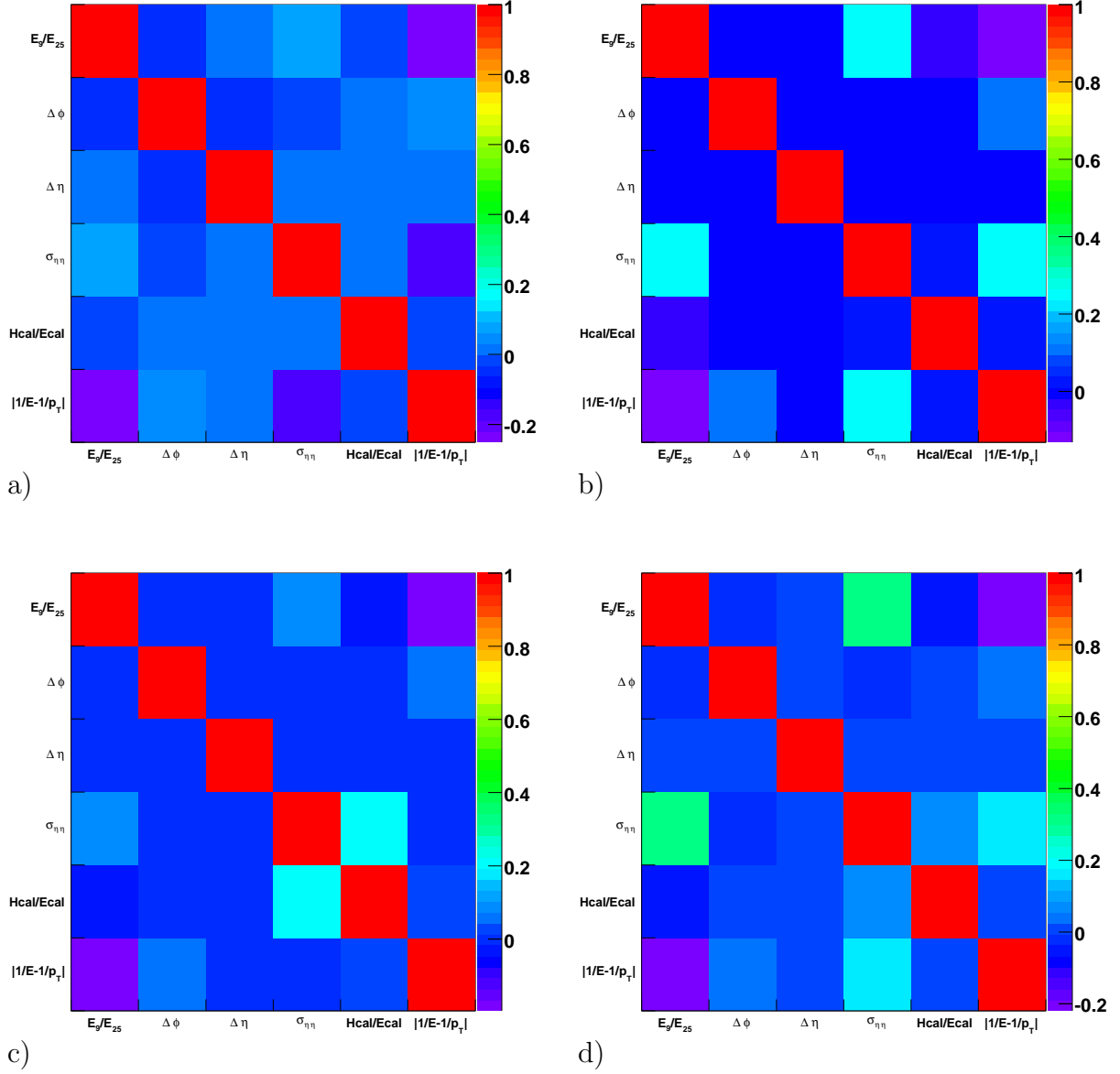


**Figure B.1:** The correlation values between the input variables within the four different classes. a) For the non showering barrel and b) endcap. c) For the showering barrel and d) endcap.

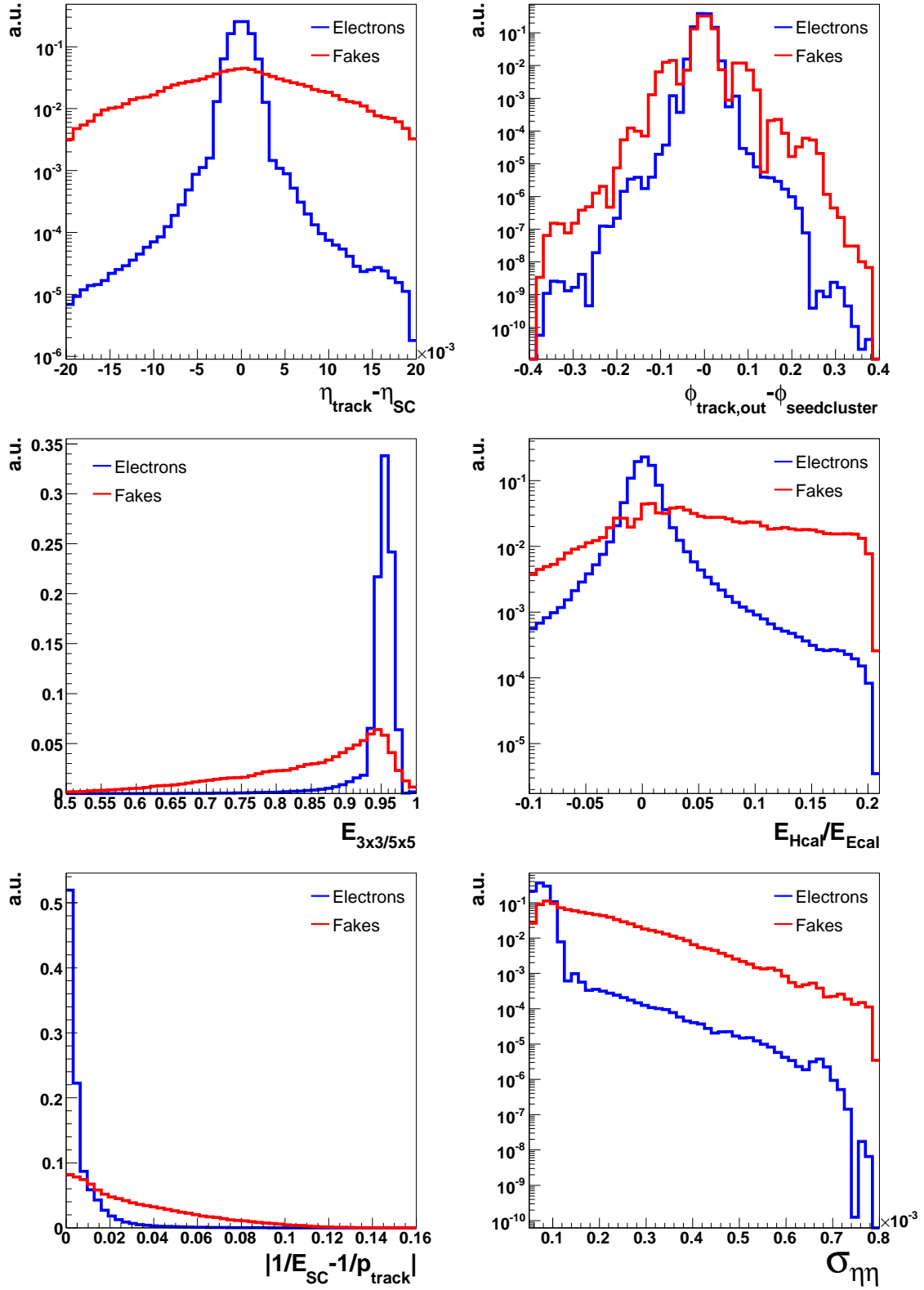


Figure B.2: The pdfs for the non showering barrel class.

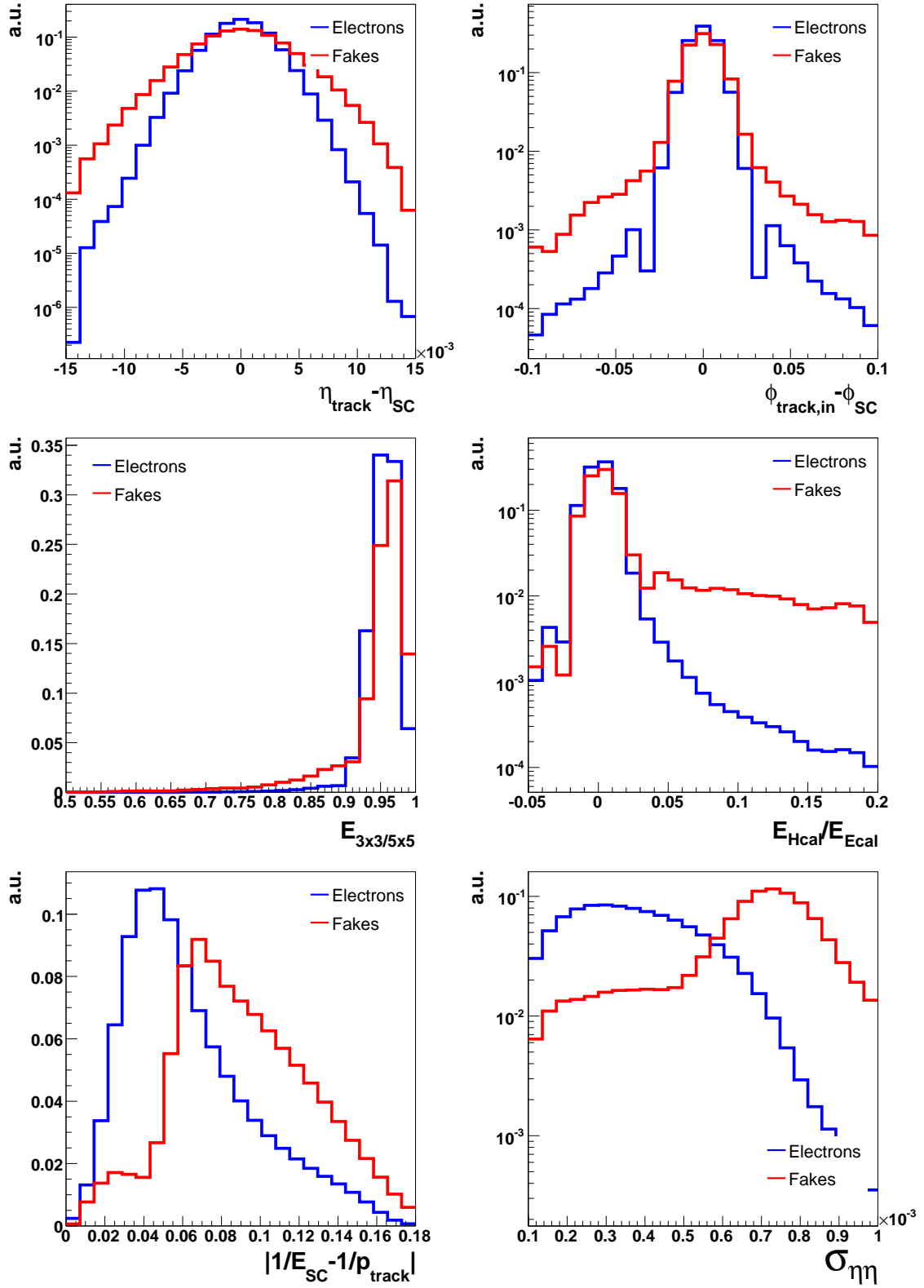


Figure B.3: The pdfs for the non showering endcap class.

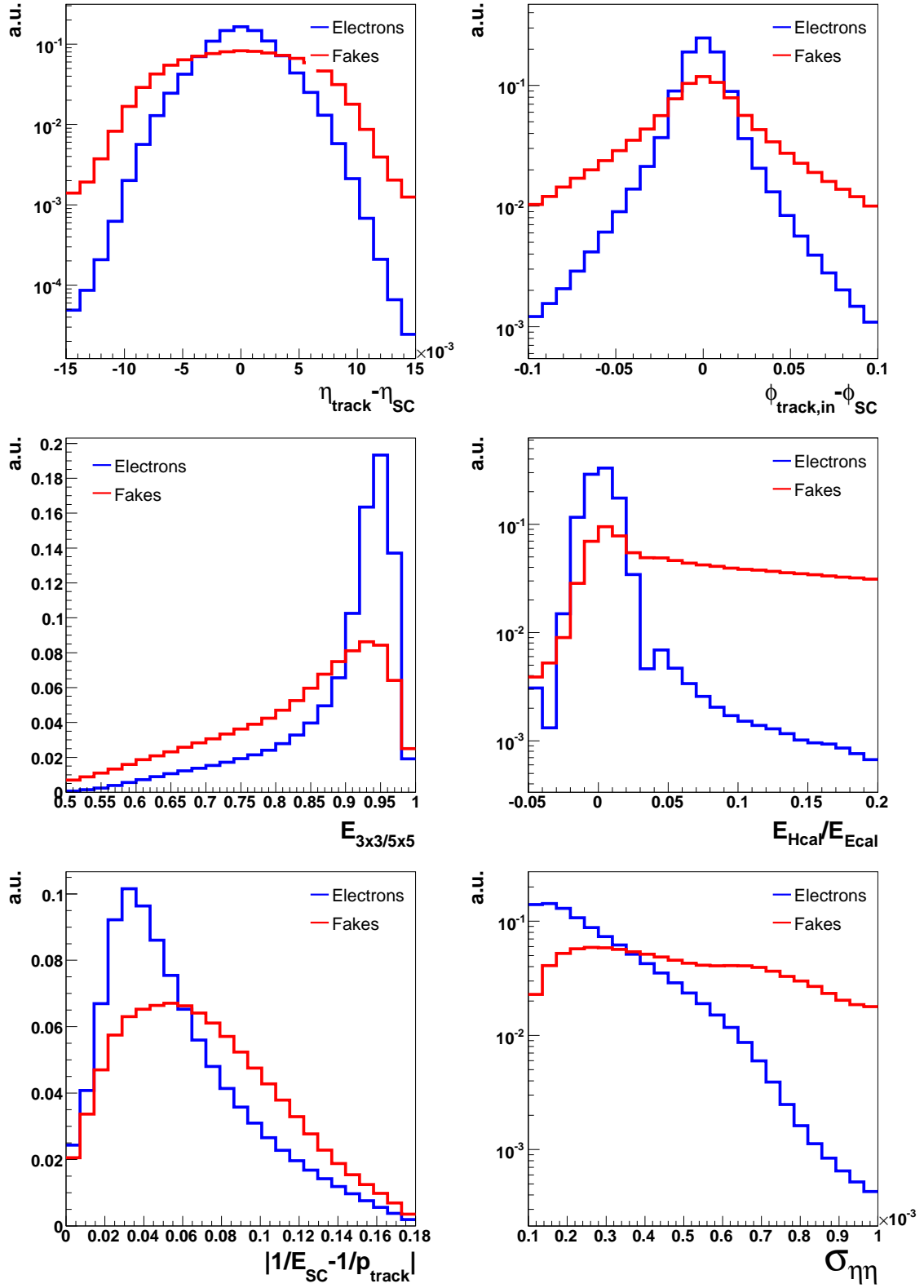


Figure B.4: The pdfs for the showering endcap class.

# Appendix C

## Least Square fitting with external constraints

A full mathematical reference can be found in [53].

In an event are several measured quantities  $\vec{y} = y_1, y_2, \dots$  with experimental uncertainties  $\sigma_y$ . In addition there are unmeasured quantities  $\vec{a} = a_1, a_2, \dots$ . Constraints can be formulated in terms of the true quantities:

$$f_i(\bar{y}_1, \bar{y}_2, \dots, \bar{a}_1, \bar{a}_2, \dots) = 0.$$

In general these constraints will not be fulfilled by the measured quantities  $\vec{y}$ . Corrections  $\Delta\vec{y}$  can be computed, so that these corrected  $\vec{y}' = \vec{y} + \Delta\vec{y}$  fulfil the constraints. At the same time the weighted sum  $S(\vec{y})$  has to be minimal, with the covariance matrix  $\mathcal{V}$ :

$$S(\vec{y}) = \Delta\vec{y}^T \mathcal{V}^{-1} \Delta\vec{y}.$$

A common method to determine the local extrema of multidimensional function is the application of *Lagrange Multipliers*  $\lambda_i$ . The function to be minimised is then defined as:

$$L(\vec{y}, \vec{a}, \vec{\lambda}) = S(\vec{y}) + 2 \sum_i \lambda_i f_i(\vec{y}, \vec{a}).$$

In the case of linear constraints the minimum of  $L(\vec{y}, \vec{a}, \vec{\lambda})$  is found in a single step. For non-linear constraints like mass constraints the solution can be found iteratively by linearisation in each step.

In vector notation the values in the current iteration  $f'_i, \vec{y}', \vec{a}'$  are determined from the values before  $f_i^*, \vec{y}^*, \vec{a}^*$ :

$$f'_i(\vec{y}', \vec{a}') = f_i^*(\vec{y}^*, \vec{a}^*) + \mathcal{A}(\Delta\vec{a} - \Delta\vec{a}^*) + \mathcal{B}(\Delta\vec{y} - \Delta\vec{y}^*) = 0 \quad (\text{C.1})$$

The Jacobi matrices  $\mathcal{A}$  and  $\mathcal{B}$  are the matrices of the partial derivatives of the constraints with respect to the measured and unmeasured quantities  $\vec{y}$  and  $\vec{a}$ :

$$\mathcal{A} = \frac{\partial \vec{f}}{\partial \vec{a}} \quad \text{and} \quad \mathcal{B} = \frac{\partial \vec{f}}{\partial \vec{y}}.$$

For computation it is easier to write the linearised formula C.1 with a single vector  $\vec{c}$  that is only dependent on the values of the previous iteration:

$$f'_i(\vec{y}', \vec{a}') = \mathcal{A}\Delta\vec{a} + \mathcal{B}\Delta\vec{y} - \vec{c} = 0 \quad \text{with} \quad \vec{c} = \mathcal{A}\Delta\tilde{y}^* + \mathcal{B}\Delta\tilde{a}^* - \vec{f}_i^*.$$

With this the function to be minimised becomes:

$$L = \Delta\vec{y}^T \mathcal{V}^{-1} \Delta\vec{y} + 2\lambda^T (\mathcal{A}\Delta\vec{a} + \mathcal{B}\Delta\vec{y} - \vec{c}).$$

The condition for an extremum is then:

$$\begin{pmatrix} \mathcal{V}^{-1} & 0 & \mathcal{B}^T \\ 0 & 0 & \mathcal{A}^T \\ \mathcal{B} & \mathcal{A} & 0 \end{pmatrix} \begin{pmatrix} \Delta\vec{y} \\ \Delta\vec{a} \\ \lambda \end{pmatrix} = \begin{pmatrix} 0 \\ 0 \\ \vec{c} \end{pmatrix}$$

With two shorthand definitions for matrix products

$$\mathcal{V}_\mathcal{B} = (\mathcal{B}\mathcal{V}\mathcal{B}^T)^{-1} \quad \text{and} \quad \mathcal{V}_\mathcal{A} = (\mathcal{A}^T\mathcal{V}_\mathcal{B}\mathcal{A})$$

the corrections and the Lagrange Multipliers can be calculated by matrix multiplication:

$$\begin{aligned} \Delta\vec{y} &= (\mathcal{V}_\mathcal{B}^T\mathcal{V}_\mathcal{B} - \mathcal{V}_\mathcal{B}^T\mathcal{V}_\mathcal{B}\mathcal{A}\mathcal{V}_\mathcal{A}^{-1}\mathcal{A}^T\mathcal{V}_\mathcal{B})\vec{c} \\ \Delta\vec{a} &= (\mathcal{V}_\mathcal{A}^{-1}\mathcal{A}^T\mathcal{V}_\mathcal{B})\vec{c} \\ \vec{\lambda} &= (\mathcal{V}_\mathcal{B}\mathcal{A}\mathcal{V}_\mathcal{A}^{-1}\mathcal{A}^T\mathcal{V}_\mathcal{B} - \mathcal{V}_\mathcal{B})\vec{c} \end{aligned}$$

The package used in this thesis is based on the ABCFIT by J.B. Hansen and O. Buchmüller. The actual code used was part of ORCA and is a C++ rewrite of the ABCFIT package by V. Klose and J. Sundermann. Some minor modifications of optimisation and bug removal in the ORCA implementation were performed.

From the computed minimal  $\chi_{min}^2$  value a probability can be determined for the known number of degrees of freedom  $ndf$ . This is computed from the incomplete Gamma function  $\Gamma(x, a)$ , representing the probability that for a correct model the  $x = \chi^2/2$  value for a given number  $a = ndf/2$  should be less than the computed one. The probability  $p_{fit}$  of a given fit to be right is then

$$p_{fit} = 1 - \Gamma\left(\frac{\chi^2}{2}, \frac{ndf}{2}\right).$$

# Appendix D

## Artificial Neural Networks

An extensive and comprehensive overview of (artificial) neural networks is given in [54].

Here the technical details are given. The toolkit used for network creation and training is the *Stuttgart Neural Network Simulator SNNS* [58].

### Network layout

The network is created to have eight input nodes, fifteen hidden nodes and two output nodes. The fully connected network graph is shown in D.1.

The information of the network is stored in the weights of the connections. This network is technically a function that calculates two numbers (in the range of  $[0, 1]$ ) out of the eight input values.

The eight observables are described in the selection chapter. Their range is restricted to  $[0, 1]$ , which is done by a simple linear transformation from the initial range to this target range.

The input values can be formalised as activation values  $v_i$  of the input nodes  $i$ . These activation values are weighted with the connection weights and serves as input to the connected nodes. Their activation value is then determined from an activation function. Used here is the *logistic activation function* for a node  $j$ , connected to the nodes  $i$  with connection weights  $w_{ij}$ :

$$a_j = \frac{1}{1 + \exp(\sum_i w_{ij}v_i)}.$$

The same idea is used for the output nodes of the network.

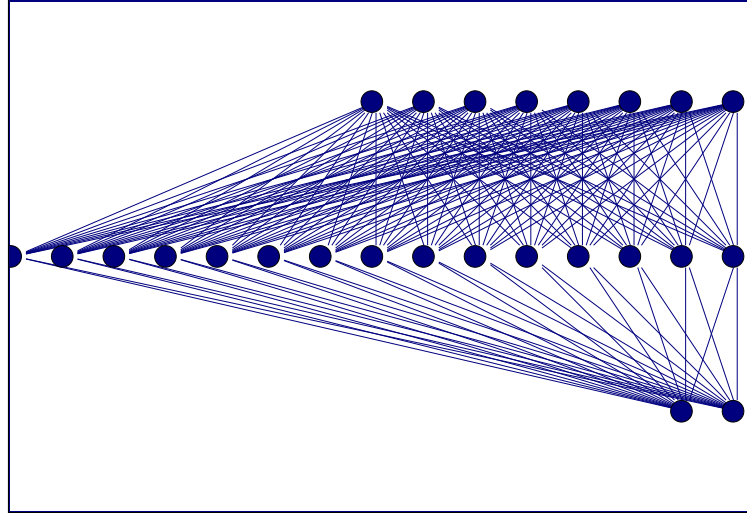


**Figure D.1:** The layout of the chosen neural network with eight input, fifteen hidden and two output nodes.

## Training

Training is the process to adapt the network to approximate the given task. This means that the initial weights are adapted using a learning algorithm. For this the network is presented an input vector of values and given it the right output vector for comparison. This procedure is called supervised learning.

The actual adaption routine is the backpropagation with a momentum term. Weights are changed according to the learning parameter  $\eta$  and the momentum term  $\mu$  for the output value  $o_i$  of a node:

$$\Delta w'_{ij} = \eta o_i \zeta + \mu \Delta w_{ij}.$$

In this an additional function  $\zeta$  is introduced for flat spot elimination, which is described in [58]. The fundamental parameter of  $\zeta$  is the difference between the current value and the taught value.

To perform this training two representative data samples are needed. These are needed for training and validation and must not be used for anything else. The training sample is used to adapt the weights to minimise the overall error of the network. The validation sample is only used to test the generalisation power of the network.

For the usage as pattern recognition method it is important to present the network an equal number of input vectors for each of the classes that need to be distinguished. In the case of a network for selection this means that an equal number of signal and background events are used, although this is not the natural ratio. It is equally important that within

the classes the *internal* ratio of events is natural, though. For the signal this is easy, since only one source is present. But for the background it is important that the internal ratios of different sources are chosen accordingly. Otherwise the result will be distorted, since the total error with respect to the validation sample is minimised.

The training process is done in cycles, where the whole training sample is presented in random order for each of the cycles. For the evaluation an error can be defined as between the known output  $o_{known}$  and the current network answer  $o_{net}$  for the input vector  $\vec{x}$  and the weight vector ( $\vec{w}$ ):

$$E(\vec{x}, \vec{w}) = |o_{known} - o_{net}(\vec{x}, \vec{w})|^2.$$

The mean squared error (MSE) is based on this, averaging over a large set:

$$MSE(\vec{w}) = \lim_{N \rightarrow \infty} \frac{1}{N} \sum_{k=1}^N E(\vec{x}_k, \vec{w}_k).$$

The optimal network is found, when the validation error is at its minimum. As a general rule the error of the training set will always decrease with an increasing number of training cycles. But the validation error has an absolute minimum. This minimum is usually the network with the best generalisation power.

The validation minimum is well pronounced if over-training occurs, but also can be found in cases without over-training. Over-training happens, when the training pattern is memorised instead of the general features of the sample. Instead of approximating the general features of the presented data sample, the specific attributes of the training sample is stored.

In figure D.2 different training and validation curves are shown. Part a) shows the MSE of the network used for the muon selection. The training error is always decreasing, but the validation remains constant after an initial decrease. Part b) depicts the MSE of a different, more complex network. The total error is a little lower in this case, indicating a better classification potential of the network. But after the initial drop of the validation error over-training becomes evident after a sufficient number of cycles, leading to a performance degradation.

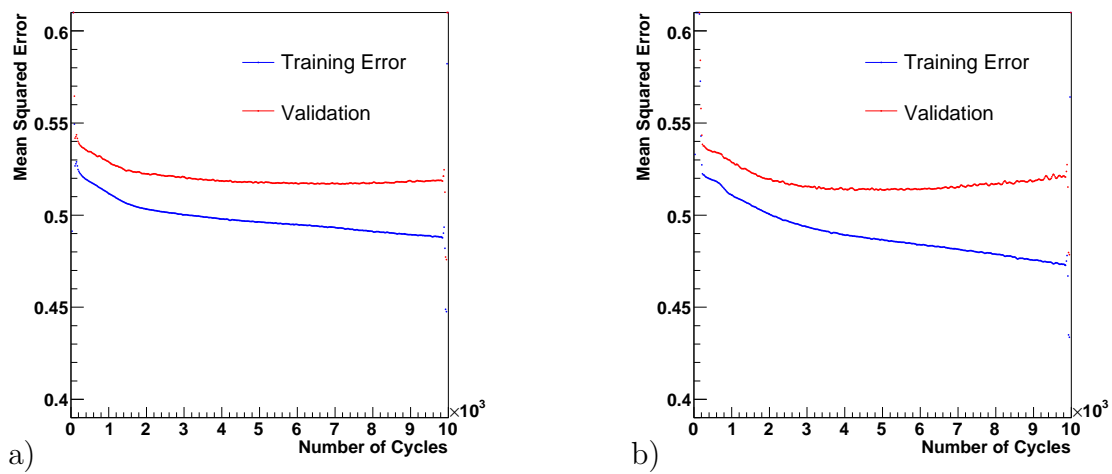


**Figure D.2:** Training and validation errors of two networks. a) shows the errors of the network used within the muon selection. In b) an example for the occurrence of over-training is shown for a different network topology.

# Appendix E

## Identification of $\tau$ -jets

Within CMS an own working group exists, that is dedicated to the identification and reconstruction of tau leptons. A proposal how to perform this task exists, but was not available in the software at the time of writing [59].

Based on the ideas presented in the note an identification method for hadronic tau lepton decays is developed. Tau leptons decay hadronically in 65% of all cases and have a lifetime of  $\Gamma = 291 \cdot 10^{-15}$  s. The leptonic decays are very hard to identify as tau decay, which is not described here.

The hadronic decays form a jet that has some special properties compared to an *average* jet. Usually the hadronic decay contains several neutral particles and very few charged particles. The majority is either with a single charged particle (*one-prong* decay) in about 77% of the hadronic decays. The rest are almost only three-prong decays. The resulting jet is usually narrower than an *average* jet of comparable energy [59].

This leads to a possibility to identify isolated hadronic tau decays. In a first step candidates for a closer inspection are formed. Every jet is checked for an association to tracks. As sketched in figure E.1 three cones are defined. The inner *signal* cone and outer *isolation* cone are checked for tracks and energy in both the Ecal and the Hcal. The signal cone is built around the leading track (the one with the highest  $p_T$ ), that is found in a *matching* cone around the jet axis. The isolation cone is centered around the tau-jet axis.

The settings for the finding of candidates are  $\Delta R_s \leq 0.07$  for the signal cone within a matching cone of  $\Delta R_M \leq 0.1$  and  $\Delta R_{Iso} \leq 0.5$  for the isolation cone. Tracks are only counted above a  $p_T$  threshold of 1 GeV, the leading track needs to have at least 5 GeV.

A likelihood method is used for the tau-jet identification. The general method is explained for the electron identification in section 4.2.3, the details in appendix A. All shown distributions are interpreted as probability density functions, normalised to unity area. The

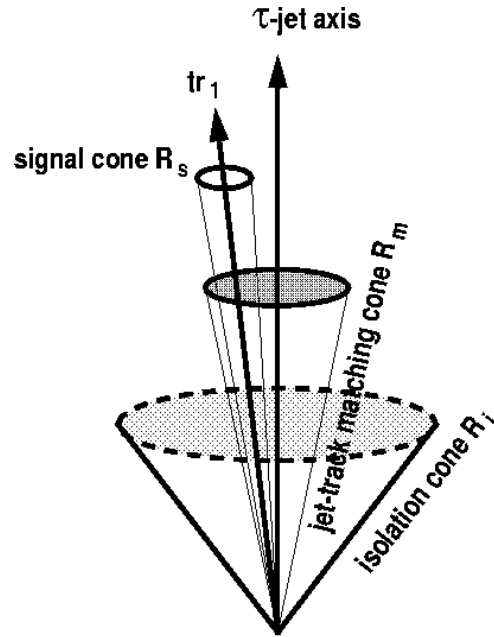


**Figure E.1:** The principle of tau-jet identification based on track isolation[59].

distinction between *true* and *fake* tau-jets is again made by a match using the information from event generation.

Several observables are used for the identification. There are several observables related to the tracks within the two cones, shown in figure E.3. Part a) shows the number of tracks inside the total cone, which should be one or three for taus in the case of perfect tracking. Part b) shows the number of tracks only inside the isolation cone (outside the signal cone), which should be zero for perfectly isolated tau-jets. Part c) shows the  $p_T$  of the leading track; which is usually larger than the random tracks of non-tau-jets. Part d) shows the sum of the track  $p_T$  of the tracks only inside the isolation cone (and outside the signal cone). As said for the number of tracks inside the isolation cone, this should be zero for tau-jets.

Also there are several observables related to the calorimeter information within the cones, shown in figure E.4. Part a) shows the number of individual Ecal clusters inside the isolation cone. Since the tau-jet is rather collimated this number should be small. Part b) shows the electromagnetic fraction (emf) of the jet. Due to the hadronic nature the fraction is dominated by small numbers, although this is altered by the decay of neutral pions that are produced in the tau decay. Part c) shows the summed energy of those Ecal cluster that are only in the isolation cone, which also should be small due to the collimation of tau-jets.

In figure E.4d) the invariant mass is shown, determined from the track and calorimeter information. The higher values for non-tau-jets indicate other reconstructed particles than a tau.

The final result from the application of the whole method in terms of Likelihood Ratio is shown in figure E.2. By the method a clearer separation of tau-jets from other objects is possible. But no clear cut is indicated. The number of candidates is simply too large to be effective.

Since the main usage is the rejection of true tau leptons, the method is not applied. Further more dedicated studies are needed. Several opportunities for improvements exist, both in the building of the candidates and the refinement of the requirements. For example the lifetime could be exploited by using the extraordinarily good resolution of the vertex detector as for the b-tagging. Also the inclusion of more observables and the employment of a neural network is likely to improve the performance of identification.

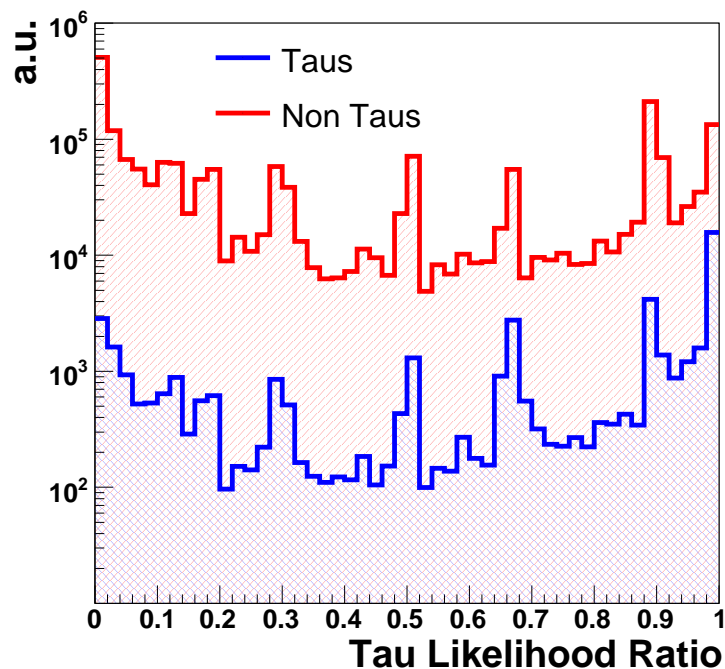


**Figure E.2:** The likelihood ratio distribution for tau-jet identification.

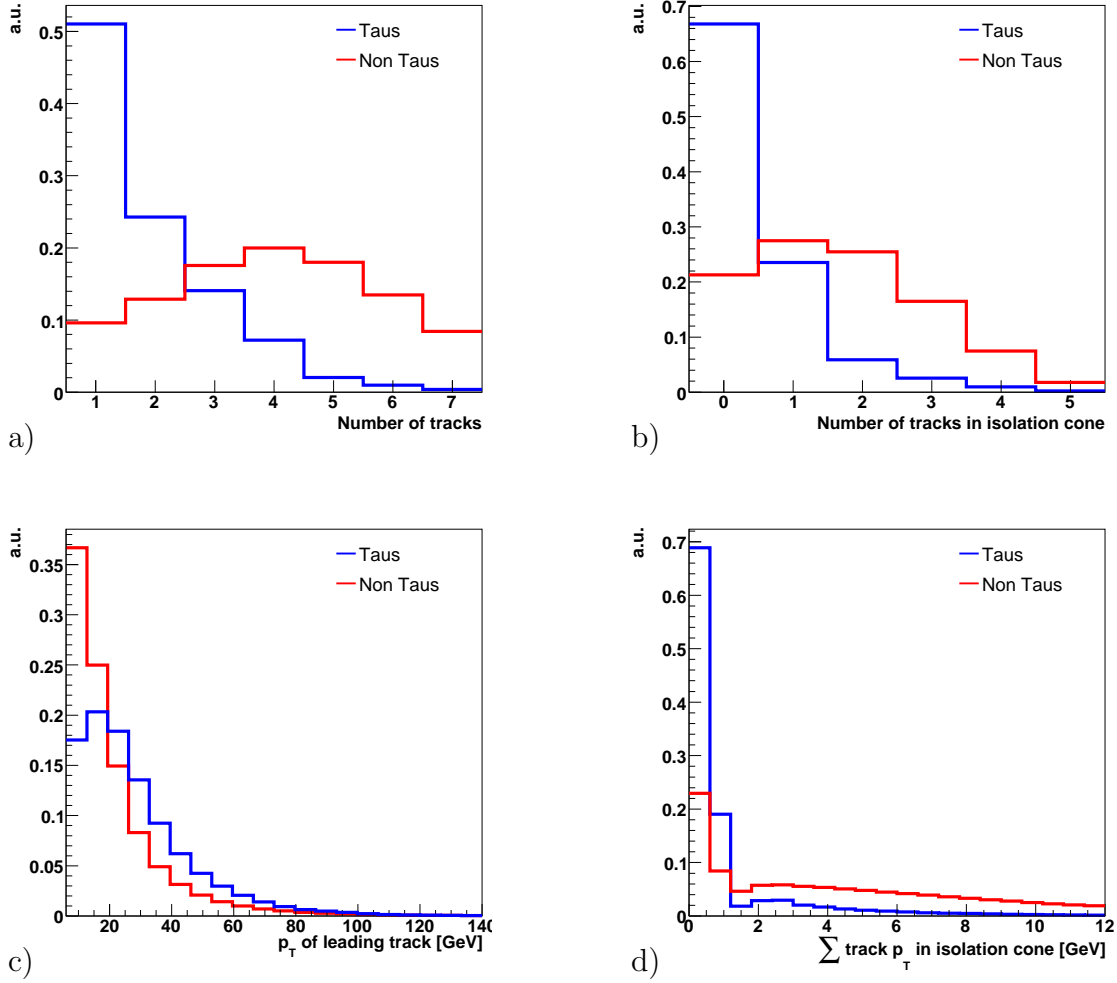


**Figure E.3:** The pdfs for tau-jet identification based on tracking information. a) is the total number of tracks within the isolation cone, b) is the same number without the number of tracks inside the signal cone. c) is the  $p_T$  of the leading track. d) is the summed  $p_T$  of all tracks inside the isolation cone, that are outside the signal cone.

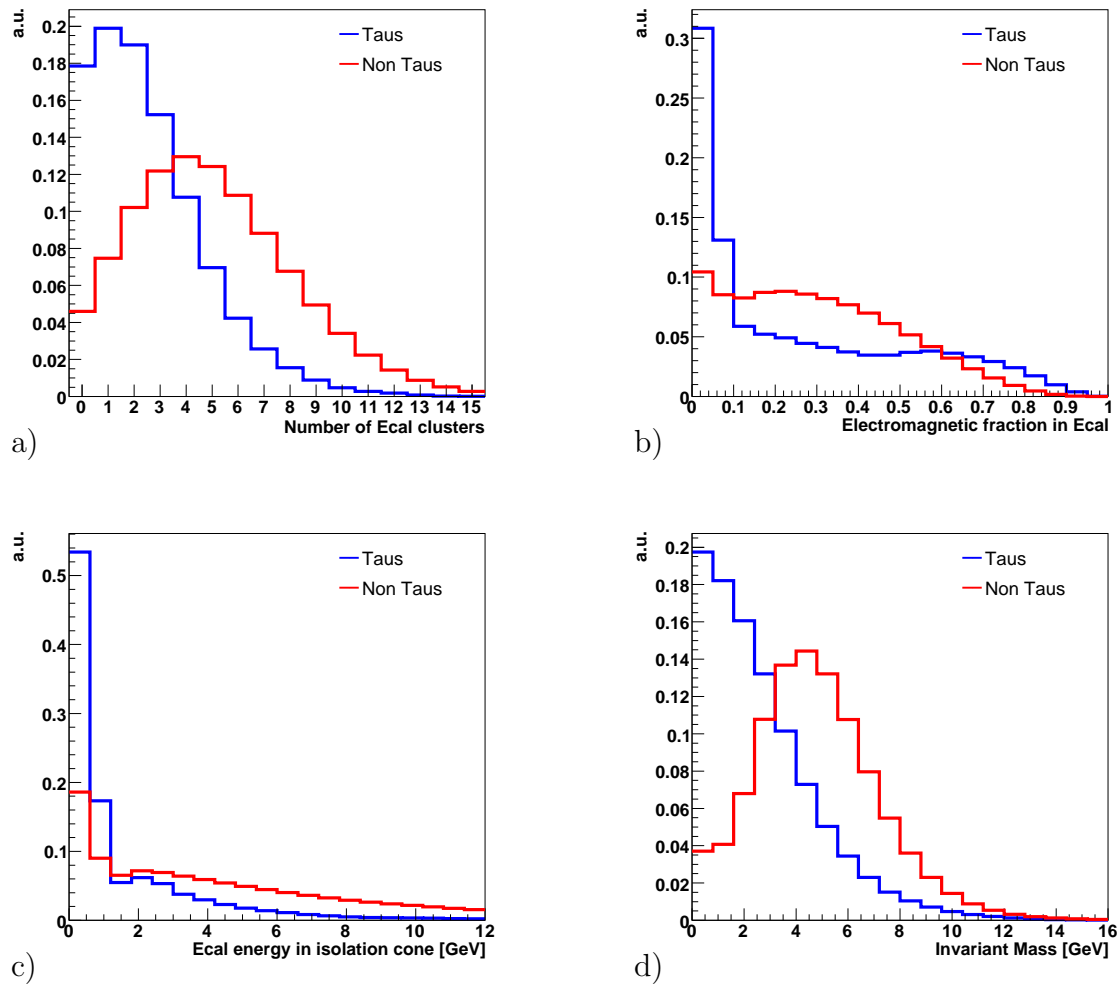


**Figure E.4:** a) The number of Ecal clusters inside the isolation cone. b) The electromagnetic fraction of those Ecal clusters. c) The total Ecal energy of clusters only inside the isolation cone and outside the signal cone. d) The pdf for the invariant mass.



# Bibliography

- [1] D. Griffiths. *Introduction to Elementary Particles*. Wiley & Sons, 1987.
- F. Halzen and A. D. Martin. *Quarks and Leptons: Introductory Course in Modern Particle Physics*. Wiley & Sons, 1984.
- D. H. Perkins. *Introduction to High Energy Physics*. Cambridge University Press, 2000.
- M. E. Peskin and D. V. Schroeder. *Quantum Field Theory*. B&T, 1995.
- [2] V. M. Abazov et al. Experimental discrimination between charge  $2e/3$  top quark and charge  $4e/3$  exotic quark production scenarios. *Phys. Rev. Lett.*, 98:041801, 2007.
- [3] C. Amsler *et al.* (Particle Data Group). Review of Particle Physics. *Phys. L.*, B667:1, 2008. <http://pdg.lbl.gov>  
Last visit: 11/2008. Last update: 10/2008.
- [4] G. t'Hooft. Renormalization of Massless Yang-Mills Fields. *Nucl. Phys.*, B33:173–199, 1971.
- G. t'Hooft. Renormalizable Lagrangians for Massive Yang-Mills Fields. *Nucl. Phys.*, B35:167–188, 1971.
- [5] S.L. Glashow. Partial-Symmetries of Weak Interactions. *Nucl. Phys.*, 22:579–588, 1961.
- A. Salam. *Elementary Particle Theory*. Almquist & Wiksell, 1968.
- S. Weinberg. A Model of Leptons. *Phys. Rev. Lett.*, 19:1264–1266, 1967.
- [6] SNO Collaboration. Direct Evidence for Neutrino Flavor Transformation from Neutral-Current Interactions in the Sudbury Neutrino Observatory. *Phys. Rev. Lett.*, 89:011301, 2002.
- Super-Kamiokande Collaboration. Determination of Solar Neutrino Oscillation Parameters using 1496 Days of Super-Kamiokande-I Data. *Phys. Lett.*, B539:179–187, 2002.

- [7] The LEP Working Group for Higgs Boson Searches. Search for the Standard Model Higgs boson at LEP. *Phys. Lett.*, B565:61–75, 2003.
- [8] P. Achard *et al.* Measurement of W polarisation at LEP. *Phys. Lett.*, B557:147, 2003.
- [9] M. Veltman. Limit on Mass Differences in the Weinberg Model. *Nucl. Phys.*, B123:89, 1977.
- W.J. Marciano. The Weak Mixing Angle and Grand Unified Gauge Theories. *Phys. Rev.*, D20:274, 1979.
- M. Veltman. Radiative Corrections to Vector Boson Masses. *Phys. Lett.*, B91:95, 1980.
- A. Sirlin. Radiative Corrections in the  $SU(2)_L \times U(1)$  Theory: A Simple Renormalization Framework. *Phys. Rev.*, D22:971–981, 1980.
- [10] LEP Electroweak Working Group. <http://lepewwg.web.cern.ch/LEPEWWG/>  
Last visit: 11/2008. Last update: 07/2008.
- [11] A.D. Martin *et al.* Physical gluons and high-E(T) jets. *Phys. Lett.*, B604:61–64, 2004.
- [12] J. Mnich. Experimental Tests of the Standard Model in  $e^+e^- \rightarrow f\bar{f}$  at the Z Resonance. *Phys. Rept.*, 271:181–266, 1996.
- [13] F. Abe *et al.* Observation of Top Quark Production in  $p\bar{p}$  Collisions with the Collider Detector at Fermilab. *Phys. Rev. Lett.*, 74:2626–2631, 1995.
- S. Abachi *et al.* Observation of the Top Quark. *Phys. Rev. Lett.*, 74:2632–2637, 1995.
- [14] Tevatron Electroweak Working Group. Combination of CDF and D0 Results on the Mass of the Top Quark. 2007. hep-ex/0703034.
- [15] T. Aaltonen *et al.* Measurement of the  $p\bar{p} \rightarrow t\bar{t}$  Production Cross Section and the Top Quark Mass at  $\sqrt{s} = 1.96$  TeV in the All-Hadronic Decay Mode. *Phys. Rev.*, D76:072009, 2007.
- V.M. Abazov *et al.* Measurement of the  $t\bar{t}$  Production Cross Section in  $p\bar{p}$  Collisions at  $\sqrt{s} = 1.96$  TeV. 100:192003, 2008. *Phys. Rev. Lett.*
- [16] V.M. Abazov *et al.* Evidence for the Production of Single Top Quarks. *Phys. Rev.*, D78:012005, 2008.
- [17] S. Catani *et al.* QCD. 2000. hep-ph/0005025.

- 
- [18] M. Duda. Top quark mass measurement in the All Jets channel with the CMS detector. (Preliminary title). PhD Thesis in preparation.
- [19] R.K. Ellis, W.J. Stirling, and B.R. Webber. *QCD and Collider Physics*. Cambridge University Press, 1996.
- [20] M. Cacciari *et al.* Updated predictions for the total production cross sections of top and of heavier quark pairs at the Tevatron and at the LHC. 2008. hep-ph/08042800v1.
- [21] M. Beneke *et al.* Top quark physics. 2000. hep-ph/0003033.
- [22] CERN. Layout of the LEP tunnel including future LHC infrastructures, 1997. modified picture.
- [23] CMS. *Detector Performance and Software*. CERN/LHCC 2006-001, 2006. Physics Technical Design Report, volume 1.
- [24] CMS. *The Magnet Project*. CERN/LHCC 97-010, 1997. Technical Design Report.
- [25] R.L. Glückstern. Uncertainties in Track Momentum and Direction, Due to Multiple Scattering and Measurement Errors. *Nucl. Instr. and Meth.*, 24:381, 1963.
- [26] CMS. *The Tracker System Report*. CERN/LHCC 98-006, 1998. Technical Design Report.
- [27] T. Franke. *Development and Evaluation of a Test System for the Quality Assurance during the Mass Production of Silicon Microstrip Detector Modules for the CMS Experiment*. PhD thesis, RWTH Aachen, 2005.
- [28] CMS. *Addendum to CMS Tracker TDR*. CERN/LHCC 2000-016, 2000. Technical Design Report Addendum.
- [29] CMS. *The Muon Project*. CERN/LHCC 97-032, 1997. Technical Design Report.
- [30] CMS. *The Electromagnetic Calorimeter*. CERN/LHCC 97-033, 1997. Technical Design Report.
- [31] CMS. *The Hadron Calorimeter Project*. CERN/LHCC 97-031, 1997. Technical Design Report.
- [32] TOTEM Collaboration. *TOTEM*. CERN/LHCC 2004-002, 2004. Technical Design Report.
- [33] CMS. The Tridas Project. *The Trigger Systems. Volume 1*. CERN/LHCC 2000-038, 2000. Technical Design Report.

- [34] CMS. The Trigger and Volume II Data Acquisition Project. *Data Acquisition & High-Level Trigger*. CERN/LHCC 2002-026, 2002. Technical Design Report.
- [35] Note in preparation. <https://twiki.cern.ch/twiki/bin/view/CMS/SWGuide>  
Last visit: 11/2008. Last update: 11/2008.
- [36] S. Agostinelli *et al.* GEANT4 – a simulation toolkit. *Nucl. Instr. and Meth. A*, 2003. 506 (3), 250-303.
- [37] M.L. Mangano *et al.* ALPGEN, a generator for hard multiparton processes in hadronic collisions. 2006. hep-ph/0206293  
<http://mlm.home.cern.ch/mlm/alpgen/alpdoc.pdf>  
Last visit: 11.2008. Last update: December 2006.
- [38] T. Sjostrand. PYTHIA 6.4. 2006. hep-ph/0603175.
- [39] M. Pierini and M. Spiropulu. Study of  $t\bar{t}$ +jets as a function of jet  $p_T$  and multiplicity for 2007 1  $fb^{-1}$  Monte Carlo production at CMS. 2007. CMS IN 2007/038.
- [40] M. Pierini and M. Spiropulu. Study of V+jets in bins of boson  $p_T$  and jet multiplicity for 2007 1  $fb^{-1}$  Monte Carlo production at CMS. 2007. CMS IN 2007/031.
- [41] E. Meschi *et al.* Electron Reconstruction in the CMS Electromagnetic Calorimeter. 2001. CMS NOTE 2001/034.
- [42] R. E. Kalman. A New Approach to Linear Filtering and Prediction Problems. *Transactions of the ASME—Journal of Basic Engineering*, 82(Series D):35–45, 1960.
- [43] S. Baffioni *et al.* Electron Reconstruction in CMS. 2006. CMS NOTE 2006/040.
- [44] Communication within the e/gamma group (electron ID).
- [45] G.C. Balzey *et al.* Run II Jet Physics. 2000. hep-ex/0005012.
- [46] S. Catani *et al.* Longitudinally invariant K(t) clustering algorithms for hadron hadron collisions. *Nucl. Phys. B*, 1993. 406, 187.  
J.M. Butterworth *et al.* Kt++: A C++ implementation of the  $K_{\perp}$  clustering algorithm. 2002. hep-ph/0210022.  
M. Cacciari and G.P. Salam. Dispelling the  $N^3$  myth for the  $k_t$  jet-finder. 2005. hep-ph/0512210.
- [47] A. Bhatti *et al.* Plans for Jet Energy Corrections at CMS. 2008. CMS AN 2007/055.

- [48] Note in preparation. <https://twiki.cern.ch/twiki/bin/view/CMS/WorkBookJetAnalysis>  
Last visit: 11/2008. Last update: 09/2008.
- [49] (Internal) Note in preparation. <https://twiki.cern.ch/twiki/bin/view/CMS/SWGuideBTagging>  
<https://twiki.cern.ch/twiki/bin/view/CMS/SWGuideBTagMCTools>  
Last visit: 11/2008. Last update: 06/2008.
- [50] A. Rizzi *et al.* Track impact parameter based b-tagging with CMS. 2006. CMS NOTE 2006/019.
- [51] P. Avery *et al.* Measurement of Missing Transverse Energy With the CMS Detector at the LHC. 2006. CMS NOTE 2006/035.
- [52] <https://twiki.cern.ch/twiki/bin/view/CMS/CSA07>  
Last visit: 11/2008. Last update: 08/2008.
- [53] V. Blobel and E. Lohrmann. *Statistische und numerische Methoden der Datenanalyse*. Teubner, 1998.
- [54] C. Bishop. *Neural Networks for Pattern Recognition*. Oxford University Press, 1995.
- [55] S. Kasselmann. *Top Quark Mass Measurement in the Lepton+Jets Channel using Full Simulation of the CMS Detector*. PhD thesis, RWTH Aachen, 2007.
- [56] G. Mahlon and S. Parke. Angular correlations in Top Quark Pair Production and Decay at Hadron Colliders. 1995. hep-ph/9512264.
- [57] J. Brau (ed.) *et al.* International Linear Collider reference design report. 1: Executive summary. 2: Physics at the ILC. 3: Accelerator. 4: Detectors. ILC-REPORT-2007-001.
- [58] A. Zell *et al.* *SNNS – Stuttgart Neural Network Simulator, User Manual, Version 4.2*. University of Stuttgart, University of Tübingen, 1998. <http://www.ra.cs.uni-tuebingen.de/SNNS/>  
Last visit: 11/2008. Last update: 07/2008.
- [59] S. Gennai *et al.* Tau jet reconstruction and tagging at High Level Trigger and offline. 2006. CMS NOTE 2006/028.